BANDWIDTH EXTENDED DESIGNS OF DOUBLE-RIDGED GUIDE HORN ANTENNAS

by

Benjamin Jacobs

Submitted in partial fulfilment of the requirements for the degree
Philosophiae Doctor (Electronic Engineering)

in the

Department of Electrical, Electronic and Computer Engineering
Faculty of Engineering, Built Environment and Information Technology

UNIVERSITY OF PRETORIA

August 2024

SUMMARY

BANDWIDTH EXTENDED DESIGNS OF DOUBLE-RIDGED GUIDE HORN ANTENNAS

by

Benjamin Jacobs

Supervisor:	Professor J. W. Odendaal
Co-supervisor:	Professor J. Joubert
Department:	Electrical, Electronic and Computer Engineering
University:	University of Pretoria
Degree:	Philosophiae Doctor (Electronic Engineering)
Keywords:	Additive manufacturing, antenna measurement, broad bandwidth, double-ridged guide horn antenna, electromagnetic simulation

The explosive growth in bandwidth requirements on antennas and antenna systems, driven by various industries, also drives the need for the ever-increasing bandwidth of antennas used for testing. The broadband Double-Ridged Guide Horn (DRGH) antenna finds widespread use in antenna measurement and ElectroMagnetic Compatibility/Interference (EMC/I) testing. An example of a DRGH used extensively for testing is the 1-18 GHz DRGH antenna. A study using ElectroMagnetic (EM) simulation was performed to determine the factors that limit the bandwidth of these antennas. All the parts and sub-assemblies of the DRGH were investigated to determine the impact of each part and or sub-assembly on the electrical performance of the antenna. This was done in simulation using reduced complexity models and parametric studies. The design changes that resulted from this study were implemented in several prototype antennas used for verification. It was found that it is possible to design DRGH antennas with bandwidth ratios of 100:1 and possibly beyond. It is expected that at higher frequencies, the limit will be the manufacturing tolerances and technology, and at lower frequencies, the maximum permissible size of the antenna.

LIST OF ABBREVIATIONS

2D	Two Dimensional
3D	Three Dimensional
ABS	Acrylonitrile Butadiene Styrene
AM	Additive Manufacturing
CAD	Computer-Aided Design
CEM	Computational ElectroMagnetic
CESM	Communications Electronic Support Measures
CNC	Computer Numerically Controlled
CPU	Central Processing Unit
CW	Continuous Wave
DLP	Digital Light Processing
DMLS	Direct Metal Laser Sintering
DRGH	Double-Ridged Guide Horn
EM	ElectroMagnetic
EMC/I	ElectroMagnetic Compatibility/Interference
FDM	Fused Deposition Modelling
FDTD	Finite Difference Time Domain
FEM	Finite Element Method
mmW	millimetre Wave
MoM	Method of Moments
MUB	Maximum Usable Bandwidth
PC	Personal Computer
PCB	Printed Circuit Board
PEC	Perfectly Electrical Conducting

PLA	PolyLactic Acid
PTFE	PolyTetraFluoroEthylene
RADAR	Radio Detection and Ranging
RESM	Radar Electronic Support Measures
RF	Radio Frequency
SEP	Surface Equivalence Principle
SLA	StereoLithogrAphy
SLM	Selective Laser Melting
SLS	Selective Laser Sintering
SS	Stainless Steel
TEM	Transverse ElectroMagnetic
UTD	Uniform Theory of Diffraction
VEP	Volume Equivalence Principle
VNA	Vector Network Analyser
VSWR	Voltage Standing Wave Ratio
W	Watt

TABLE OF CONTENTS

CHAPTER 1 INTRODUCTION

1.1 PROBLEM STATEMENT

1.1.1 Context of the Problem

Globally, diverse industries have an ever-increasing demand for broader bandwidth systems. Two of the most demanding industries for broadband systems are the telecommunications sector and the defence industry. For instance, in the telecommunications industry, for broadband 5G cellular networks the latest 3GPP TS 38.101–1 standard [1] defines operation in frequency ranges from 410 to 7125 MHz (FR1), 24.25 to 52.6 GHz (FR2-1) and 52.6 to 71 GHz (FR2-2). Within the defence industry, state-of-the-art Radar Electronic Support Measures (RESM) systems necessitate frequency ranges from a few hundred MHz to 40 GHz and beyond, and Communication Electronic Support Measures (CESM) systems range from a few kHz up to 9 GHz or more.

Typically, ultra-wideband systems require multiple antennas to cover the complete frequency range. Despite substantial advancements in the speed of measurement instrumentation such as Spectrum Analyzers and Vector Network Analyzers (VNA) over the past decade, the testing of these broadband systems can be extremely time-consuming with one of the significant factors that have a major influence on measurement time being the setup and calibration of different source and reference antennas to cover the whole frequency range. Increasing the operational bandwidth of the antennas used for testing not only reduces measurement time, but also cuts costs associated with expensive test antennas if a single source or reference antenna replaces two or more antennas.

One of the most prevalent measurement antennas used are broadband Double-Ridged Guide Horn (DRGH) antennas, for antenna measurement as reference, source, and ElectroMagnetic Compatibility/Interference (EMC/I) testing. Widespread adoption of DRGH antennas for these applications was driven by noteworthy characteristics such as high gain, favourable pattern behaviour, high power handling, straightforward excitation, and relatively uncomplicated construction, but most importantly for this study, broad bandwidth.

For more than three decades the de-facto industry standard test antenna for the 1-18 GHz band (18:1 bandwidth) had been the DRGH, with the traditional design being derived from the antenna designs proposed in [2] fifty years ago. Deficiencies in the radiation pattern above 12 GHz were identified through ElectroMagnetic (EM) simulations [3] - [5], sparking renewed interest in the design of these antennas. Initial efforts were concentrated on addressing the pattern deterioration problem, resulting in several enhanced designs [6] - [14]. Subsequent endeavours included studies on manufacturing tolerance and sensitivity [15] - [18], extending enhancements to other frequency bands [19] - [21], and improving the electrical performance by exploring design changes to for example the ridges, coax-to-waveguide launcher, and sidewalls [22] - [25]. Some of these studies also yielded designs with slightly broader bandwidths ranging from 20:1 to 25:1 [11], [13], [20], [23]. In [26] a DRGH design boasting an 83:1 bandwidth (0.6–50 GHz) is proposed, however, no prototype had been manufactured and only simulated results are available. The design information presented had been incomplete and some results lacked sufficient detail, for example, the antenna gain had been presented in wide frequency steps, potentially overlooking narrow dips in gain indicative of pattern break-up. This poses a challenge in verifying the accuracy of the claims made in [26].

In this study, all the parts and sub-assemblies of the DRGH were investigated to determine the impact of each part and or sub-assembly on the bandwidth of the DRGH. The most important parts and or sub-assemblies of the DRGH with regards to limiting the bandwidth were found to be the ridges and coax-to-waveguide launcher. It is shown how the redesign of the ridges and coax-to-waveguide launcher makes it possible to design DRGH antennas with significantly extended bandwidth without sacrificing electrical performance. A method to design a basic DRGH is proposed. This basic design can then be used as a starting point for further optimisation.

1.1.2 Research Gap

Further improving the bandwidth of DRGH antennas significantly beyond 18:1 would be of value to the antenna measurement and EMC/I community since it would enable reduced measurement time and thus reduced cost of antennas and antenna systems. This is driven by the need for wider bandwidth systems in various industries worldwide. The research gap identified is therefore the availability of design procedures or guidelines to design and manufacture DRGH antennas with bandwidths of significantly more than 18:1.

1.2 RESEARCH OBJECTIVE AND QUESTIONS

A literature study revealed that there is no well-established definitive limit to the bandwidth of DRGH antennas. The research objective of this study is to determine if it is feasible to design and manufacture DRGH antennas with bandwidths extending beyond the typical industry standard of 18:1. Inclusive of this objective is to investigate, identify and describe the methods used to make this possible. In addition to the research objective stated above, the following requirements should also be adhered to as far as possible:

- The electrical performance of the extended bandwidth design should remain similar or reasonably similar to current state-of-the-art designs as summarised below:
    - Typical Voltage Standing Wave Ratio (VSWR) of 2:1 or better, maximum of 2.5:1.
    - Boresight realised gain of 3 dBi or better at the low end, and 14 dBi or better at the high end.
    - No pattern breakup anywhere in the operational band.

- The design should be usable for antenna measurement as a source or reference antenna and/or for EMC/I measurements. For some EMC/I tests, high power handling is required, the antenna should therefore have the capability to handle high power. For antenna measurement applications, however, high power handling is not a prerequisite.

To achieve the research objective the following research questions needed to be answered:

- What parts and or sub-assemblies of the DRGH limit the bandwidth?
- Can these parts and or sub-assemblies be redesigned to extend the bandwidth of the antenna with acceptable electrical performance?
- Can a design procedure or approach be formulated that will result in practical, manufacturable DRGH designs with bandwidths significantly beyond 18:1?

1.3 APPROACH

The approach followed was to perform an investigation to answer the first research question using EM simulation. The EM simulation tools used were FEKO from Altair HyperWorks [27] and CST from Dassault Systèmes [28]. The design presented in [14] was used as the basis for this study, but the FEKO EM model was first improved upon from the one used in [14]. Each part and or sub-assembly of the DRGH was then evaluated in terms of its influence on the DRGH's electrical performance. This was done in simulation using different approaches, for example, parametric studies and reduced complexity models.

Once the parts and or sub-assemblies that limit the bandwidth of the design were identified, changes to the design that would potentially lead to increased bandwidth were then proposed, implemented in the simulation model and investigated. All the design changes were then combined in an extended bandwidth design. Upon confirmation of this design's simulated performance, the electrical design was converted into a practical realisable mechanical design of the DRGH. Prototypes were constructed and measured, with the measured results being used for verification and validation by comparison to the simulated results and desired electrical performance requirements. The successful practical realisation of extended bandwidth DRGH designs that met the desired requirements confirmed research question two, i.e. that DRGH parts and or sub-assemblies can be redesigned to extend the bandwidth of the antenna with acceptable electrical performance.

A method was formulated to design a basic DRGH, as starting point for further optimisation. The use of this method was then illustrated by providing simulated examples of two extended bandwidth DRGH designs, which confirmed research question 3.

1.4 RESEARCH CONTRIBUTION

This thesis presents a design procedure or guideline to design DRGH antennas with bandwidths significantly beyond 18:1. This approach was used to design the widest bandwidth 100:1 (0.5-50 GHz) DRGH antenna published to date in literature, validated with measured results of a prototype. This thesis thus demonstrates the feasibility of designing and manufacturing DRGH antennas with bandwidth ratios of 100:1 and potentially even beyond this threshold.

Detailed information is provided that will allow antenna engineers to design and manufacture extended bandwidth DRGH antennas. These antennas can be manufactured using widely available and cost-effective Additive Manufacturing (AM), also called 3D printing, and Computer Numerically Controlled (CNC) machining techniques.

Several new and novel design concepts were introduced:

- New coax-to-waveguide launcher designs:
    - A version capable of handling high power consisting of a three-step pyramidal cavity with partially open *E*-plane sidewalls operating over 0.5-18 GHz (36:1).

    - A honeycomb absorber-filled cavity similar to cavity-backed spiral antennas with a novel coax-to-waveguide launcher sub-assembly based on a typical Vivaldi antenna suitable for 100:1 (0.5-50 GHz) bandwidth designs.
- The addition of sub-ridges and several tapered ridge sections for improved electrical performance and extended bandwidth.
- Utilisation of the coaxial feeding sub-assembly as an impedance transformer between the 50 Ω input connector and the characteristic impedance of the double-ridged waveguide at the feed point if different.

1.5 RESEARCH OUTPUTS

The current study builds upon and significantly expands on previous work performed as part of the author's Master of Engineering studies from which the following journal articles were published: [14], [16].

The following journal articles were published based on the research presented in this thesis:

- B. Jacobs, J. W. Odendaal, and J. Joubert, "Compact 0.5–18 GHz double-ridged guide horn antenna," *IET Microw. Antennas Propag.,* vol. 15, no. 4, pp. 427-440, Mar. 2021.
- B. Jacobs, J. W. Odendaal, and J. Joubert, "Wideband 0.5–50 GHz double-ridged guide horn antenna using coaxial-to-ridge waveguide launcher," *IET Microw. Antennas Propag.*, vol. 18, no. 4, pp. 248-265, Dec. 2023.

1.6 OVERVIEW OF STUDY

The literature review in Chapter 2 provides background on the historical evolution of DRGH antenna development and the methods employed in their design. The basic parts and sub-assemblies that constitute the DRGH are identified and discussed as well as the materials and manufacturing methods used to produce DRGH antennas. The latest cutting-edge designs, excluding the contributions of this thesis and the relevant publications detailed in Section 1.5, are summarised in terms of design changes and performance.

Chapter 3 shows how the original 1-18 GHz DRGH design was used as the basis for the investigation into bandwidth-limiting parts and or sub-assemblies of the antenna using EM simulation. Design changes are proposed that resulted in a 36:1 (0.5-18 GHz) design.

In Chapter 4, the bandwidth is further extended by using the 0.5-18 GHz DRGH design as the basis for further investigation into bandwidth-limiting parts and or sub-assemblies of the antenna and removing some design restrictions such as the ability to handle high power. Design changes are proposed that resulted in a 100:1 (0.5-50 GHz) design. Both the designs above were verified by measurements on manufactured prototype antennas.

Combining all the results from the parametric studies in Chapters 3 and 4, Chapter 5 presents a method that can be followed to design broadband DRGH antennas with bandwidths significantly greater than 18:1.

Chapter 6 provides concluding remarks, summarising the key findings, insights and contribution of this study.

CHAPTER 2 LITERATURE STUDY

2.1 INTRODUCTION

This chapter presents detailed background information on DRGH antenna development. A short introduction to the background of the DRGH antenna is given in Section 2.2. The DRGH typically consists of several sub-assemblies; the coaxial feed, the coax-to-waveguide launcher and cavity, the *E*- and *H*-plane sidewalls and the ridges. These sub-assemblies are described in detail in Section 2.3 with the manufacturing methods and materials used for the sub-assemblies discussed in Section 2.4. The development of DRGH antennas is then discussed concerning the tools used to design and analyse these antennas in Section 2.5. The typical performance of the current state-of-the-art DRGH designs is presented in Section 2.6 along with design changes that provided incremental bandwidth or performance improvement. Finally, in Section 2.7, the chapter is summarised.

2.2 BACKGROUND OF THE DRGH ANTENNA

Typical types of horn antennas include standard rectangular (which could be sectoral or pyramidal horns), profiled, conical, corrugated, quad and double-ridged horn antennas. The focus of this dissertation is on DRGH antennas. Presently horn antennas are widely used in antenna and EMC/I measurement, but the origin of horn antennas dates back to well over a century. The origin of horn antennas is closely linked to that of waveguide with the horn being the radiating transition between waveguide and free space. Waveguide and its properties were first demonstrated at the end of the 1800s by electromagnetic pioneers such as O. J. Lodge, Lord Rayleigh and J. C. Bose [29] - [31]. In 1897 Bose showed what can be considered as the first pyramidal horn antenna used as a receiving antenna in his receiver arrangement [31]. The interest in waveguides and horns faded until the late 1930s with the concepts being "rediscovered" by engineers such as G. C. Southworth [32], and W. L. Barrow [33], [34] because of the development of Radio Detection and Ranging (RADAR) and the start of World War II. At this stage, the bandwidth of horn antennas was limited to that of the waveguide used to feed the horn, with practical bandwidth being less than 2:1 for standard rectangular waveguides.

The development of ridged waveguides in the 1950s [35], [36], and its extension to double-ridged horn antennas, see Figure 2.1, allowed rapid expansion of the bandwidth of horn antennas beyond an octave. The cut-off frequency of the fundamental mode is reduced, increasing the Maximum Usable Bandwidth (MUB), by adding ridges into the design of the basic rectangular horn. This initially resulted in a bandwidth increase to 3:1 [37] similar to the standard double ridged waveguide. Further improvements made on various parts and sub-assemblies of the antenna, for example, the ridge profile, coax-to-waveguide launcher and sidewalls led to the bandwidth further increasing to 12:1 [2], [38] - [40].

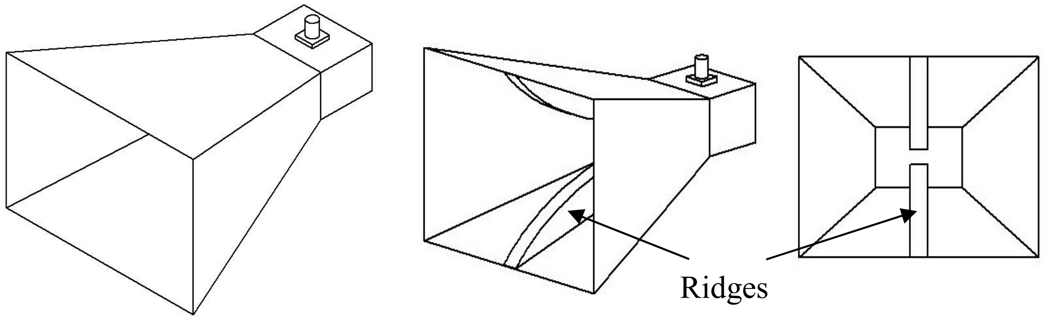

(a) (b)

Figure 2.1. (a) Standard rectangular pyramidal horn and (b) DRGH from [17].

Derivatives of the design in [2], see Figure 2.2, were in widespread use, for example as the 1-18 GHz DRGH specified in MIL-STD-461 [41], however, in the early 2000s deficiencies in the radiation pattern above 12 GHz were exposed using EM simulations [3] - [5]. This result spurred a lot of research into DRGH antenna design and subsequently several authors presented new designs that solved the pattern deterioration problem [6] - [14]. The increased focus on DRGH design also led to tolerance and sensitivity studies [15], [18], studies with regards to manufacturing defects [16], [17], and the extension of design improvements to other bands such as 0.2-2 GHz, 18-40 GHz, 0.1-1 GHz and 10-100 GHz [19] - [21]. Further performance improvements were achieved by again investigating and making changes to the ridge width, ridge profile, coax-to-waveguide launcher, and sidewalls [22] - [25].

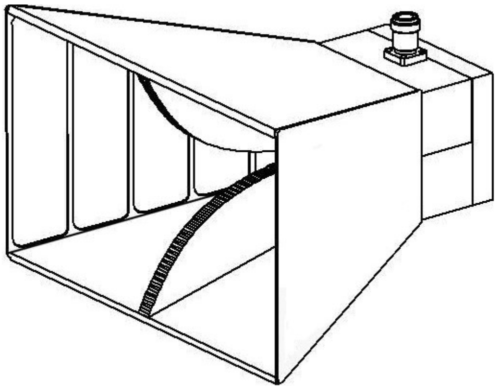

Figure 2.2. Traditional 1-18 GHz DRGH based on Kerr design from [17].

Some of the improvements also resulted in slightly wider bandwidths in the order of 20:1 to 25.7:1 [11], [13], [20], [23]. In [26] an 83:1 bandwidth (0.6–50 GHz) DRGH is proposed, however, only simulated results were presented and a lack of information makes it difficult to thoroughly validate this design. The antenna gain was also presented in very large frequency steps and it is possible that narrow gain dips could have been missed which usually is an indication of pattern break-up.

2.3 PARTS AND SUB-ASSEMBLIES OF THE 1-18 GHZ DRGH ANTENNA

The DRGH typically consists of the following main sub-assemblies: The coaxial feed, the coax-to-waveguide launcher and cavity, the *E*- and *H*-plane sidewalls and the ridges. The ridges start inside the coax-to-waveguide launcher assembly and extend into the flared waveguide assembly formed by the sidewalls. The coaxial feed is the transmission line connecting the Radio Frequency (RF) connector with the ridges and is contained inside the ridges and launcher assembly. To illustrate the typical sub-assemblies and how they fit together the design as presented in [14] will be used as reference, the three-dimensional (3D) Computer-Aided Design (CAD) model of this antenna is shown in Figure 2.3.

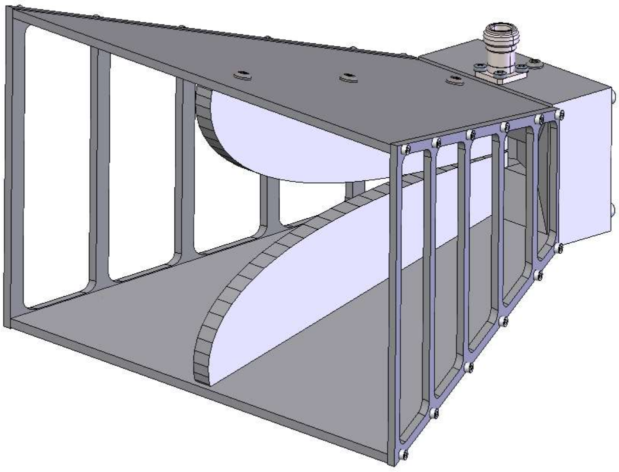

Figure 2.3. 3D CAD model of the 1-18 GHz DRGH design from [14].

2.3.1 Coaxial Feed

The coaxial feed is the transmission line that connects the RF connector to the ridges. For the 1-18 GHz DRGH the RF connector used is typically either a precision N-Type that works up to 18 GHz or a SMA (or similar) connector if high power handling is not needed. The centre conductor of the RF connector is connected with a pin to the bottom ridge. This pin passes through a cylindrical hole in the top ridge with this hole forming the outer conductor. The hole can be filled with a dielectric, but typically for the 1-18 GHz DRGH the coaxial feed is kept as an airline for better power handling. Usually, the coaxial line characteristic impedance is designed to be the same as the RF connector, i.e. 50 Ω. There are various methods to ensure proper termination of the feed pin on the bottom ridge, for example:

Soldering, using conductive epoxy or by mechanical means such as a collet, grub screw, press fit or thread. These methods will be discussed further in Section 2.4. The design shown in Figure 2.4 makes use of a collet press fitted into the bottom ridge. Once the pin is inserted into the collet conductive epoxy can be applied to the feed point to fill any possible gaps.

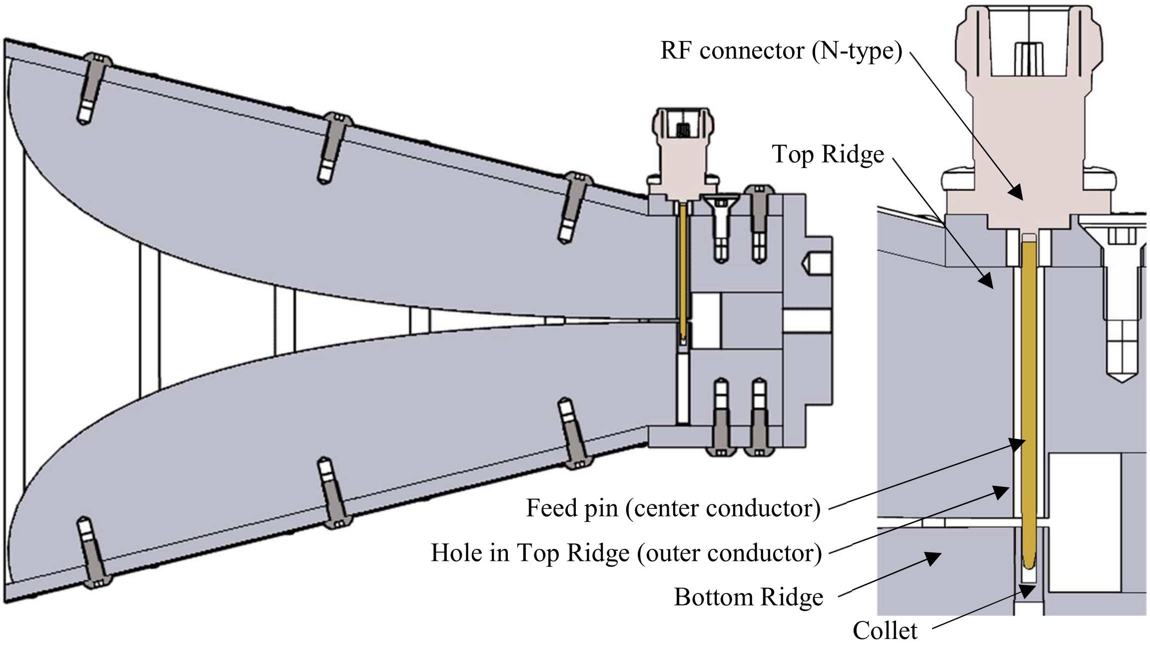

Figure 2.4. Cross-section of the DRGH showing the coaxial feed assembly.

Historically the outer conductor of the coaxial feed line was implemented using a hollow bush that passed through a hole in the top ridge connecting the top ridge and outer of the connector. The bottom ridge contained another bush (solid or hollow depending on the design of the feed pin termination) to which the feed pin could be fastened using various methods as discussed in Section 2.4. This assembly allows for identical ridges to be manufactured for both the top and bottom ridges of the DRGH antenna, but as was shown in [16], [17], it is important to ensure that there are no gaps between the sub-assemblies in the feed pin assembly that could lead to resonances in gain or VSWR.

2.3.2 Coax-to-Waveguide Launcher and Cavity

The coax-to-waveguide launcher is one of the most crucial sub-assemblies of the horn antenna design. Usually, it is easily identifiable as the "box" sub-assembly at the back of the DRGH flared waveguide, see Figure 2.5. The coaxial feed is effectively part of this assembly, but the coax-to-waveguide launcher can also be seen as the transition between the coaxial feed and the flared waveguide with ridges. The launcher must ensure that the unbalanced coaxial feed is transformed to a balanced double-ridged waveguide geometry, effectively performing the role of a balun. The launcher also suppresses higher-order modes that could cause pattern deterioration and reduce backward radiation.

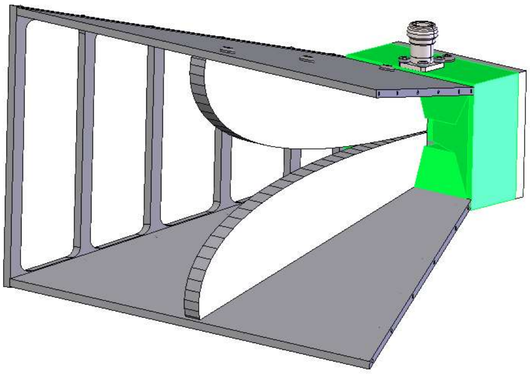

Figure 2.5. Coax-to-waveguide launcher (green highlight), *E*-plane sidewall removed for clarity.

Due to the complexity of this sub-assembly, the design was mostly done through experimentation, either on physical prototypes or in EM simulation. Various geometries were used in the past as illustrated in Figure 2.6. The first and most basic design consists of an empty box cavity as shown in Figure 2.6, top left. This design can typically operate over bandwidths of 3:1 to 9:1. Examples of this design in literature can be found in [38], [42] - [44].

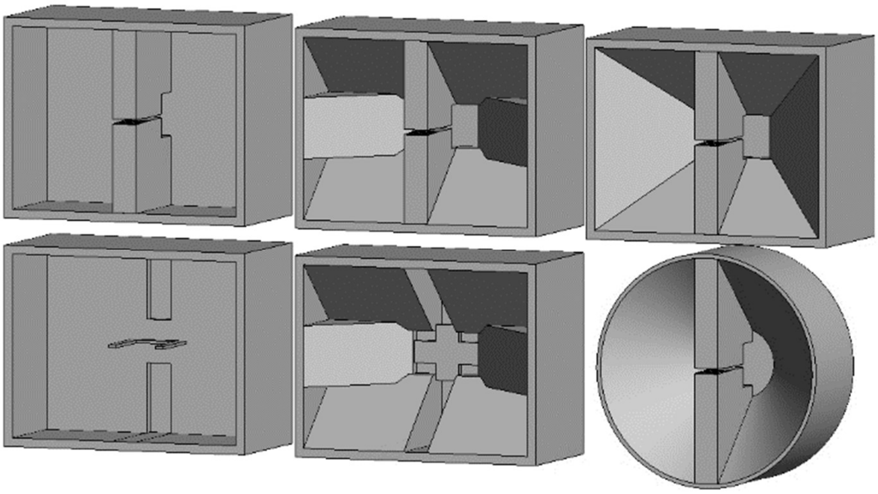

Figure 2.6. Previous coax-to-waveguide launcher designs from [45].

The design of the ridges in the launcher depends on the desired MUB. Walton and Sundberg [38] used the transverse resonance method to design the dimensions of the ridged cross-section in the coax-to-waveguide launcher. In [38] it was found that a critical dimension is the distance from the feed pin to the shorting back plane of the cavity which must be less than λ/2 at the highest operating frequency. Also according to [38] the height of the waveguide launcher assembly must be less than λ at the highest operating frequency to prevent propagation of the TE_{02} mode. If the feed pin is in the centre of the waveguide (thus in the centre of the ridges) and a short straight section of ridged waveguide is used between the feed pin and the flared waveguide assembly, the TE_{20} mode cannot be excited, and the first higher order mode is the TE_{30} mode [38].

In most empty box cavities, the ridge is stepped down and extended into the cavity up to the back short. For example, see Figure 9 in [38] where the ridge is cut away so that a section approximately ⅛ of the waveguide height is left. Basically, this results in a gap of ¾ of the waveguide height between the ridges as they extend into the launcher after the feed point.

The most widespread, traditional 1-18 GHz design uses a box cavity filled with *E*-plane flares and *H*-plane wedges (Figure 2.6, top centre). The ridge is also stepped down and extended into the cavity, along with the back short which forms a smaller rectangular box cavity. Examples of this design in literature can be seen in [4], [5], [8], [12], [15] - [19]. This design was adapted from the coax-to-waveguide launcher designs in [2], [40] used in DRGH antennas with a maximum bandwidth of 12:1. Due to the low quality of the figures in the old literature references the exact detail of these designs are somewhat unclear, but from the text the following should be noted:

- The first design in [40] used a short section (approximately 1.5 inches) of S-Band waveguide with inner dimensions of 2.84 inches × 1.34 inches. The height of the waveguide was kept constant at 1.34 inches, but the width was tapered down from 2.84 inches at the launcher aperture to 1.39 inches at the feed point. This width was then held constant from the feed point to the back short 0.325 inches away. So this design is basically a box with ridges and tapered inserts in one plane (*H*-plane) only.
- The second design in [40] used a smaller box of 3.4 × 2.616 inches. Tapered inserts were placed in both planes. These inserts tapered down from the aperture size, 1 inch away from the feed, to a size of 1.4 × 0.872 inches at the feed. This size is then maintained for 0.325 inches up to the back short. This design is thus very similar to that shown in Figure 2.6, top right, i.e. a pyramidal taper which has a small box cavity at the top.
- The 1-12 GHz design in [2] changed the size of the launcher from the second design in [40]. Specifically, the width at the feed point was reduced from 1.4 to 1.2 inches.

Metal pins were included in these designs to improve the high-frequency VSWR. These pins were connected between the back of the ridge and the back short, in the centre of the back edge of each ridge.

Further improvements in the launcher design in [2] resulted in a bandwidth approaching 18:1 albeit with some degradation in the VSWR to 3:1 at low frequencies and noted pattern deterioration at 18 GHz. The launcher cross-section was further reduced from 1.2 × 0.872 inches to 1 × 0.625 inches. The coaxial inserts' (bushes) dimensions were reduced from 0.276 to 0.187 inches and the input connector changed from N-type to SMA. These changes improved high-frequency VSWR at the expense of low-frequency VSWR. None of these designs could, however, suppress unwanted modes in designs with bandwidths over 12:1 typically resulting in pattern deterioration above 12 GHz.

A variation of the basic box design was the introduction of mode-suppressing fins, shown bottom left in Figure 2.6, with the ridges omitted for clarity. This launcher was used in DRGH designs without pattern deterioration over bandwidths of 18:1 albeit with reduced gain and VSWR performance at low frequencies. Examples can be seen in [6] - [8]. A variation of the traditional flare and wedge design was the inclusion of a cross-shaped structure in the small rectangular box cavity as presented in [23] (bottom centre in Figure 2.6, with the ridges omitted for clarity), this launcher was used in a DRGH horn design with a 25:1 bandwidth (0.8-20 GHz) without pattern deterioration.

It has also been shown that pyramidal and semi-pyramidal coax-to-waveguide launcher designs shown in Figure 2.6, top right, can work over an 18:1 bandwidth without pattern deterioration if correctly designed, see [14]. Examples of conical launchers, bottom right in Figure 2.6, can be seen in [46], [47].

2.3.3 *E*- and *H*-plane Sidewalls

The *E*- and *H*-plane sidewalls form the flared waveguide assembly of the horn antenna, see Figure 2.7. For DRGH antennas the flared waveguide assembly also contains the profiled ridges. The flared waveguide assembly provides the transition between the coax-to-waveguide launcher and free space. The design of this assembly mostly determines the radiating performance of the DRGH. For pyramidal horns the aperture method calculation is used to determine the dimensions of the flared assembly to achieve the desired gain and beamwidth characteristics [48], [49].

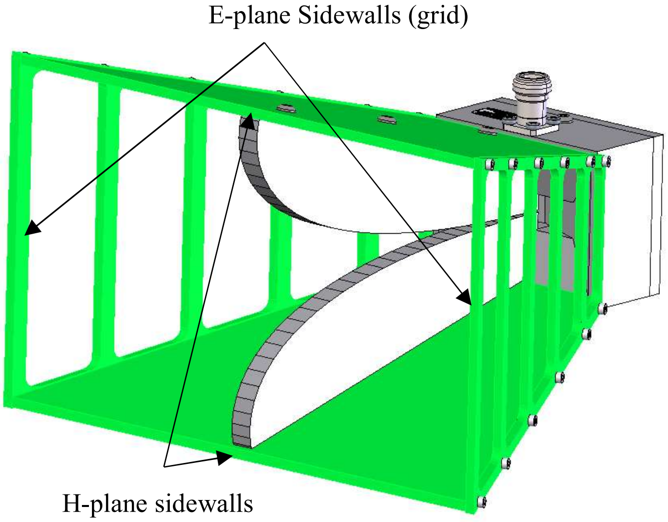

Figure 2.7. *E*- and *H*-plane Sidewalls of the DRGH (green highlight).

Figure 2.8 shows the definition of the aperture dimensions of a pyramidal horn antenna. The introduction of ridges in the flared waveguide assembly complicates the aperture distribution and therefore the aperture method cannot be used to design the flared waveguide assembly of DRGH antennas [39]. It is important to note that the aperture size of the traditional 1-18 GHz DRGH antenna is defined in MIL-STD-461 [41] as 24.2 ×13.6 cm (width by height). Ridges were introduced in both the coax-to-waveguide launcher and flared waveguide assembly to increase the MUB. To allow the ridges to be terminated in the waveguide assembly, the *H*-plane aperture of the horn at the point of ridge termination must be at least $\lambda/2$ at the lowest operating frequency [38]. This ensures that the horn operates above the cut-off for the TE_{10} mode. Therefore, for operation down to 1 GHz an aperture width of 15.0 cm is required as compared to the MIL-STD requirement of 13.6 cm ($\lambda/2.2$).

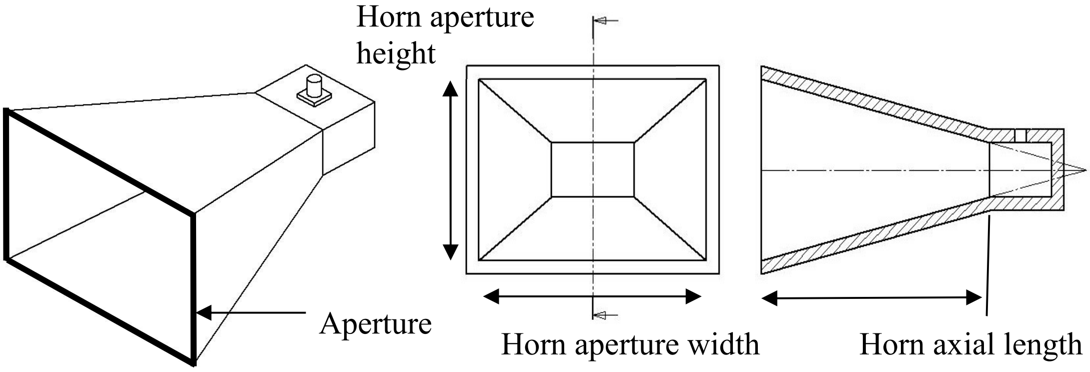

Figure 2.8. Flared waveguide assembly of the pyramidal horn antenna from [17].

The profile of the ridges is designed to provide a smooth impedance transition from the ridged waveguide at the coax launcher to that of free space (377 Ω), [2], [38]. In [38] it is suggested that the flared assembly should therefore be reasonably long, at least λ/2 at the lowest operating frequency to ensure a smooth impedance taper. According to [38] ridges of horns with reduced axial length might cause undesirable radiation characteristics and reduced gain especially when a constant ridge width is used. Thus, for operation down to 1 GHz, an axial length of 15 cm or more is required.

The ridges affect the phase variation of the *E*- and *H*-plane differently and this must also be considered when designing the flared waveguide assembly and ridges [38]. Increasing the horn axial length can reduce the phase error and thus improve radiating characteristics with the drawback being increased size, mass and cost. Another method that can be used to improve the phase error and increase gain is the use of a lens at the aperture of the DRGH, [20], [26], [38], [50].

Initially, the sidewalls of the flared assembly were solid. Later the *E*-plane sidewalls of DRGH antennas were implemented as a grid, while the *H*-plane flares were kept solid. This was done since it was shown in [2] that the *E*-plane sidewalls increase the low-frequency gain but have no significant effect above 3.5 GHz. It was found that the ridges control the radiation in the upper-frequency band of operation, see [2], [39], [40], [51]. Therefore, these sidewalls could be substituted with a grid. The spacing of the grid elements is typically a tenth of a wavelength at the low end of the band to simulate a solid conducting wall at these frequencies [38]. No information is given on how to define the thickness of the grid elements themselves, it is assumed that this was done experimentally. Thin grids etched on a dielectric substrate were used to reduce mass, improve robustness (thin unsupported grids are fragile) and make the design easier to weatherproof [2].

For several designs the *E*-plane sidewalls were completely removed since it was found that the dielectric substrate of these sidewalls is one of the factors that causes pattern deterioration above 12 GHz [6] - [8], [13]. The removal of the *E*-plane sidewalls led to reduced low-frequency gain and increased low-frequency VSWR. In [14] it was shown that when the coax-to-waveguide launcher is designed correctly grids that are thick enough to be self-supporting can be implemented without causing pattern deterioration while retaining good low-frequency performance. An adjustable metallic grid is used in [23]. It is, however, unclear whether continuous adjustment of the sidewalls is required to realise the claimed operational bandwidth of this antenna (25:1 bandwidth, 0.8-20 GHz).

In [12] it was observed that there was significantly more surface current on the flares of the DRGH above 12 GHz. The hypothesis was that it was these surface currents that caused pattern deterioration. To solve this problem a High Impedance Surface (HIS) was implemented on the *H*-plane sidewalls using corrugations [12]. This did improve the radiation patterns, but from the graphs presented it is clear that it did not solve the problem completely. The author suspects that the increased surface current on the flares above 12 GHz is most likely due to higher-order modes and that it is these modes that are the cause of the pattern deterioration.

In [9] structures are added to the four corners of the flared waveguide, basically removing the sharp inside corners and rounding them. It is claimed that this can improve the radiation patterns.

2.3.4 Ridges

As mentioned before, ridges were introduced in both the coax-to-waveguide launcher and flared waveguide assembly to increase the MUB by lowering the cut-off frequency of the TE_{10} mode, see Figure 2.9. The ridges start inside the coax-to-waveguide launcher assembly and extend into the flared waveguide assembly formed by the sidewalls. The ridges typically terminate at the horn aperture, although in some designs the ridges extend past the aperture to improve impedance matching [6] - [11], [13].

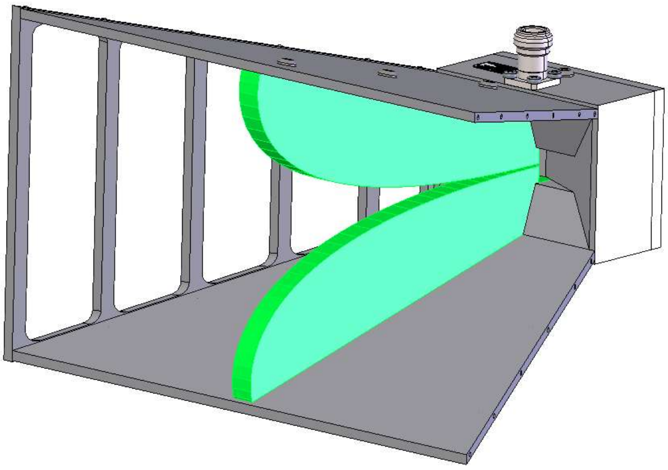

Figure 2.9. Ridges of the DRGH (green highlight), *E*-plane sidewall removed for clarity.

The profile of the ridges is designed to provide a smooth impedance transition from the ridged waveguide at the launcher to that of free space (377 Ω), [2], [38]. Various ridge profiles have been used over the years, for example: Linear, sinusoidal, quadratic, exponential, and exponential with a linear taper, elliptical, pole, spline and Bezier curves [2], [14], [18], [24], [38], [52], [53]. It is important to note that the ridge profile can either refer to the physical coordinates of the points defining the ridge shape mechanically in space or the values of the impedance taper along the axis of the horn, starting at the wave impedance of the ridged waveguide feed point and ending at 377 Ω at the horn aperture.

Examples of ridge profiles defined as physical coordinates for exponential, exponential with a linear taper, elliptical and Bezier curves can be seen in [2], [14], [24]. Equation (2.1), from [54], defines a ridge profile with an exponential impedance taper.

$$Z(x) = Z(0)e^{kx} \qquad 0 \leq x \leq L \tag{2.1}$$

In (2.1) x is the distance from the interface between the coax-to-waveguide launcher and flared waveguide, along the horn axial length. The axial length of the antenna (distance between the coax-to-waveguide launcher aperture and the horn aperture) is L, and $Z(0)$ is the wave impedance of the ridged waveguide at $x = 0$. The impedance at point x is $Z(x)$ and k is defined in (2.2).

$$k = \frac{1}{L} ln\left(\frac{Z(L)}{Z(0)}\right) \tag{2.2}$$

A slightly different formulation is given in (2.3) and (2.4), from [38], where L is the axial length of the ridge, $Z_{0\infty}$ is the characteristic impedance of the waveguide and k is a constant such that the impedance at the midpoint of the flared assembly is the average of the endpoint impedances.

$$Z = Z_{0\infty}e^{kx} \qquad 0 \leq x \leq \frac{L}{2} \tag{2.3}$$

$$Z = 377 + Z_{0\infty}(1 - e^{k(L-x)}) \qquad \frac{L}{2} \leq x \leq L \tag{2.4}$$

Experimentally it was found that this exponential profile provided satisfactory results. If the ridge profile is defined as impedances, it is necessary to use the transverse resonance method, see Section 2.5.1, to calculate the physical coordinates (ridge gap along the axial length) from the impedance profile.

Historically the exponential profile was preceded by a short straight section. Experimentally it was found that this prevented excitation of the TE_{20} mode and provided a smooth impedance taper from the ridged waveguide to free space [38]. In most cases, the linear part starts at the feed point and ends at the point where ridges come out of the coax-to-waveguide launcher [8] (i.e. the interface between coax-to-waveguide launcher and the flared waveguide).

The traditional 1-18 GHz ridge profile is based on the 1-12 GHz Kerr DRGH profile given in [2]. The Kerr, 1-12 GHz ridge profile has a 25.4 mm straight section followed by an exponential plus linear taper. In [38] it was found that as the MUB of the DRGH antenna is increased, VSWR peaks appear in the low band and increase in height and number. No explanation for this result could be found, but it was found that a linear taper superimposed on the logarithmic curve improved the VSWR in the first octave of the frequency band for the 1-12 GHz DRGH designed in [2]. The Kerr ridge profile shown in Fig 3 of [2] is approximated by (2.5) where x is the distance in mm along the horn axial length starting at the end of the ridge's straight section and $f(x)$ is the perpendicular distance in mm from the centre line of the horn. Note that this is a physical (height) ridge profile, not an impedance profile.

$$f(x) = 0.6382 \cdot e^{0.030585x} + 0.02x \tag{2.5}$$

According to [8] replacing a part of the exponential profile near the horn aperture with a circular section can improve the impedance matching. This is based on the aperture-matched profile of a pyramidal horn suggested by [55] and the redesigned DRGH in [6], [7].

Ridges were mostly implemented with constant width due to ease of fabrication. The width of the ridges can be used to ensure single-mode propagation in the flared section of the waveguide [38]. Also, according to [38] a constant ridge width in a short axial length DRGH causes an undesirable peaked amplitude distribution in the *H*-plane and large phase error in the *E*-plane which will result in reduced gain. Recently, tapered ridges have been shown to improve the radiating characteristics of DRGH antennas [22], [25]. Several tapered-width ridges were investigated: constant, Klopfenstein and linear. It was found that the best performance could be achieved using a linear ridge taper. Adding structures to the ridges at the feed point has been shown to improve the radiation pattern and impedance matching [56].

2.4 MANUFACTURING METHODS AND MATERIALS

Historically most of the parts and or sub-assemblies of DRGH antennas were manufactured from metal using subtractive manufacturing methods such as machining. Complex sub-assemblies like the coax-to-waveguide launcher are either manufactured with 5-axis CNC machines [14] or assembled from multiple parts which are fastened together using normal fasteners like screws. The fasteners are usually made from Stainless Steel (SS) 316 due to better corrosion resistance. This can however lead to gaps between parts and sub-assemblies that can cause resonances in gain and VSWR [16], [17]. For the design presented in [14] and shown in Figure 2.3, all the parts (except for the commercially available RF connector) were manufactured using machining. A CNC lathe was used to manufacture the feed pin in brass, this part was then gold-plated and soldered into the solder bucket of the RF connector. The rest of the parts were manufactured in aluminium using normal CNC milling machines, except for the coax-to-waveguide launcher that required a 5-axis CNC milling machine.

Typically, the aluminium parts are then surface treated with a chromate conversion coating. For environmental considerations, this should be a non-hexavalent chromate conversion coating. Aluminium is used since this material has a low electrical loss, is lightweight and machine very easily. The drawback is that aluminium is not solderable. This can be solved by using other materials like brass or copper where needed or coating the aluminium with nickel plating. If nickel plating is used care should be taken that the coating is not overly lossy, especially at high frequencies.

A crucial aspect of the DRGH assembly is how to properly terminate the feed pin in the bottom ridge. As was shown previously gaps at the feed point can lead to severe performance deviations [16], [17]. In [14] a collet with eight spring fingers, removed from a precision N-type connector female contact, was press-fitted into the bottom ridge, see Figure 2.4. It was also found that once the pin is securely inserted into this collect, applying silver epoxy to fill all the voids can ensure that no gaps are present. If the bottom ridge is made from a solderable material (for example copper or brass) or plated with a solderable material (for example nickel or gold) the feed pin can be soldered to the bottom ridge, for added strength there should be a small hole in the ridge so that a portion of the pin fits into the ridge. A portion of the bottom ridge can also be replaced with a piece of solderable material mechanically attached using for example screws to the bottom ridge, but again care needs to be taken to ensure that there are no gaps between the parts after assembly.

If very accurate machining tolerances can be achieved the feed pin can be press-fitted into a hole in the bottom ridge. If the desired fit is not achievable, conductive epoxy can be used to glue the pin into the bottom ridge hole. The feed pin can be machined to have a threaded section on the bottom end that can thread into a threaded hole on the bottom ridge. It is advisable to use conductive epoxy to ensure that there are no gaps between the threads. If the bottom ridge has a hole for the feed pin, another hole perpendicular to the feed pin one can be drilled up to the feed pinhole and threaded. Then a grub screw can be used to fasten the feed pin. Again, it is advisable to use conductive epoxy to ensure that there are no gaps between the feed pin and feed pin hole. Also, use of a thread locker is advisable for the grub screw.

As mentioned before the *E*-plane sidewalls of the DRGH can be manufactured using Printed Circuit Board (PCB) methods, i.e. as thin grids etched on a dielectric substrate, typically copper on PolyTetraFluoroEthylene (PTFE) or FR4 (glass-reinforced epoxy laminate material).

The rapid progress and now widespread availability of AM has made this the method of choice for rapidly manufacturing low-cost parts and prototypes. This has also been true for the manufacturing of horn antennas [47], [57] - [70]. Plastic 3D printed parts are manufactured in a plethora of different plastic materials using methods such as Selective

Laser Sintering (SLS) [64], Fused Deposition Modelling (FDM) [65], [66], [70] or resin printing using for example Stereolithography (SLA) [58], [61], [65], [71] or Digital Light Processing (DLP) [70]. Examples of materials typically used include Acrylonitrile Butadiene Styrene (ABS) [59], [62], [68], [70], [71], PolyLactic Acid (PLA) [65] - [67], [70] and nylon [64]. Choosing the correct material and printing method for the part being printed will depend on a host of factors, a discussion of which is beyond the scope of this study.

To create conductive surfaces on the printed plastic parts various methods have been used, for example; conductive tape [62], [66], conductive epoxy [58], conductive paint applied with a brush or aerosol (spray painting) [57], [59], [62], [65], [67] - [70], vacuum metallisation [70], electroplating [61], [65], [70] and electro-less plating [71]. Typical materials used for the conductive layer were copper [61], [62], [64], [65], [67], [70], silver [57] - [70], nickel [59], [68], [71], gold [71] and aluminium [66]. For proper performance, it is important to ensure that the applied conductive layer is significantly thicker than the skin depth at the lowest frequency of operation [65], [70].

Some studies have also used metal 3D printing, typically using Direct Metal Laser Sintering (DMLS) or Selective Laser Melting (SLM) and printing in aluminium or copper [47], [63], [71]. These parts are usually stronger and have better surface finish but are more expensive and weigh more than plastic parts.

Apart from being fast and cost-effective, 3D printing can be used to manufacture more complex structures without the need for multiple parts requiring assembly. With the right design methods, for example including small perforations in various parts of the antenna or printing parts with fill factors instead of solid, these parts can be made to be extremely lightweight [61], [71].

One drawback with 3D printing is a rougher surface finish than what can easily be achieved with machining. Poor surface roughness can lead to additional losses at high frequencies due to the skin effect. The rough surface of 3D printed parts can be improved by mechanical means such as machining, sanding, sand or bead blasting, or chemical methods for example using acetone to smooth parts printed in ABS.

The widest bandwidth DRGH antennas manufactured with 3D printing in literature were 9:1 (2-18 GHz), [47], [61].

2.5 METHODS OF DESIGN AND ANALYSIS

Historically the basic design of horn antennas was done using analytical and semi-analytical methods such as the aperture, transverse resonance [35], [36], [72] and mode matching [73] - [76]. Due to the limitations of these methods, the DRGH antenna mostly had to be designed by experimentation [2], [38]. More recently with the advent of computers the design and analysis of this type of antenna is done almost exclusively with Computational ElectroMagnetic (CEM) techniques. Initial implementations were limited to very simple problems using methods such as the UTD (Uniform Theory of Diffraction) [55] and two-dimensional (2D) formulations of the MoM (Method of Moments) [77].

The increase in computational power and improvement in the numerical techniques have led to the development of powerful commercially available electromagnetic software packages such as FEKO and CST [27], [28]. In the following sections, the design of horn antennas with these various methods is briefly discussed.

2.5.1 Analytical and Semi-Analytical Methods

Maxwell's equations describe the interaction and behaviour of electromagnetic fields. The solution to these equations is, however, complex and exact analytic solutions exist for only a small number of simple problems. Before the advent of computers, complex EM problems had to be reduced to problems that could be analysed with analytical or semi-analytical methods. Thus, although the method used to analyse the problem might be exact (or nearly exact), usually the problem is simplified. As was mentioned previously ridges can be used in rectangular waveguides to lower the cut-off frequency of the fundamental mode and increase the MUB. A single, double or quad ridge can be used. If dual polarisation is required with one antenna, quad ridges are used, while for single polarised horn antennas, the double ridge geometry is typically used.

The transverse resonance method is an example of a semi-analytical method used to calculate the cut-off frequency of the modes, the impedance and attenuation in double ridged waveguide [35], [36], [72], [78], [79]. This method approximates the double-ridged structure with a circuit model that includes capacitive susceptance for the effect of the fringing field from the step discontinuity formed by the ridge edges and for the capacitive effect of the gap between the ridges and the gap between the waveguide next to the ridges. The double-ridged waveguide cross-section geometry and the equivalent circuit model are shown in Figure 2.10(a) and Figure 2.10(b), respectively.

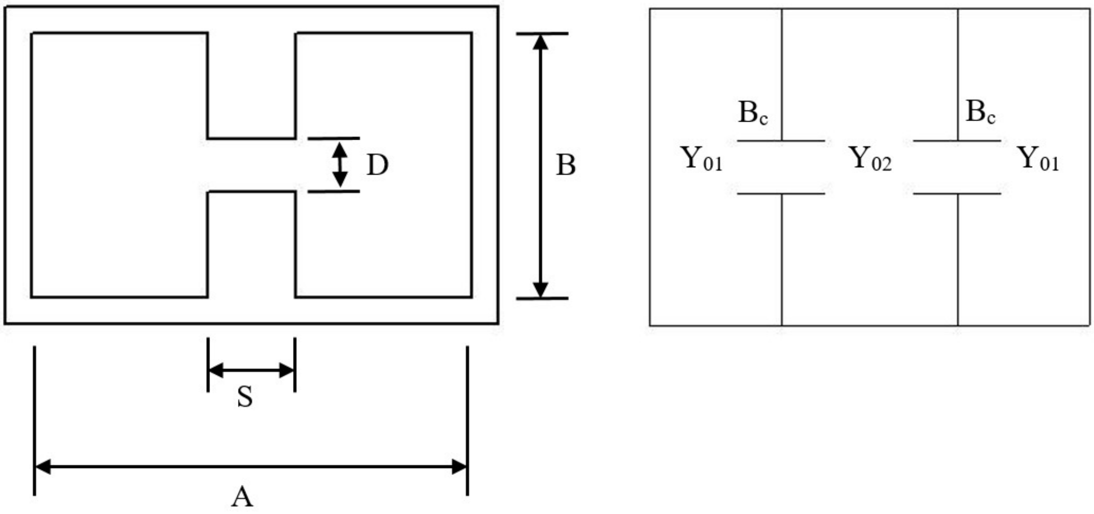

(a) (b)

Figure 2.10. (a) Ridged waveguide and (b) equivalent circuit from [17].

For the following equations, the notation as used in [38] was followed with *A* the waveguide width, *B* the waveguide height, *D* the ridge gap and *S* the ridge width as shown in Figure

2.10(a). Equations were given in [35] and [36] for the cut-off frequency of various TE_{no} modes as well as the wave impedance of the double-ridged waveguide at a specific frequency. The equations for the cut-off (λ_c) wavelength of the TE_{no} modes are given by (2.6) to (2.9).

$$\frac{B}{D}tan\theta_2 - cot\theta_1 + \frac{B_c}{Y_{01}} = 0 \tag{2.6}$$

$$\frac{B}{D}cot\theta_2 + cot\theta_1 - \frac{B_c}{Y_{01}} = 0 \tag{2.7}$$

where

$$\theta_1 = \frac{\pi(A-S)}{\lambda_c} = \pi\left(1-\frac{S}{A}\right)\left(\frac{A}{\lambda_c}\right) \tag{2.8}$$

$$\theta_2 = \frac{\pi S}{\lambda_c} = \pi\left(\frac{S}{A}\right)\left(\frac{A}{\lambda_c}\right) \tag{2.9}$$

Equation (2.6) applies to the TE_{no} modes where n is odd and (2.7) where n is even. The waveguide admittances Y_{01} and Y_{02} are defined in (2.10) to (2.12), see [80].

$$Y_{01} = \frac{\kappa_x}{\omega\mu}\frac{1}{B} \tag{2.10}$$

$$Y_{02} = \frac{\kappa_x}{\omega\mu}\frac{1}{D} \tag{2.11}$$

$$\frac{Y_{02}}{Y_{01}} = \frac{B}{D} \tag{2.12}$$

In (2.10) and (2.11) κ_x is the propagation constant perpendicular to the waveguide cross-section (defined as the x direction) for the cut-off frequency given by (2.13).

$$\kappa_c = \frac{2\pi}{\lambda_c} \tag{2.13}$$

The $\frac{B_c}{Y_{01}}$ term in (2.6) and (2.7) models the step discontinuity on both sides of the ridges and approximations for this term can be found in [72], [78], [81]. In [78] the discontinuity capacitance term is given in Equation 8. From this equation, the discontinuity susceptance term $\frac{B_c}{Y_{01}}$ is derived, with the result shown in (2.14) and (2.15).

$$\frac{B_c}{Y_{01}} = \frac{2B}{\lambda_c}\left[\frac{\alpha^2+1}{\alpha}cosh^{-1}\left(\frac{1+\alpha^2}{1-\alpha^2}\right) - 2ln\left(\frac{4\alpha}{1-\alpha^2}\right)\right] \tag{2.14}$$

with

$$\alpha = \frac{D}{B} \tag{2.15}$$

Equation (2.14) applies to a single-ridged waveguide, for a double-ridged waveguide (2.14) should be divided by 2. Another approximation, see [72], [81], for the discontinuity susceptance term of double-ridged waveguide is given in (2.16).

$$\frac{B_c}{Y_{01}} \approx 2\left(\frac{B}{A}\right)\left(\frac{A}{\lambda_c}\right) ln\left[cosec\left(\frac{\pi D}{2B}\right)\right] \tag{2.16}$$

The natural logarithm term in (2.16) is also sometimes approximated as shown in (2.17), see [72], with α again being defined as in (2.15).

$$ln\left[cosec\left(\frac{\pi\alpha}{2}\right)\right] \approx \frac{1}{2}\left[\left(\frac{1+\alpha^2}{\alpha}\right) l\,n\left(\frac{1+\alpha}{1-\alpha}\right) - 2ln\left(\frac{4\alpha}{1-\alpha^2}\right)\right] \tag{2.17}$$

One closed-form expression for the cut-off space of the dominant TE_{10} mode in a double-ridged waveguide is given by (2.18) from [72], [82].

$$\frac{B}{\lambda_c} = \frac{B}{2(A-S)}\left[1+\frac{4}{\pi}\left(1+0.2\sqrt{\frac{B}{A-S}}\right)\frac{B}{A-S}\ln\left(cosec\left(\frac{\pi}{2}\frac{D}{B}\right)\right) + \left(2.45+0.2\frac{S}{A}\right)\frac{SB}{D(A-S)}\right]^{-1/2} \tag{2.18}$$

According to [72], [82] this representation agrees with numerical methods within 1% provided that the following conditions are met:

$$0.01 \leq \frac{D}{B} \leq 1$$

$$0 \leq \frac{B}{A} \leq 1$$

$$0 \leq \frac{S}{A} \leq 0.45$$

For comparison to the graphs plotted in [36], (2.18) can be re-written using (2.19) from [82].

$$\frac{\lambda_c}{\mathrm{A}} = \frac{B}{A} \cdot \left(\frac{B}{\lambda_c}\right)^{-1} \tag{2.19}$$

Walton and Sundberg implemented (2.6) to (2.9) and the approximation of the fringing capacitance as given in (2.14) and (2.15) on a Personal Computer (PC) and calculated several curves that can be used to design the ridges for the coax-to-waveguide launcher assembly of a DRGH antenna [38].

The characteristic impedance for the TE_{10} mode in ridged waveguides at infinite frequency, $Z_{0\infty}$ can be calculated using (2.20) and (2.21) from [38] and is based on the derivation in [35] using the transverse resonance method.

$$Z_{0\infty} = \frac{1}{Y_{0\infty}} \tag{2.20}$$

$$Y_{0\infty} = 2\sqrt{\frac{\varepsilon}{\mu_0}}\frac{\lambda_c}{2\pi D}\left\{\frac{2D}{\lambda_c}cos^2\left(\frac{\pi S}{\lambda_c}\right)\ln csc\left(\frac{\pi D}{2B}\right)+\frac{\pi S}{2\lambda_c}+\frac{1}{4}sin\left(\frac{2\pi S}{\lambda_c}\right)\right.$$
$$\left.+\frac{D}{B}\frac{cos^2\left(\frac{\pi S}{\lambda_c}\right)}{sin^2\left(\frac{\pi}{\lambda_c}(A-S)\right)}\left[\frac{\pi(A-S)}{2\lambda_c}-\frac{1}{4}sin\left(\frac{2\pi(A-S)}{\lambda_c}\right)\right]\right\} \tag{2.21}$$

$$Z_0(f) = \frac{Z_{0\infty}}{\sqrt{1-\left(\frac{f_c}{f}\right)^2}} \tag{2.22}$$

Walton and Sunberg used (2.20) to (2.22) to calculate the wave impedance (Z_0) of the ridged waveguide at a required frequency (f) with f_c the cut-off frequency of the TE_{10} mode [38]. The same approach was also used by [18] to design the ridged waveguide launcher of a 1-14 GHz DRGH antenna. When (2.6) to (2.9) are used Newton's method can be used to calculate λ_c/A for the TE_{10} mode using the desired ridged waveguide dimensions, whilst (2.18) can be used to provide a good initial guess. Using the calculated value of λ_c/A the impedance can be calculated as above. This process is then repeated for the TE_{20} and TE_{30} modes. Subsequent modes are found from the higher roots to (2.6) and (2.7) [35]. Assuming that the TE_{20} is not excited (see Section 2.3.4) then the MUB is the ratio of the TE_{30} and TE_{10} mode cut-off wavelengths, i.e. $\lambda_c^{10}/\lambda_c^{30}$.

The estimated characteristic impedance of the ridged waveguide, at infinite frequency, can also be determined by calculating the power, P, carried by the ridged waveguide see (2.23) to (2.27) from [36], [54] for double-ridged waveguide.

$$P = \sqrt{\frac{\varepsilon_0}{\mu_0}\frac{E_0^2}{2\pi}\frac{\beta\lambda_c^2}{k}}\left(\frac{2\beta}{k}cos^2\left(\frac{\pi\gamma}{k}\right)ln\left(cosec\left(\frac{\pi D}{2B}\right)\right)+\frac{\pi\gamma}{2k}+\frac{1}{4}sin\left(\frac{2\pi\gamma}{k}\right)\right.$$
$$\left.+\frac{D}{B}\frac{cos^2\left(\frac{\pi\gamma}{k}\right)}{sin^2\left(\frac{2\pi\delta}{k}\right)}\left[\frac{\pi\delta}{k}-\frac{1}{4}sin\left(\frac{4\pi\delta}{k}\right)\right]\right) \tag{2.23}$$

$$\beta = \frac{D}{A} \tag{2.24}$$

$$\gamma = \frac{S}{A} \tag{2.25}$$

$$k = \frac{\lambda_c}{A} \tag{2.26}$$

$$\delta = \frac{\left(1-\frac{S}{A}\right)}{2} \tag{2.27}$$

After calculating the power from (2.23) to (2.27), the impedance at an infinite frequency can be calculated from (2.28), see [36], [54].

$$Z_{0\infty} = \frac{V_0^2}{2P} = \frac{E_0^2 D^2}{2P} \tag{2.28}$$

In (2.28) V_0 is the peak voltage across the centre of the ridge gap and P is the average power carried by the ridged waveguide. The characteristic impedance at any other frequency can then again be calculated using (2.22).

An alternative equivalent circuit formulation can be seen in Figure 2.11(a) and Figure 2.11(b) from [20], [54], [83] - [85]. The total capacitance per unit length of the ridged waveguide, C (F/m), can be calculated from the electrostatic capacitance C_s and the discontinuity capacitance C_d, see (2.29).

$$C = C_s + 2C_d \tag{2.29}$$

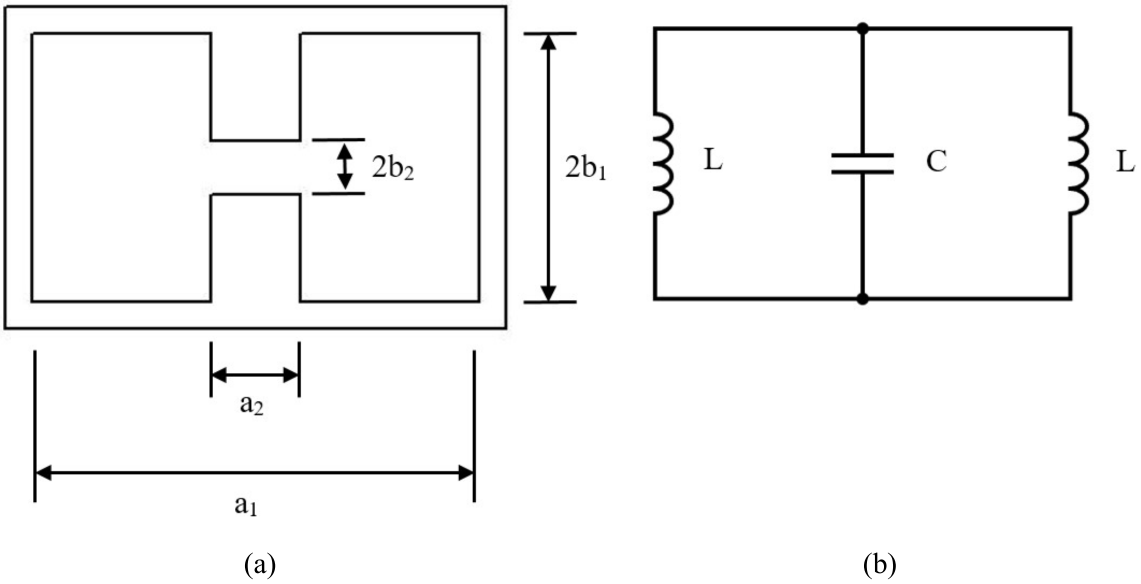

Figure 2.11. (a) Ridged waveguide and (b) alternative equivalent circuit formulation.

The electrostatic capacitance C_s for a double-ridged waveguide is given by (2.30). Note that the equations below consider the general case where the waveguide can be filled with a dielectric material.

$$C_s = \frac{\epsilon a_2}{2b_2} \tag{2.30}$$

The discontinuity capacitance C_d for a double-ridged waveguide is given by (2.31) and (2.32).

$$C_d = \frac{\epsilon}{2\pi}\left[\frac{x^2+1}{x} cosh^{-1}\left(\frac{1+x^2}{1-x^2}\right) - 2ln\frac{4x}{1-x^2}\right] \tag{2.31}$$

$$x = \frac{b_2}{b_1} \tag{2.32}$$

The inductance for a double-ridged waveguide, *L,* is given by (2.33).

$$L = \mu(a_1 - a_2)b_1 \tag{2.33}$$

Using the results from (2.29) to (2.33) the cut-off frequency is then given by (2.34).

$$f_c = \frac{1}{2\pi\sqrt{(L/2)C}} = \frac{1}{\pi\sqrt{\mu\epsilon}\sqrt{\left(\frac{a_2}{b_2} + \frac{2C_d}{\epsilon}\right)(a_1 - a_2)b_1}} \tag{2.34}$$

Equation (2.34) simplifies significantly if the discontinuity capacitance C_d is ignored as was done in [54], [84], [85]. For the equivalent circuit shown in Figure 2.11(b) the characteristic impedance at infinite frequency, $Z_{0\infty}$ is given by (2.35), see [83], where (2.8) and (2.9) can be used for ϑ_1 and ϑ_2 by replacing S with a_2 and A with a_1.

$$Z_{0\infty} = \frac{\sqrt{\frac{\mu}{\varepsilon}}}{\frac{2C_d cos\vartheta_2}{\epsilon} + \frac{1}{\pi}\frac{\lambda_c}{b_2}\left(sin\vartheta_2 + \frac{b_2}{b_1}cos\vartheta_2 tan\frac{\vartheta_1}{2}\right)} \tag{2.35}$$

In [80] a numerical study of the higher-order modes in double-ridged waveguide showed mode degeneration or the absence of the TE_{30} mode for specific dimensions. For these cases, the MUB is defined as the ratio of the TE_{10} and TE_{X1} modes with the TE_{X1} being the first higher-order mode that has maximum electric field intensity in the gap between the ridges [80].

Implementation of the transverse resonance method on a PC today requires minimal resources and allows calculation of the modes that will propagate in a matter of seconds. This method is not exact but approximates the double ridged structure with a circuit and therefore its use is limited to the design of very basic structures with more complex designs being performed using EM simulation.

A Matlab script implementing (2.6) to (2.15) and (2.20) to (2.22) was developed to calculate the cut-off frequencies and characteristic impedance of the double-ridged waveguide where necessary in the rest of the study.

2.5.2 EM Simulation

The analysis of more complex geometries requires the use of CEM techniques, numerical approximations of Maxwell's equations [86]. Each technique has certain drawbacks and advantages, requiring that the best technique based on the problem at hand be chosen. Numerical techniques can be divided into asymptotic and full wave techniques respectively. Asymptotic techniques assume certain physical approximations to Maxwell's equations which becomes more accurate and valid with an asymptotic increase in frequency. Full wave methods on the other hand do not make any initial approximations, but rather approximate Maxwell's equations numerically.

The three prominent full-wave techniques are the Method of Moments (MoM), Finite Difference Time Domain (FDTD) and Finite Element Method (FEM). These methods or variations thereof are implemented in the commercial EM software packages FEKO, CST and HFSS. Details about the methods and implementation of the methods are beyond the scope of this study, see [86] for a complete treatment of this topic.

Originally due to limited computational resources, asymptotic methods such as the UTD [55] were used to model the linearly flared waveguide of horn antennas. To model the profiled ridges 2D formulations of MoM were used [77]. The increase in computational power and improvement of commercial CEM software packages has, however, made it possible to use full wave techniques to model the whole DRGH antenna over extremely broad bandwidths. For very large horns that operate at high frequency, it is also possible to use an alternative formulation of MoM, the Multilevel Fast Multipole Method (MLFMM) [27]. It should be noted that the 1-18 GHz DRGH antenna itself has been implemented in all three of the previously mentioned software packages using full wave techniques and that currently the choice of which software package or technique to use depends more on available licenses and experience.

For the current study, MoM as implemented in FEKO was used extensively, with very limited use of CST. The main reasons for using FEKO are:

- The author has access to a large FEKO license pool, with extensive computational resources optimised for use with FEKO.
- The MoM code is a source method, only surfaces are discretised and not the volumes between structures. This method is therefore extremely efficient for models containing mostly conducting surfaces (Perfectly Electrical Conducting (PEC)). The MoM is well suited for radiating or scattering structures since it already incorporates the radiation condition. Homogeneous dielectric structures can be included in the MoM with the Surface Equivalence Principle (SEP) or Volume Equivalence Principle (VEP). Thus, MoM is ideal for DRGH antennas that contain few to no dielectric structures and consist of mostly conducting surfaces. Furthermore, MoM is very efficient in modelling small air gaps, as typically found in the feed region of DRGH antennas, without a dramatic increase in computation resources required.

Detailed implementation of the DRGH model in FEKO will be discussed in the respective design sections. As mentioned before, some use was made of CST, but only to calculate the modal content of non-standard double-ridged waveguide which cannot be done using MoM in FEKO.

2.6 CURRENT STATE-OF-THE-ART DESIGNS

In this section, several DRGH designs identified to have bandwidth ratios larger than 18:1 will be evaluated. Table 2.1 shows a comparison between these designs in terms of frequency range, bandwidth and whether the designs were verified with measurements on a prototype antenna or not. The first four designs only achieved incremental improvement over the 18:1

bandwidth, between 20:1 and 25.7:1. The last design achieved a significant improvement (83:1), but neither of the last two designs was verified with measurements on a prototype.

Table 2.1. DRGH Bandwidth comparison.

Reference	Frequency Range (GHz)	Bandwidth	Verified with measurements
[20]	2-40	20:1	Yes
[10], [11]	0.8-18	22.5:1	Yes
[23]	0.8-20	25:1	Yes
[13]	0.7-18	25.7:1	No
[26]	0.6-50	83:1	No

The 20:1 bandwidth design of [20], operates over the 2-40 GHz frequency band and is therefore significantly smaller than the typical 1-18 GHz DRGH [14]. It does not have any *E*-plane sidewalls and includes a dielectric lens. It has a standard empty rectangular box coax-to-waveguide launcher. The ridge design is also relatively standard with a constant ridge width and exponential ridge profile. Unlike conventional designs, it has slots cut into the ridges. The performance was verified with measurements on a prototype. The VSWR is nominally below 2:1, and the boresight gain increases nominally from 5 dBi at 2 GHz to 20 dBi at 40 GHz. It seems as if the design does not suffer from pattern deterioration at the high-frequency end.

The patent shown in [10] gives detailed design information for a 22.5:1 bandwidth design operating over 0.8-18 GHz. This antenna has full metal sidewalls with trapezoidal cuts in the *H*-plane sidewalls through which the ridges (called fins in [10]) protrude. The ridges have a constant width with a unique profile described in detail in [10]. The antenna is larger than the typical 1-18 GHz DRGH [14]. A small piece of carbon foam absorber is placed inside a cavity pocket formed by the flares of the coax-to-waveguide launcher directly behind the feed point and ridges. This antenna is available commercially as part number HF907 from Rohde & Schwarz with typical measured results shown in the datasheet [11].

Above 1.5 GHz the VSWR is below 2:1, between 0.8 and 1.5 GHz there is a VSWR peak that is between 2.5:1 and 3:1. The gain increases nominally from 5 dBi at 0.8 GHz to 12 dBi at 18 GHz, with a peak gain of nearly 15 dBi at 12.5 GHz. The datasheet claims that this antenna does not have any pattern deterioration, maintaining a single main lobe over the entire frequency range.

The design of [23] has adjustable metallic grid sidewalls compared to the fixed grid metallic sidewalls of the typical 1-18 GHz DRGH design [14]. It is, however, unclear whether continuous adjustment of the sidewalls is required to realise the full operational bandwidth of 25:1 (0.8-20 GHz). If adjustment of the sidewalls is required for different frequency bands then this would negate the wider bandwidth advantage claimed. The coax-to-waveguide launcher is mostly similar to traditional 1–18 GHz designs with flares [14]. However, the cavity pocket formed by the flares behind the feed has a cross-shaped structure that is claimed to suppress unwanted higher-order modes. The inner conductor also includes what is termed a small metallic cylindrical at the feed point, which was found to improve the VSWR. The performance was verified with measurements on a prototype. The VSWR is below 2:1 across the entire band and the boresight gain increases nominally from 6 dBi at 0.8 GHz to 14 dBi at 20 GHz with a peak gain of 17 dBi at 10 GHz. The design does not suffer from pattern deterioration at the high-frequency end.

Very little information is available for the 25.7:1 bandwidth (0.7-18 GHz) design presented in [13] and the simulated results were not validated with measurements on a prototype. Based on the available information the antenna is smaller, comparable in size to the 1–18 GHz design presented in [6], and it does not have any *E*-plane sidewalls. The profile of the ridges is also similar to that in [6] with a constant ridge width. The coax-to-waveguide launcher is mostly similar to traditional 1–18 GHz designs with flares [14]. The cavity pocket formed by the flares behind the feed is filled with a silicone magnetic absorber (ECCOSORB® FDS) similar to [10] resulting in reduced radiation efficiency. The VSWR is nominally below 2:1 (maximum of 2.5:1) and the gain increases nominally from 3 dBi at 0.7 GHz to 13 dBi at 18 GHz with a peak gain of 16 dBi at 15 GHz. It is claimed that this antenna does not have pattern break-up at high frequencies.

The design in [26] claims an 83:1 bandwidth (0.6-50 GHz). It uses a 2.4 mm connector to enable operation up to 50 GHz. Very few design details and dimensions are given, but from Fig 3 in [26], it can be inferred that the antenna is significantly larger than the typical 1-18 GHz DRGH antenna. It does not have any *E*-plane sidewalls and includes a dielectric Luneburg lens. The ridges of the antenna have a constant ridge width and a ridge profile defined using Bezier curves, similar to [14]. The coax-to-waveguide launcher is mostly similar to the traditional 1–18 GHz design with flares [14], however, perforations are made on all the sides of the launcher and a magnetic silicone absorber (ECCOSORB® GDS) with a thickness of 0.76 mm is placed on top of all the metal components of the coax-to-waveguide launcher. Effectively the launcher sub-assembly has an absorber coating. As mentioned the antenna was not manufactured and only simulated results are presented. The maximum VSWR is 2.7 at 0.6 GHz and above 1 GHz the VSWR is below 1.5:1. The gain increases from 2 dBi at 0.6 GHz to 18 dBi at 50 GHz with a peak gain of nearly 20 dBi near 20 GHz. Unfortunately, the antenna gain is presented in very large frequency steps, and it is highly likely that narrow dips in the gain could have been missed which usually is an indication of pattern break-up. The scale of the radiation pattern plots also makes evaluation of the plots very difficult. The patterns without a lens show very large performance deviations and or pattern of break-up at some frequencies (for example 30 GHz), which is not reflected in the gain results. Overall the radiation pattern performance of the few patterns shown looks poor with very large side lobes at the high-frequency end.

As can be seen from the discussion above, most of the extended bandwidth designs (beyond 18:1) include either a dielectric lens or absorber or both, which restricts the use of these designs to lower power applications and reduce radiation efficiency when using absorbers. The designs verified with measurements show only an incremental improvement of 20:1 to 25:1. For the 25:1 bandwidth design it is an open question of whether the bandwidth is achievable without adjustment of the sidewalls or if the sidewalls need to be adjusted for different bands. Only the 22.5:1 bandwidth design is available commercially. The two widest band designs 25.7:1 and 83:1 were not verified by measurements on a prototype and a lack of information makes it difficult to validate these designs.

2.7 SUMMARY

The background of the development of DRGH antennas from the very first horn antenna presented by Bose in 1897 up to the present was briefly discussed. The design of the DRGH antenna was then discussed in detail regarding the different constituent parts and sub-assemblies, manufacturing methods and materials as well as the design methods used. Specific emphasis was given to evaluating the design and performance of the current state-of-the-art DRGH antennas that have bandwidths beyond 18:1. Most of these designs only show incremental improvement and require the use of a dielectric lens or absorber or both. The design that does claim a significant increase in bandwidth suffers from a lack of information and the simulation results were not validated with measurements on a prototype.

CHAPTER 3 0.5-18 GHZ DRGH DESIGN

Typical anechoic chamber antenna measurement setups split the 0.5 – 18 GHz band into 0.5-2 GHz and 2-18 GHz with several DRGH antennas covering these frequency ranges used as source and reference antennas. To enable a single band measurement setup to cover the full 0.5-18 GHz band would require a 0.5-18 GHz DRGH. This chapter shows how the 1-18 GHz design from [14] was used to investigate what parts and or sub-assemblies of the DRGH limit the bandwidth and how these parts and or sub-assemblies can be redesigned to extend the DRGH bandwidth to 36:1 (0.5-18 GHz), [45].

The requirements to which the antenna must adhere are outlined in Section 3.1. Section 3.2 shows how the EM model of the 1-18 GHz DRGH was implemented in FEKO. The investigation into the design limits is shown in Section 3.3. The different parts and or sub-assemblies of the DRGH are removed or adjusted step by step and the effect on the performance is observed. The order of removal/adjustment was as follows: Coaxial feed, sidewalls, cavity and finally ridges. It was found that a redesign of the coax-to-waveguide launcher and ridges is required to extend the bandwidth.

Section 3.4 shows how the various parts and or sub-assemblies were redesigned to extend the bandwidth and ensure good performance. The final simulated results for the new 0.5-18 GHz DRGH design are also presented in Section 3.4. From this design a mechanical design, to enable the manufacture of a prototype was performed, see Section 3.5. Most of the parts for the prototype were manufactured using CNC machining, this excludes the commercial RF connector, fasteners and etched PCB *E*-plane sidewalls. The prototype was tested using an anechoic chamber and VNA. The measured results from these tests are presented in Section 3.6. The 36:1 bandwidth achieved is significantly more than predicted by theory. This result is investigated further in Section 3.7. Finally, the chapter is summarised in Section 3.8.

3.1 REQUIREMENTS

It is required that the 0.5-18 DRGH antenna be able to handle moderate to high power. This requirement precludes the use of an absorber or a dielectric lens [45] and will allow the antenna to be used for high-power EMC/I testing or jamming applications. To limit power being reflected back to the source an antenna with low VSWR is desired. As discussed in Section 2.6 the VSWR performance of current state-of-the-art antennas is typically below 2:1 with peaks between 2:1 and 3:1. Thus a maximum VSWR of 2.5:1 was set as the requirement.

The boresight realised gain should be 3 dBi or better at the low-frequency end and 14 dBi or better at the high-frequency end, similar to the current state-of-the-art DRGH antennas, see Section 2.6. For the radiation pattern performance, it was required that the main beam should not have any pattern breakup and side and back lobe levels should be similar to the design of [14]. The measured side and back lobe levels for the design of [14] can be seen in Figure 3.41 and are typically in the order of 20 dB over most of the frequency range. This would ensure magnitude and phase uniformity in the quiet zone of the anechoic chamber or test zone of an EMC/I test setup [87]. The cross-polar discrimination should be in the region of 25 dB to 30 dB or better to accurately measure circularly polarised antennas in an anechoic chamber when used as a source antenna [45].

3.2 EM MODEL OF 1-18 GHZ DRGH

The design of the 1-18 GHz DRGH, shown in Figure 2.3 and discussed in detail in [14], [17], is used as the basis for the investigation in this chapter. The final FEKO model used in [14] that produced the most accurate results in comparison to the final measured prototype is shown in Figure 3.1(a). This model uses the MoM to discretise the surfaces using PEC triangles. The dielectric part (PTFE) of the *N*-type connector is modelled using the SEP.

Apart from the feed assembly, the edge length of the triangles was set to *λ/3* (the minimum allowed in FEKO) at the highest simulated frequency. To more accurately model the circular feed assembly and feed point the edge length of the triangles for the outer and inner conductors was set to *λ/10* and *λ/20* respectively. The finer mesh was required not only to more accurately represent the geometry of these small features but also because these regions are highly sensitive [14], [16], [17].

Only a single symmetry plane can be used, that is magnetic symmetry in the *E*-plane along the horn axis, i.e. the y=0 plane, see Figure 3.1. Note that in FEKO the horn boresight is located along the x-axis. This orientation allows a direct comparison of FEKO θ and φ polarisations to the anechoic chamber measured *V*- and *H*-polarisations, respectively. The axis definition shown in Figure 3.1 is used further throughout this study. The origin is typically located, unless otherwise specified, at the centre of the feed point.

To improve the speed of the simulations this model was adjusted, as shown in Figure 3.1(b):

- The partial wall thicknesses added to the *E*- and *H*-plane flares were removed.
- The model of the N-type connector and most of the coaxial feed airline was removed, see Figure 3.2.
- The polygonal representation of the feed was changed to a cylindrical representation.
- The piecewise stepped ridge profile was changed to a smooth curve.

The number of triangles decreased from 13 382 to 12 372 and the complexity of the model was reduced by removing the only dielectric part. By further shortening the length of the feed to only 1 mm into the ridges, see Figure 3.2(c), the number of triangles could be reduced to 9704, a significant reduction given that the computational resource requirement for MoM scales with the number of unknowns. According to [86] the memory cost for each basis function scales for models with surfaces to the power of 4 and the run time to the power of 6, thus even a slight reduction in the number of triangles leads to a significant reduction in memory use and required run time.

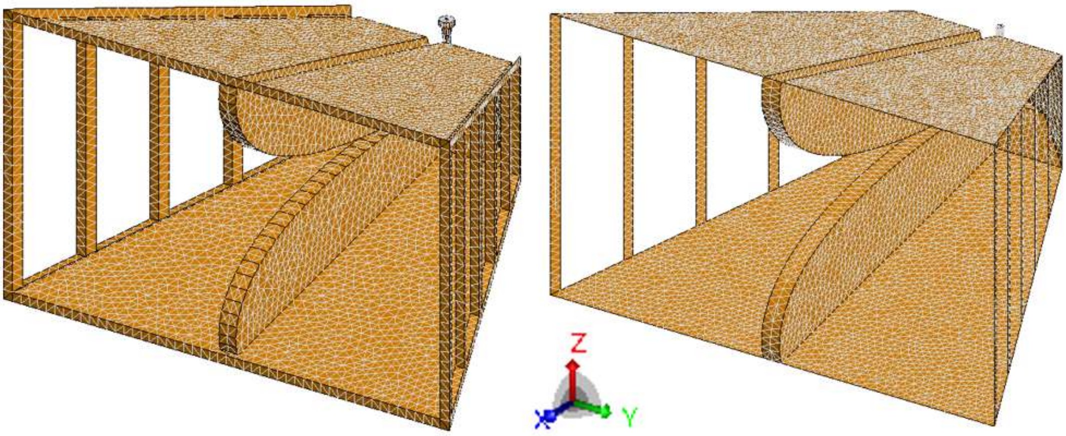

(a) (b)

Figure 3.1. (a) Meshed FEKO model of the original 1-18 DRGH and (b) reduced size model.

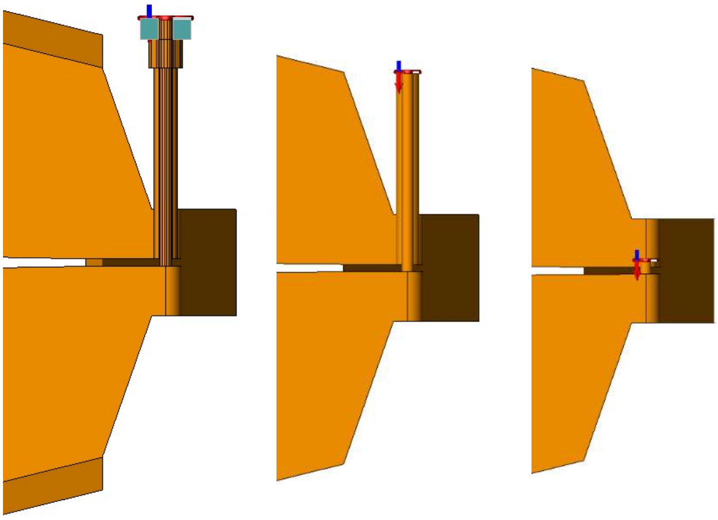

(a) (b) (c)

Figure 3.2. (a) Feed implementations of original full, (b) no N-type and (c) short, 1mm into ridge.

All three models were simulated and compared to typical measured results to verify that these changes would have a minor impact on accuracy, see Figure 3.3. The simulations were performed in 100 MHz steps from 500 MHz to 20 GHz so that the out-of-band performance for the 1-18 GHz design was also available for further use in Section 3.3.

As can be seen in Figure 3.3(a) for all the results the VSWR significantly degrades just below 1 GHz and just above 18 GHz. The boresight realised gain drops off quickly below 1 GHz and there is a deep dip in gain starting just after 18 GHz due to a combination of pattern breakup and VSWR losses, see Figure 3.3(b). These results confirm the usable bandwidth of this design as 18:1 (1-18 GHz) [14].

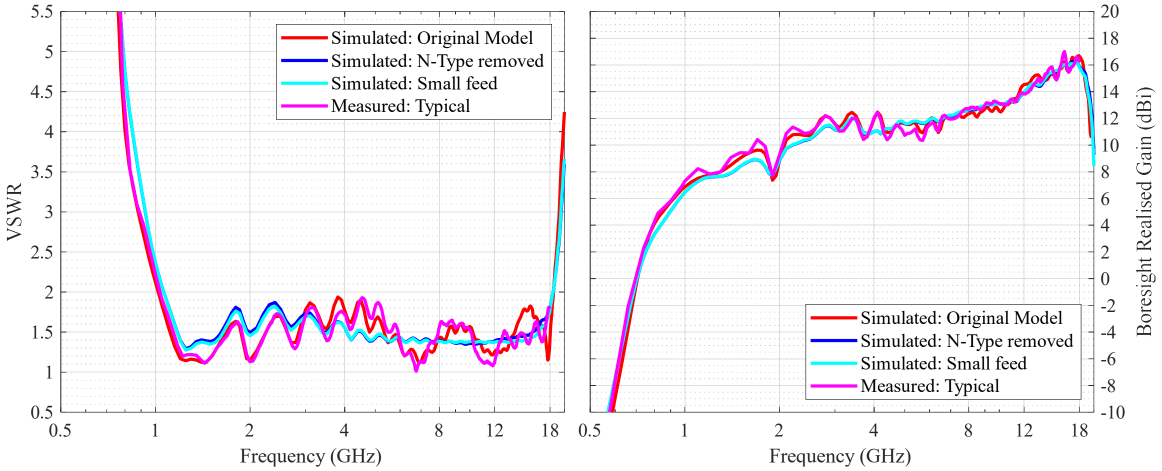

(a) (b)

Figure 3.3. (a) VSWR and (b) boresight gain comparison for different feed models.

In terms of the comparison between the different models, the original detailed model and the measured results compared very well with more ripple in both the VSWR, and gain compared to the size-reduced models. The VSWR and gain performance of the two size-reduced models compare very well to each other, following the nominal performance of the detailed model and measurements, but with reduced ripple. Further investigation using additional simulation models revealed the following:

- The VSWR ripple is mostly caused by an impedance mismatch between the N-type connector model and the coaxial line. As will be shown in Section 3.3.1, while the N-type is 50 Ω, the actual manufactured coaxial line impedance is 43 Ω. This appeared to be incorrect, but Section 3.3.1 also shows that the ridge impedance at the feed point is 32 Ω which explains why this value, found through experimentation, worked sufficiently well.

- The gain ripple, however, is mostly influenced by the thickness of the sidewalls. An observation that will be investigated further in Section 3.3.2 with regards to a related parameter i.e. the sidewall strip width.

Despite these differences, it was decided that the comparison to measured results for the reduced-sized model with a small feed is good enough so that this model can be used to investigate design limits.

3.3 INVESTIGATION INTO DESIGN LIMITS

In this section, the different parts and or sub-assemblies of the DRGH are removed or adjusted step by step and the effect on the performance is investigated. The order of removal/adjustment was as follows: Coaxial feed, sidewalls, coax-to-waveguide launcher and finally ridges. The reduced-sized FEKO model with a small feed described in the previous section was used as a starting point.

3.3.1 Coaxial Feed Investigation

In this section, the impact of the coaxial feed design on the DRGH performance was investigated. The coaxial feed starts with a precision N-type connector. For this connector, it should be noted that the maximum frequency of operation is 18 GHz and for a higher frequency of operation another connector would be required. SMA connectors are typically available for use up to 26.5 GHz, 2.92 mm up to 40 GHz and 2.4 mm connectors up to 50 GHz. The drawback with these high-frequency connectors is that power handling is reduced significantly.

For the design shown in Figure 2.3, the final outer conductor (hole in the ridge) diameter implemented was 3.3 mm and the inner conductor (feed pin) diameter was 1.6 mm. The characteristic impedance of a coaxial line is given by (3.1), see [75].

$$Z_0 = \sqrt{\frac{\mu}{\varepsilon}}\frac{ln\frac{\phi_{outer}}{\phi_{inner}}}{2\pi} \tag{3.1}$$

The cut-off frequency of the first higher-order mode can be calculated as shown below in (3.2) with c the speed of light.

$$f_c = \frac{c}{\pi\left(\frac{\phi_{outer}+\phi_{inner}}{2}\right)\sqrt{\mu_r\epsilon_r}} \tag{3.2}$$

The characteristic impedance is 43.4 Ω and not 50 Ω. The cut-off frequency is calculated as 38.98 GHz which is well above 18 GHz and thus the bandwidth is not limited by the coaxial feed, apart from the connector. Using the Matlab script (see Section 2.5.1) implementing the transverse resonance method the characteristic impedance of the ridges at the feed point is calculated as 32.5 Ω at the centre frequency of 9.5 GHz. The outer conductor of the FEKO model was thus changed to 2.75 mm, which would change the coaxial line impedance to 32 Ω, to improve the VSWR. The simulated result is shown in Figure 3.4 with the VSWR being below 1.5:1 nominally across the band. The cut-off frequency for this coax feed line design is calculated as 43.9 GHz.

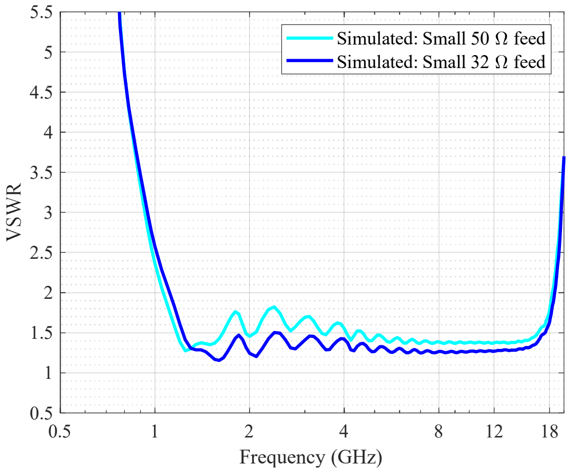

Figure 3.4. VSWR improvement with updated outer conductor design.

In summary, the precision N-type connector used on the 1-18 GHz DRGH limits the highest frequency of operation to 18 GHz. For higher frequency operation this connector can be replaced albeit with a reduction in the power handling ability.

The airline coaxial feed line cut-off frequency is well above 18 GHz and thus the coaxial feed design is not the bandwidth limiting factor in the 1-18 GHz DRGH design.

3.3.2 Sidewall Investigation

In this section, the effect of the two sidewalls of the flared waveguide assembly on the DRGH performance was investigated. The FEKO DRGH model with a small 32 Ω feed of the previous section was used as a starting point for this section. As was mentioned in Section 3.2, it was found that the finite thickness of the sidewalls caused a ripple in the boresight gain. To investigate this effect further the *E*-plane grid strip width was reduced to 1 mm. The 1-18 GHz DRGH design from [14] had thick grids (5.5 mm) to enable the grid structure to be self-supporting and robust without the use of a substrate, while historically the strip width of the traditional 1-18 GHz DRGH design was very thin, in the order of one or two mm [2].

The next test was to increase the strip-to-strip spacing between centres, also called the strip gap, to 60 mm (λ/10 at 0.5 GHz) from the original 40 mm (λ/10 at 0.75 GHz). To simulate a plane reflector the strip spacing should be in the order of λ/10. The simulated results of these parametric analyses are shown in Figure 3.5. Very little change is observed in the VSWR, see Figure 3.5(a), but the boresight gain ripple between 1.5 GHz and 4 GHz is improved by either reducing the strip width or increasing the strip gap, see Figure 3.5(b).

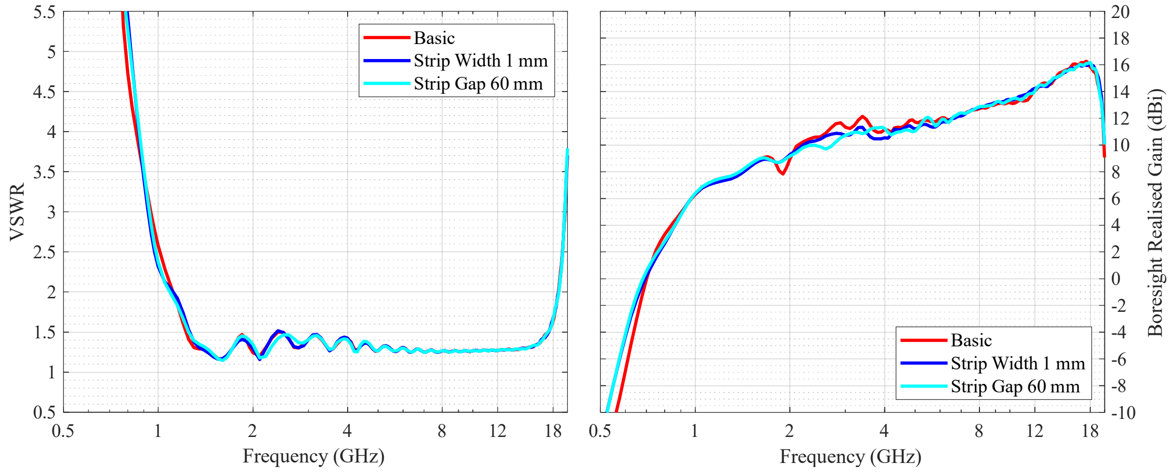

(a) (b)

Figure 3.5. (a) VSWR and (b) boresight gain comparison for the sidewall strip test.

For the next tests first the *E*-plane grid sidewalls and then both the *E*- and *H*-plane sidewalls were removed, these results are shown in Figure 3.6. Large ripples appear in the VSWR below 4 GHz, see Figure 3.6(a). As the sidewalls are removed, the boresight gain is reduced significantly between 0.7 GHz and 4 GHz, but above 4 GHz increases more smoothly, linearly when using a logarithmic scale for the x-axis, see Figure 3.6(b).

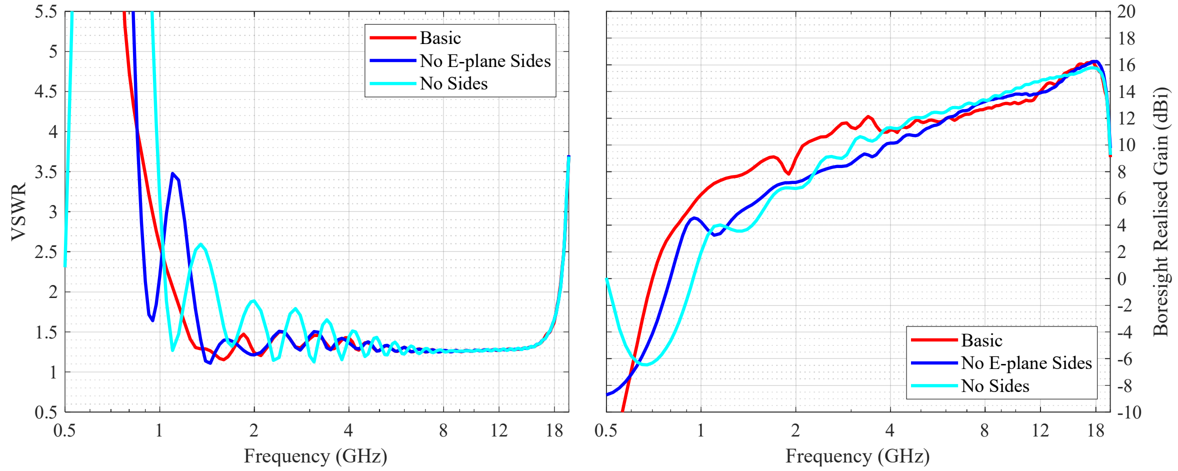

(a) (b)

Figure 3.6. (a) VSWR and (b) boresight gain comparison for the sidewall test.

Interestingly for the no-sidewall case, the antenna is well matched at 0.5 GHz and the boresight gain is nominally 0 dBi. This shows that if the impedance matching can be improved below 1 GHz it should be possible to extend the operational bandwidth lower in frequency. Overall, the sidewalls have a significant effect on the VSWR and gain performance below 4 GHz and a small effect on the gain above 4 GHz. It does look like the sidewalls affect the DRGH usable bandwidth with a decrease in performance and bandwidth when the sidewalls are removed.

3.3.3 Coax-to-Waveguide Launcher Investigation

For the first set of coax-to-waveguide launcher tests the model without any sidewalls was used from the previous section as starting point. The coax-to-waveguide launcher (referred to as the cavity in this section) was modified step by step, by removing parts of the cavity until there was no cavity remaining. The models are shown in Figure 3.7 from left to right, the basic model in Figure 3.7(a), the model with forward cavity flares removed in Figure 3.7(b), the model with inner cavity flares, apart from the section directly behind the ridge, removed in Figure 3.7(c), and the model without a cavity in Figure 3.7(d).

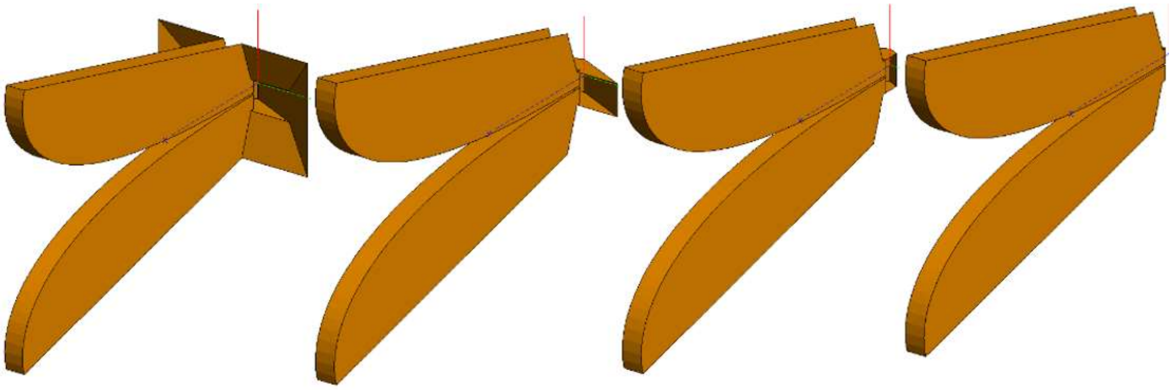

(a) (b) (c) (d)

Figure 3.7. (a) Basic model, (b) model with forward flares removed, (c) model with inner flares removed and (d) model without a cavity for the cavity investigation with no sidewalls.

The simulated VSWR and boresight gain results are shown in Figure 3.8(a) and Figure 3.8(b), respectively. Removing the first set of flares had very little influence on either the VSWR or gain. The VSWR is reduced significantly at the low end of the band for the test with just the section of the cavity behind the ridges and the test with the cavity removed completely. The gain shows a corresponding increase at the low end due to the reduced mismatch loss.

In the 8-18 GHz band there is a reduction in gain for the last two models without a significant corresponding influence on the VSWR. Above 18 GHz both the VSWR and boresight gain improves. Analysis of the three-dimensional radiation patterns at 20 GHz, see Figure 3.9, shows that the radiation pattern improves as the cavity is removed step by step. The beam behaves much better with a sharp reduction in side lobes for the ridges-only case.

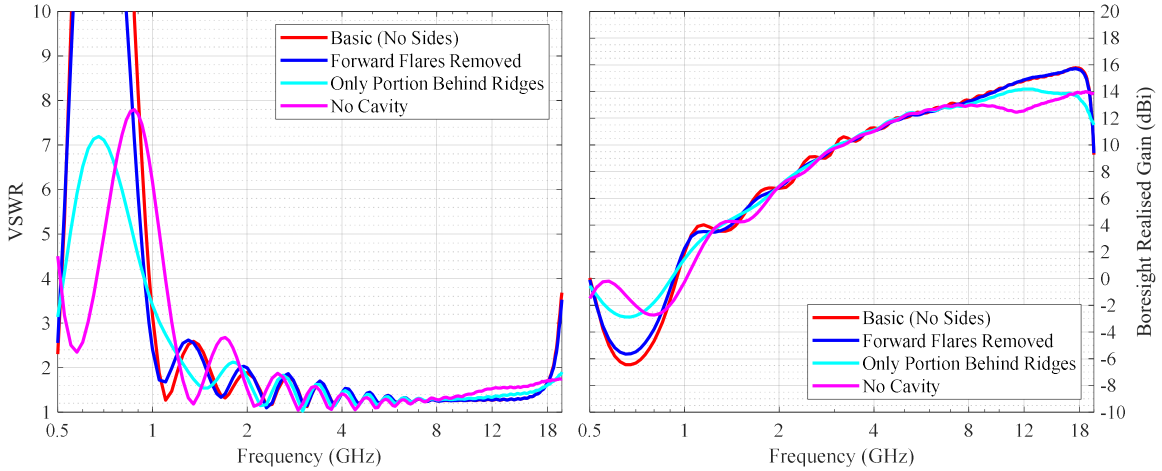

(a) (b)

Figure 3.8. (a) VSWR and (b) boresight gain comparison for the cavity investigation with no sidewalls.

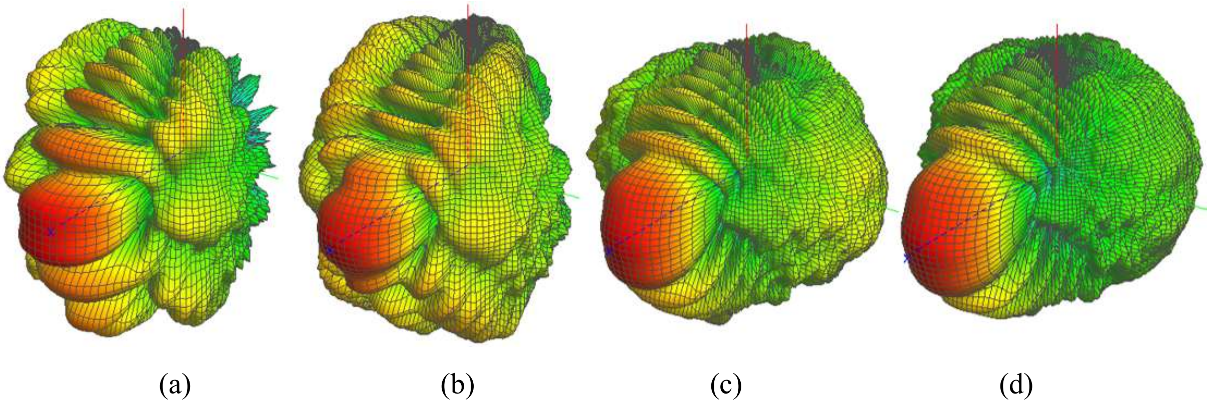

Figure 3.9. (a) Basic model, (b) model with forward flares removed, (c) model with inner flares removed and (d) model without a cavity radiation patterns (3D) at 20 GHz for the cavity investigation with no sidewalls.

For the next set of tests, the sidewalls were added again, i.e. the basic model from Section 3.3.2 was used as a starting point. The same cavity configurations were used as shown in Figure 3.7 with the simulated VSWR and boresight gain results shown in Figure 3.10(a) and Figure 3.10(b), respectively.

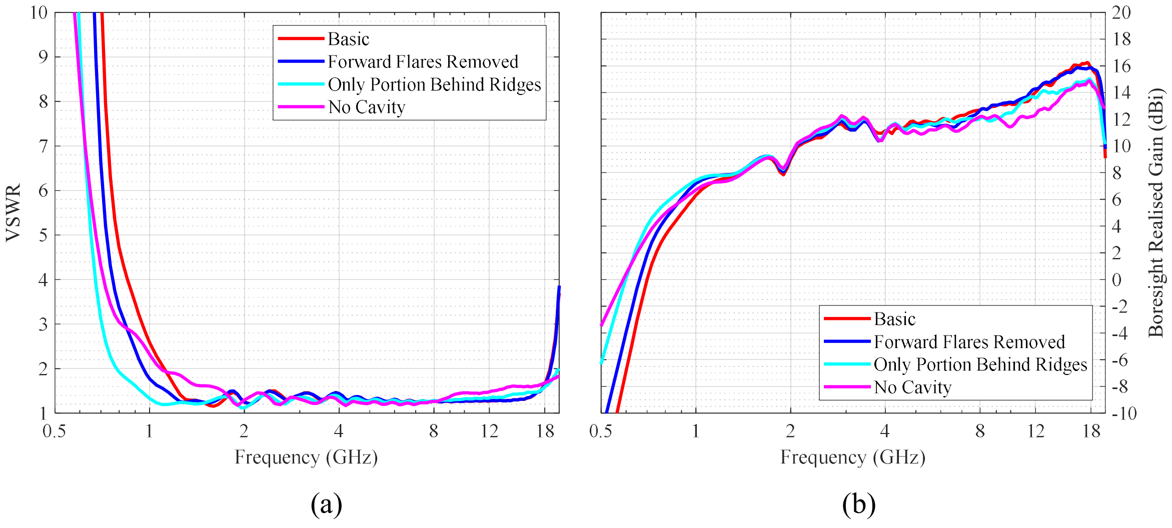

Figure 3.10. (a) VSWR and (b) boresight gain comparison for the cavity investigation with sidewalls.

Removing the forward cavity flares shifts the low-frequency operating point lower without a discernible effect of the high-frequency thus improving bandwidth. Further removal of the flares, keeping only the portion behind the ridges shifts the low-frequency operating point even lower, still with minimal effect at the high frequency. Removal of the full cavity shifts the low-frequency operating point upwards again. Also, the gain is reduced between 8 and 18 GHz but improved at 20 GHz. As shown in Figure 3.11 the pattern deterioration at 20 GHz in the basic model is improved significantly when removing the full cavity.

These results would seem to indicate that the cavity limits the bandwidth at the low end due to an impedance mismatch. At the high end, the cavity causes pattern deterioration above 18 GHz, either from not effectively suppressing higher-order modes or due to reflections from the cavity surfaces. If not all the energy is launched into the ridges, some of the backward travelling energy might lead to reflections from the cavity. A redesign of the cavity is necessary to improve the bandwidth of the DRGH with a bandwidth of at least 25:1 looking possible from Figure 3.10.

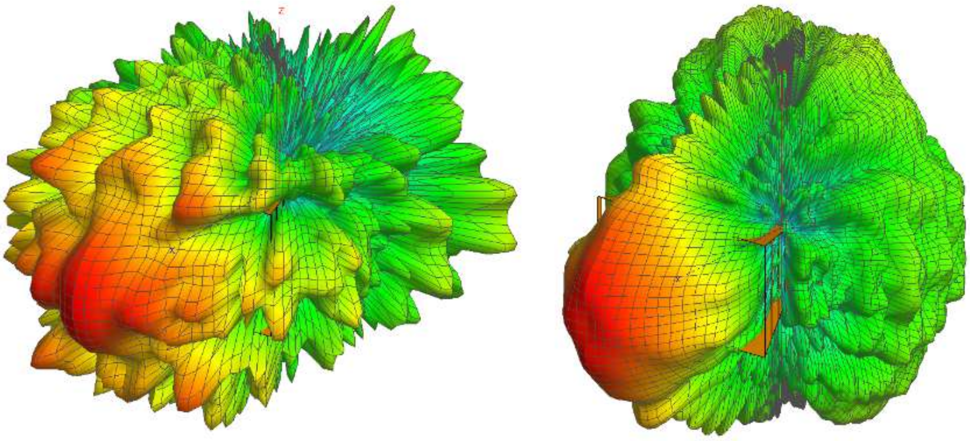
(a) (b)

Figure 3.11. (a) Radiation pattern (3D) basic model and (b) radiation pattern (3D) basic model with the full cavity removed at 20 GHz.

3.3.4 Ridge Investigation

Starting from the model in the previous section without sidewalls and ridges, the ridges were investigated, see Figure 3.12(a). First, the rear section of the ridges, that was left partially open/truncated by the removal of the cavity was filled, see Figure 3.12(b). Then a linear taper was applied to the ridge width similar to [25], increasing the width linearly along the horn axis from 10.6 mm to 70.42 mm. This modification is shown in Figure 3.12(c). Unlike [25] the ridge profile was not changed from a Bezier curve to an elliptical profile. The reason for wanting to perform this test is that apart from the performance improvements that can be gained as shown in [25] according to [38] the width of the ridges can be used to ensure single-mode propagation in the flared waveguide assembly and hence extend the bandwidth.

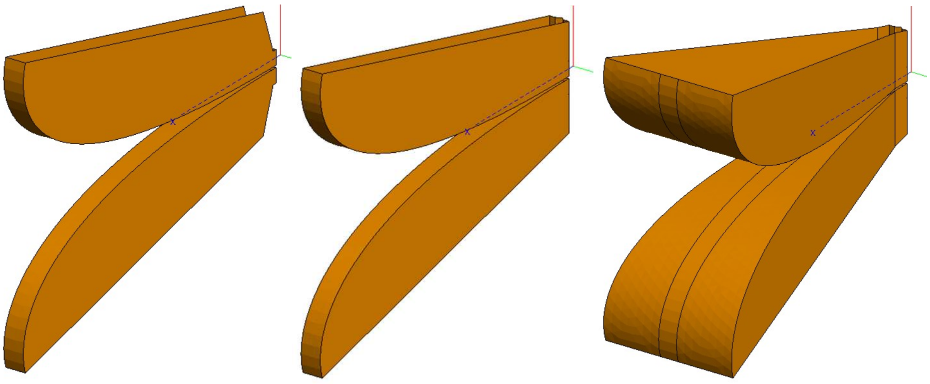

(a) (b) (c)

Figure 3.12. (a) Basic ridge model, (b) modified ridge model and (c) tapered modified ridge model.

The results are shown in Figure 3.13(a) and Figure 3.13(b). The VSWR is virtually unaffected by the change to the rear of the ridge, while the gain improves slightly around 12 GHz and reduces slightly around 20 GHz. The addition of the linear taper significantly improves VSWR and correspondingly the gain below 4 GHz. Above 4 GHz the VSWR is very similar to the other two models, but the gain improves significantly above 8 GHz. Thus adding the linear ridge width taper improved the bandwidth.

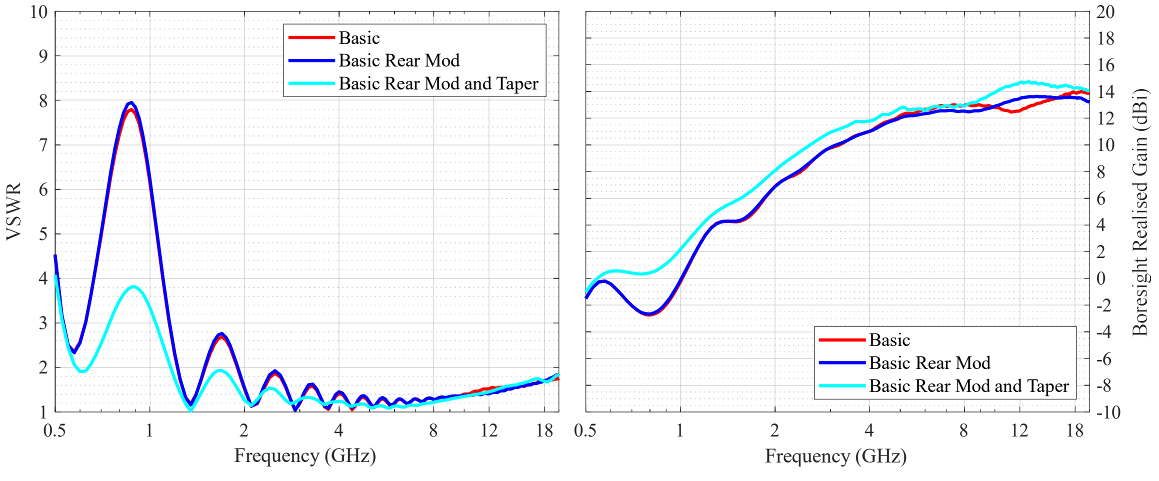

(a) (b)

Figure 3.13. (a) VSWR and (b) boresight gain comparison for the ridges only investigation.

This modification was then added to the initial model that included the cavity and sidewalls, see Figure 3.14(a) and Figure 3.14(b). The results of this test are shown in Figure 3.15(a) and Figure 3.15(b). The VSWR peaks increase slightly below 8 GHz, but the low-frequency cut-off shifts lower in frequency and the usable bandwidth increases to around 25.7:1 (0.7-18 GHz). As shown in [25] the gain above 8 GHz increases significantly due to the larger effective radiating aperture.

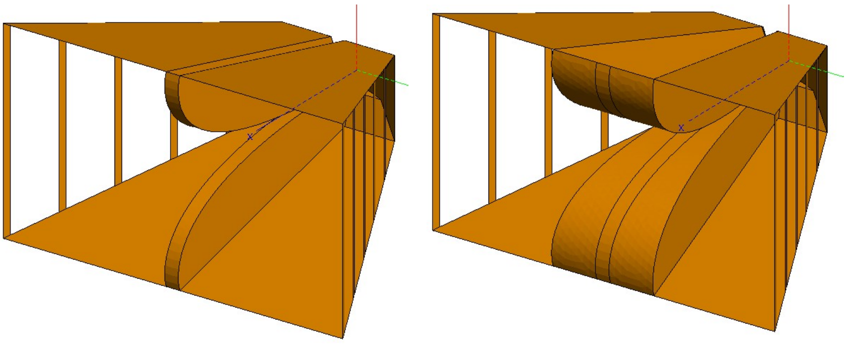

(a) (b)

Figure 3.14. (a) Basic model and (b) model with tapered ridge width.

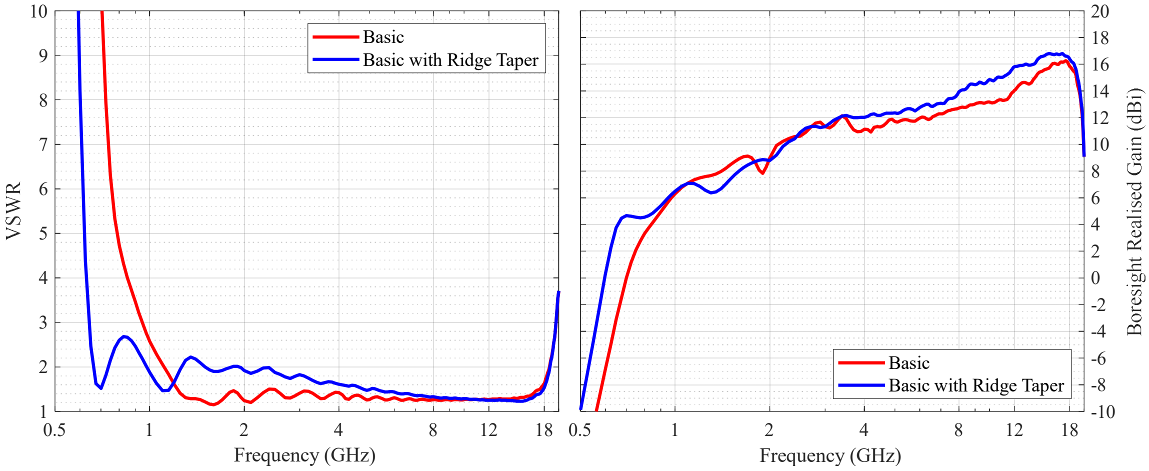

(a) (b)

Figure 3.15. (a) VSWR and (b) boresight gain comparison for the addition of the ridge taper to the basic initial model.

For the next tests, several ridge profiles were considered using the model from Figure 3.14(a) with a Bezier ridge profile as a starting point. Two other profiles were tested: an elliptical and an exponential one. Both are defined as physical not impedance profiles, see Figure 3.16.

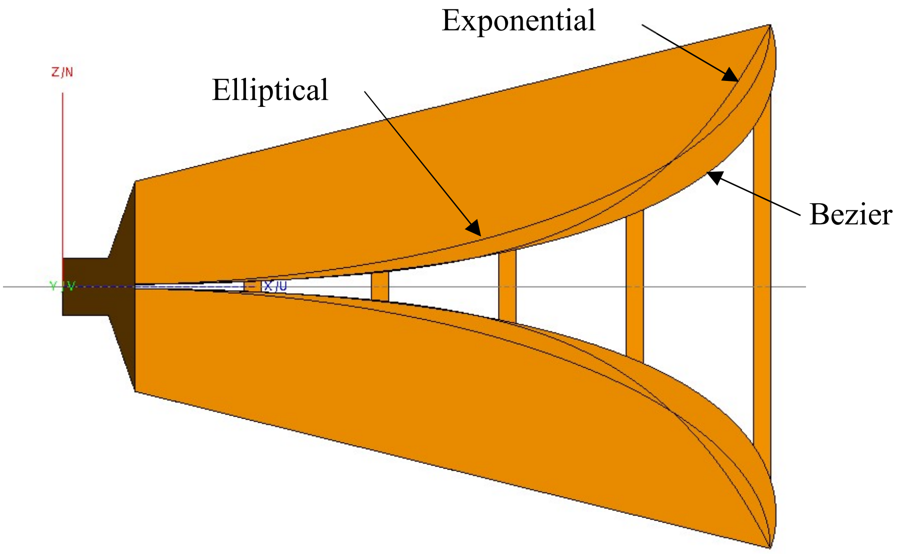

Figure 3.16. Comparison Bezier, elliptical and exponential ridge profiles.

The exponential profile opens slowly at the beginning, similar to the Bezier curve, and then it increases very quickly unlike the Bezier curve that was optimised for better aperture matching similar to [8].

The elliptical profile opens faster at the start, but near the aperture, the elliptical profile lies between the exponential and Bezier curves. The results of these tests are shown in Figure 3.17(a) and Figure 3.17(b). Above 8 GHz the VSWR and gain for all three profiles are similar except for a dip in gain for the exponential profile between 8 and 14 GHz. The elliptical ridge has slightly more gain and lower VSWR between 2 and 4 GHz, but the VSWR and gain degrades quickly below 1.2 GHz. The VSWR peaks of the exponential profile increase between 1 and 2 GHz. The Bezier curve has the best VSWR performance below 2 GHz, probably because it was optimised for better aperture matching in [14] which would be more apparent at low frequencies.

Overall, at least for this specific design, it looks like the Bezier curve provides superior performance. It does not look like the ridge profile impacts the bandwidth significantly, the reduction in bandwidth for the elliptical profile can most probably be corrected by doing a parametric study and finding the optimum values defining the elliptical curve.

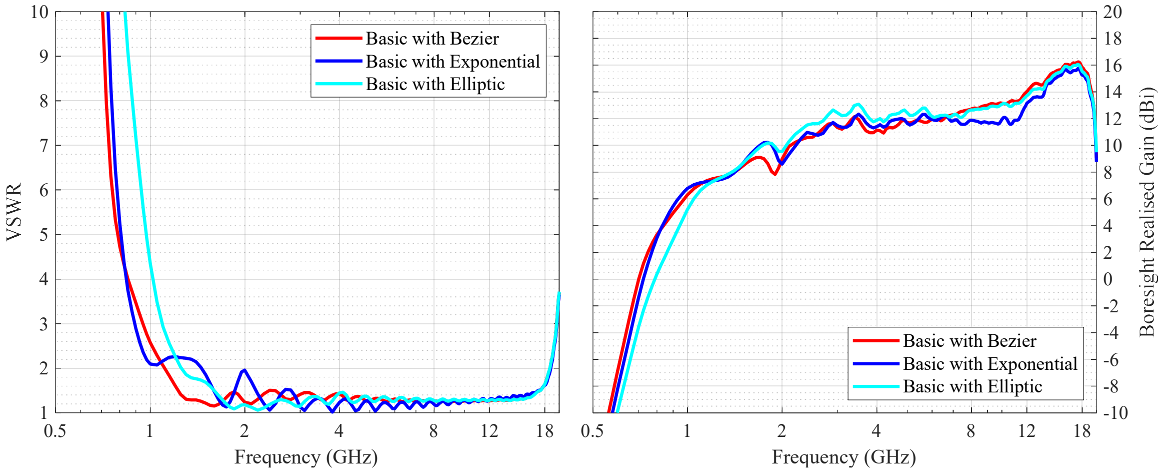

(a) (b)

Figure 3.17. (a) VSWR and (b) boresight gain comparison for several ridge profiles.

As a final test, a parametric study was performed on the ridge width and ridge gap using the model shown in Figure 3.12(b) as basis. The ridge gap and width were first varied in isolation and then the gap and width were varied together. The parameter values were reduced by 10% and increased by 10%, for example, the ridge gap was simulated for the values of 0.9 mm, 1 mm and 1.1 mm. From the results of these tests (Figure 3.18(a) and Figure 3.18(b)) the following was observed:

- By varying these parameters over such a limited range there is nearly no effect on the VSWR below 8 GHz and gain below 16 GHz.
- The best performance was found by either reducing just the ridge gap or reducing both the gap and the width.
- None of the changes led to an improvement in bandwidth. Thus, just slightly tuning the ridge parameters is not a useful method to improve bandwidth in DRGH antennas. It is still possible that a significant change in the ridge width and gap can result in bandwidth changes.

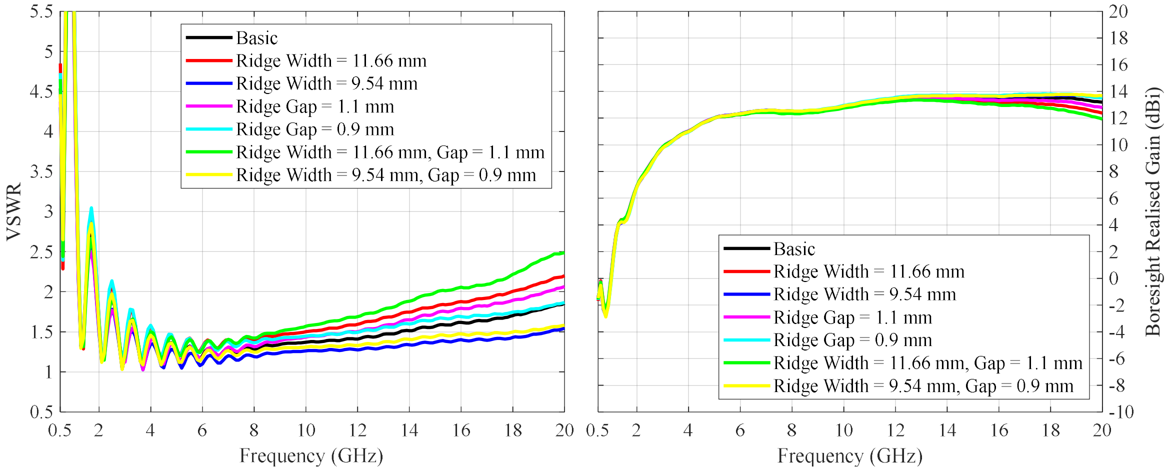

(a) (b)

Figure 3.18. (a) VSWR and (b) boresight gain comparison for the ridge width and gap parametric study.

In summary, the only ridge design parameter that seems to be useful to expand the bandwidth of the 1-18 GHz DRGH design is to vary the ridge width over the horn axial length. The other parameters such as the ridge profile, gap and width (for constant width ridges) are more useful in tuning the absolute performance.

3.3.5 Summary

In summary, considering the results of the investigation in this section, redesigning the coax-to-waveguide launcher and ridge width over axial length looks like the most promising method to increase the DRGH bandwidth. The coaxial line design does not look like a bandwidth limiting factor if the correct connector is used. The sidewalls are important to maintain the current bandwidth. It, however, does not look possible to further extend the bandwidth by changing the sidewall design.

3.4 ELECTRICAL DESIGN AND SIMULATIONS

In this section, the knowledge gained from the previous section is used to design the 0.5-18 GHz DRGH. Extensive use was made of experimentation using the EM models from the previous section as shown in Section 3.4.1. The final models and simulation results are presented in Section 3.4.2.

3.4.1 EM Experimental Design

As a starting point, the tapered ridge model of Section 3.3.4, Figure 3.12(c) was inserted into the original sidewall design, except that the *E*-plane grid sidewall was modified by reducing the strip width to 1 mm and increasing the strip gap to 60 mm as discussed in Section 3.3.2. This model thus did not include a coax-to-waveguide launcher cavity, see Figure 3.19(a). For the next design step, a pyramidal cavity (dimensions 80 × 55 mm for the base, height 19 mm) with a sharp end, ending at the same position as the original 1-18 GHz DRGH back short was added, see Figure 3.19(b). The ridges were stepped down and extended into the cavity for design step 3. The 15 mm gap of the ridge extensions was left unmodified from the 1-18 GHz DRGH design, see Figure 3.19(c). The forward half of the *E*-plane sidewalls of the pyramidal cavity was removed for step 4, see Figure 3.19(d) and Figure 3.21(a). The removed portion of the *E*-plane sidewall of the pyramidal cavity was increased to three-quarters of the pyramid height for step 5, see Figure 3.21(b). The simulated results for design steps 1 to 5 can be seen in Figure 3.20(a) and Figure 3.20(b) and are discussed below in a numbered list corresponding to the applicable design step:

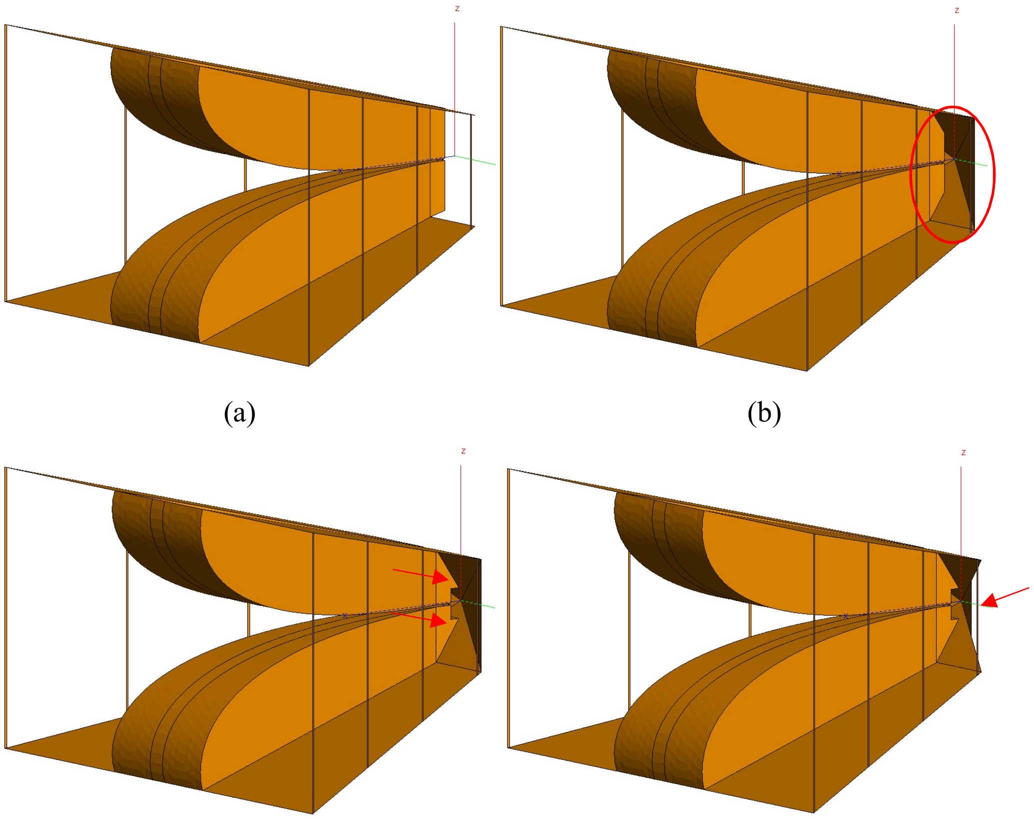

(a) (b)

(c) (d)

Figure 3.19. (a) Model for 0.5-18 GHz DRGH design step 1, (b) step 2, (c) step 3 and (d) step 4.

1. The basic design without cavity nominally works from 0.6 GHz.
2. The addition of the pyramidal cavity degrades the VSWR between 1.5 and 4 GHz, but the VSWR is still mostly below 2:1 above 0.6 GHz. Unfortunately, two very large gain peaks appear at 12 and 18 GHz indicative of pattern breakup.

3. The high-frequency gain is corrected, becoming nominally flat by adding the ridges inside the pyramidal cavity. This improvement comes at the expense of degraded VSWR below 1 GHz.
4. The degraded VSWR of Step 3 was slightly improved by removing part of the cavity *E*-plane flare without any effect on the boresight gain.
5. Further improvement was achieved by removing more of the sidewall, again without any effect on the boresight gain.

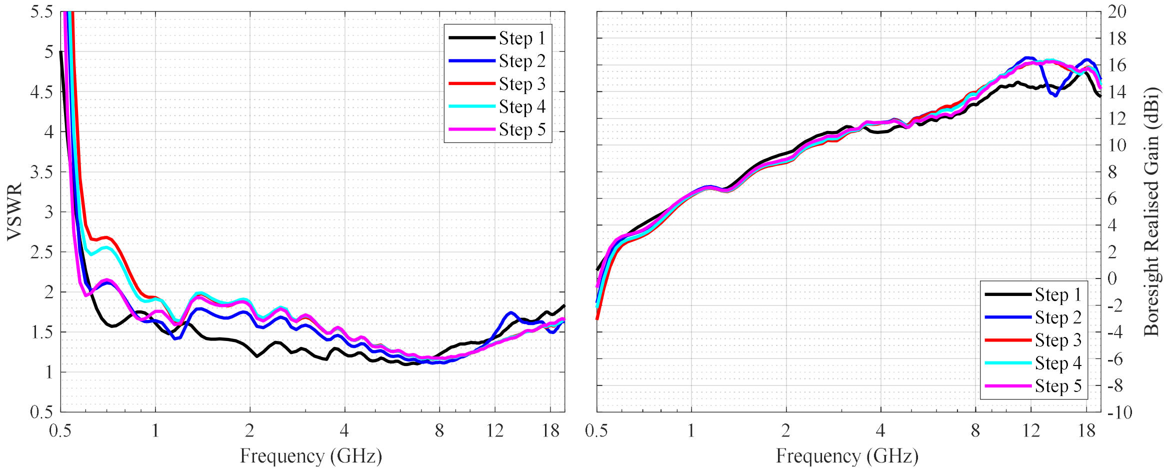

(a) (b)

Figure 3.20. (a) VSWR and (b) boresight gain comparison for design steps 1 to 5.

For step 6 the antenna was scaled by a factor of 1.1 except for the coax inner and outer conductors, strip width and strip gap which was left unmodified from the unscaled model. For step 7 the ridge gap around the feed point was reduced from 1.1 mm to 0.7 mm, see Figure 3.21(c). The feed point structure was then tapered from the coaxial line cylindrical to the start of the ridge in step 8 as shown in Figure 3.21(d).

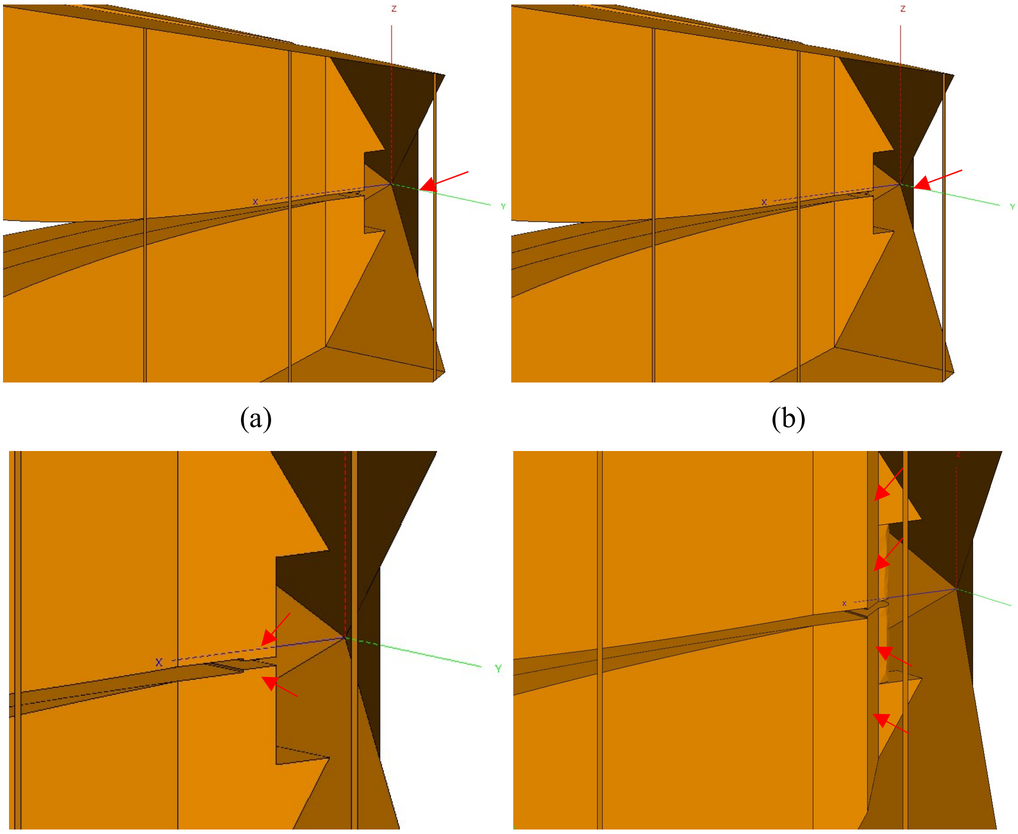

(a) (b) (c) (d)

Figure 3.21. (a) Model for 0.5-18 GHz DRGH design step 4, (b) step 5, (c) step 7 and (d) step 8.

The simulated results for design steps 5 to 8 can be seen in Figure 3.22(a) and Figure 3.22(b) and are discussed below in a numbered list corresponding to the applicable design step:

6. Scaling of the design moved the low-frequency VSWR run-out and gain drop lower in frequency with a maximum VSWR just below 3:1 at 0.5 GHz, but there is now a slight gain drop at 18 GHz.
7. The addition of the ridge step at the feed point degraded the VSWR above 6 GHz but improved the gain drop at 18 GHz.
8. Improvement of the coaxial feeding structure transition to the ridge significantly improved the VSWR and slightly improved the gain at 18 GHz. At this point, it seemed very promising that the performance of this design would be able to meet the requirements as stated in Section 3.1.

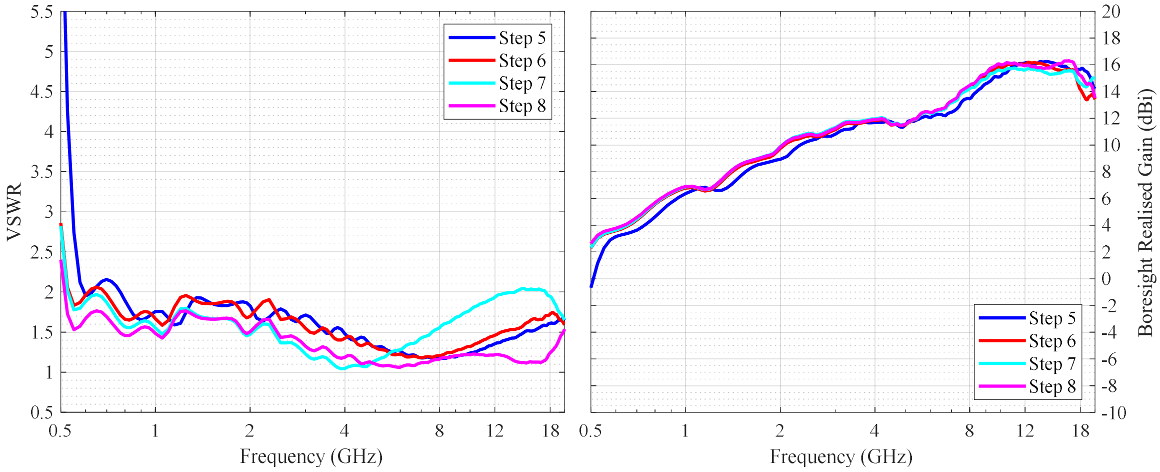

(a) (b)

Figure 3.22. (a) VSWR and (b) boresight gain comparison for design steps 5 to 8.

In summary by following an experimental approach, using EM simulation and step by step implementing and evaluating changes to the ridges and coaxial to waveguide launcher structure it was possible to design an extended bandwidth DRGH. Note that in Section 3.3 specifically the ridges and coax-to-waveguide launcher were identified as the main parts and or sub-assemblies of the DRGH design limiting the bandwidth.

3.4.2 Final Simulation Model and Results

The design from step 8 in the previous section was subsequently optimised by slightly adjusting some of the parameters of the ridges and coax-to-waveguide launcher while staying with the basic structure from step 8. This model still had one drawback in that it used the basic short 32 Ω coaxial feed and some kind of impedance transformation would be required between the 50 Ω RF connector and the ridge feed point. The characteristic impedance of the ridges at the feed point for the final simulation design was calculated as 31 Ω using the Matlab script (see Section 2.5.1 and Section 3.5) implementation of the transverse resonance method. It was thus decided to add a coaxial impedance transformer to the FEKO model, see Section 3.5.1 for the details of this design.

The final basic FEKO model with a coaxial impedance transformer is shown in Figure 3.23(a). A highly detailed model was then created to improve accuracy and reduce risk before performing the mechanical design and manufacturing a prototype, see Figure 3.23(b). This model included material thicknesses, the PCB *E*-plane sidewalls and a model for a SMA connector. As with the detailed 1-18 GHz DRGH FEKO model, the SEP was used to model the dielectric materials. The general triangle edge length for the detailed model was reduced from λ/3 to λ/5 at 18 GHz. The basic model consisted of 7190 PEC triangles while the detailed model consisted of 25870 PEC triangles and 6577 dielectric triangles.

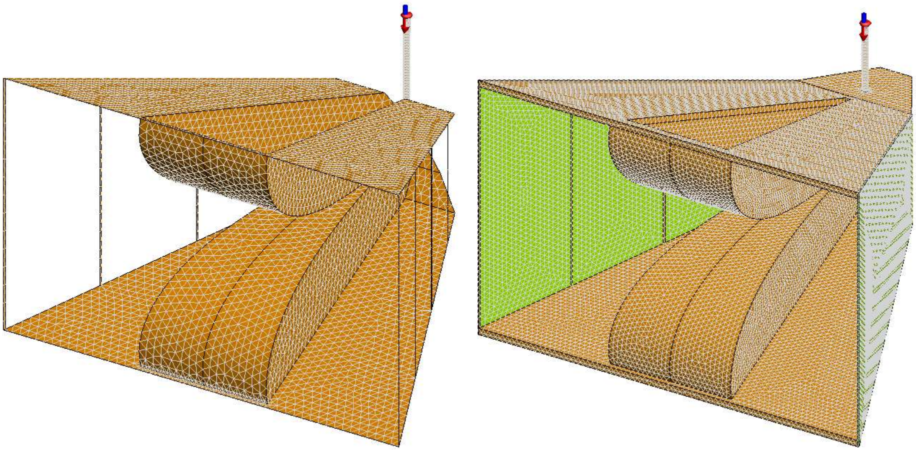

(a) (b)

Figure 3.23. (a) Final optimised basic and (b) detailed FEKO model.

The final simulation results, shown in Figure 3.24(a) and Figure 3.24(b), were calculated at 201 frequency points between 0.5 and 18 GHz with a frequency step size of 25 MHz below 1 GHz, 50 MHz between 1 and 2 GHz and 100 MHz above 2 GHz. For comparison purposes when performing simulations using twelve parallel cores on one Central Processing Unit (CPU), the basic model per core peak memory requirement was 153–170 MB (total peak of 1.8 GB) and the per core runtime 4.7 hours (total of 56.4 hours). For the detailed model, the per-core peak memory requirement was 4.4–4.5 GB (total peak of 52.5 GB) and the per-core runtime was 201 hours (total of 2411 hours). The detailed model predicted slightly reduced boresight gain performance above 16 GHz and slightly better performance between 5 and 8 GHz. The VSWR is virtually identical for both models. Evaluation of the simulated 3D radiation patterns confirmed no pattern breakup at the high-frequency end, see for example Figure 3.25. In simulation, this final electrical design easily meets the requirements as set out in Section 3.1. The final dimensions for this design will be presented in Section 3.5.

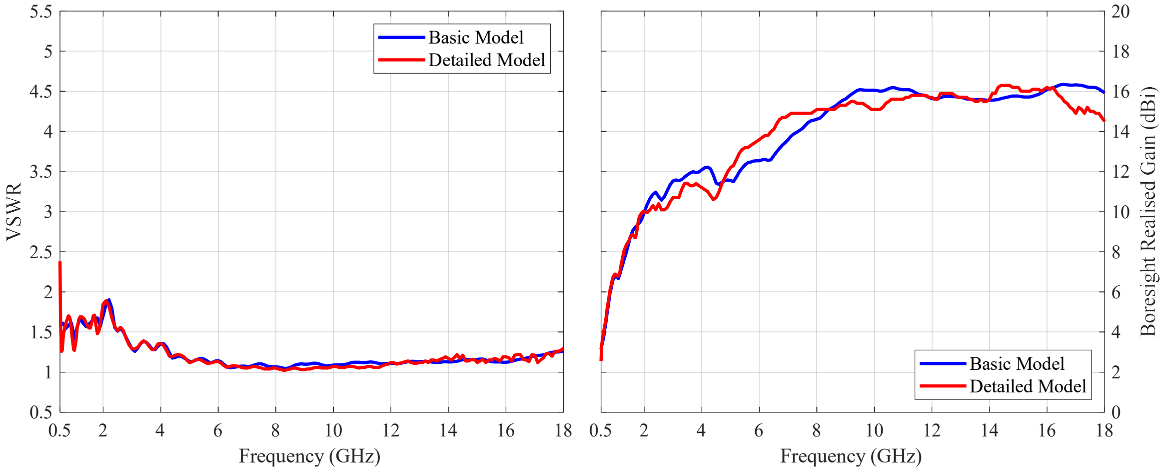

(a) (b)

Figure 3.24. (a) Final simulated VSWR and (b) boresight gain comparison for the basic and detailed FEKO models.

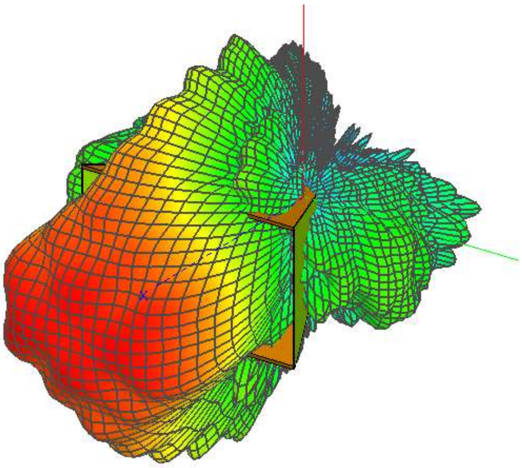

Figure 3.25. Radiation pattern (3D) at 18 GHz for the detailed model.

3.5 PROTOTYPE DESIGN AND MANUFACTURE

The detailed FEKO model from Section 3.4.2 was used as a starting point to perform a mechanical design and create CAD models and detailed drawings from which a prototype was manufactured, see Figure 3.26(b). The final design and dimensions will be discussed in detail in the following sections. Most of the manufactured parts were machined in aluminium except for the PCB sidewalls, which were etched on FR4, and feed pin. The feed pin was machined in brass with subsequent gold plating.

To reduce the possibility of gaps between parts and sub-assemblies which could lead to performance deviations, see [16], [17], the minimum number of sub-assemblies was implemented. As an example, the coax-to-waveguide launcher was implemented as a single part using a 5-axis CNC machine. Note that the 0.5-18 GHz DRGH prototype has a weight of 1.78 kg which is 40 grams more than that of the 1-18 DRGH. This was made possible due to the reduced mass of the PCB sidewalls compared to the thick grid sidewalls and the mass reduction applied to the tapered ridges which would otherwise be very heavy.

(a) (b)

Figure 3.26. (a) The 1-18 GHz DRGH from [14] and (b) prototype 0.5-18 GHz DRGH.

3.5.1 Coaxial Feed Design

For ease of assembly and testing it was decided to use an SMA connector (Huber & Suhner 23SMA-50-0-165). If higher power handling is required this connector can be replaced without any additional modification by an N-type connector (Southwest Microwave 312-14SF) with the same flange dimensions. As mentioned in Section 3.4.2 a coaxial impedance transformer was implemented in the coaxial feed line to transform the impedance from 50 Ω at the RF connector to 31 Ω, see Section 3.5.4, at the ridge feed point shown in Figure 3.27. Like the design presented in [14] the outer conductor was implemented as a constant diameter (3.7 mm) hole through the upper ridge. The part of the coaxial line inside the ridge is quite short (nominally 30 mm) and ideally, the impedance transformer transition length should be λ/2 at the lowest frequency of operation, which is 300 mm. This would, however, not be practical. It was thus decided to restrict the transition length to 75 mm (λ/2 at 2 GHz) in total which would avoid extension beyond the horn aperture. To add the additional transition length, a new part, basically a hollow tube with mounting flanges was added on top of the coax-to-waveguide launcher. The RF connector was mounted on top of this new part.

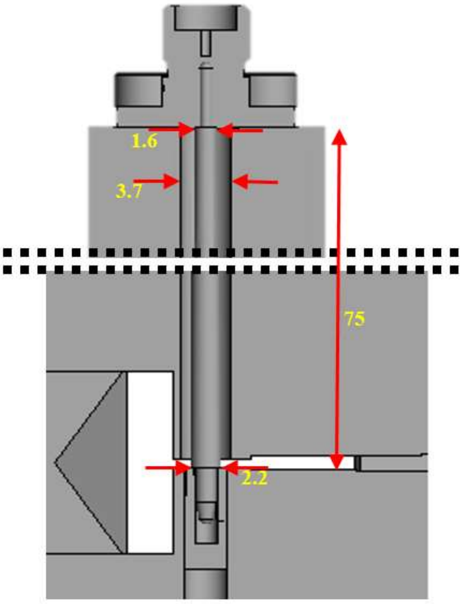

Figure 3.27. Coaxial feed impedance transformer design, dimensions in mm.

The feed pin, forming the centre conductor, has a 0.9 mm tab to interface with the spring fingers of the RF connector. For ease of manufacture, the diameter of the feed pin increases linearly from 1.6 mm at the RF connector (50 Ω) to 2.2 mm at the feed point on the bottom ridge (31 Ω). It is possible that the low-frequency VSWR performance could potentially be improved by increasing the transition length or implementing for example a Hecken taper instead of a linear taper on the feed pin. The bottom of the feed pin has another tab to fit into a collet with spring fingers extracted from an N-Type connector. The collet is press fitted into a hole machined in the bottom ridge, similar to [14], [17], see Figure 3.27. The collet was pressed into the bottom ridge until the top of the collet was flush with the ridge face at the feed point. Once the pin was securely inserted into the collect, silver epoxy was applied to the feed point to fill all the voids and ensure good electrical contact.

During manufacturing, it was found that the high-frequency gain and VSWR performance of the DRGH antenna are extremely sensitive to small variations of the feed point and the exact location of the spring fingers. Small changes resulted in large variations in performance, especially if silver epoxy is not applied to remove any gaps. Simulations performed on a model without the impedance transformer confirmed the significant improvement in VSWR across the band when adding the transformer, for a comparison of these results see Figure 3.28.

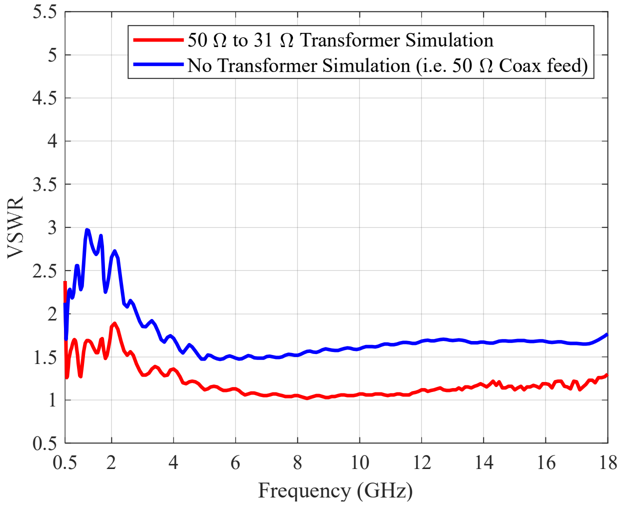

Figure 3.28. Impact of the coaxial impedance transformer on VSWR.

3.5.2 Flared Waveguide and Sidewall Design

The flared waveguide and sidewall design is shown in Figure 3.29. The solid *H*-plane sides were machined in aluminium, and a triangular section corresponding to the hollowed-out ridge (see section 3.5.4) was cut in the *H*-plane sides to reduce mass. The two *E*-plane sides were implemented as etched grids on a 0.8 mm FR4 PCB. The strip width and spacing were kept the same as designed in Section 3.4.21 i.e. a 1 mm strip width and a gap of 60 mm (λ/10 at 0.5 GHz). The *H*-plane sidewalls are mounted with screws to the ridges and in turn the *E*-plane sidewalls are mounted with screws to the *H*-plane sidewalls, see Figure 3.26.

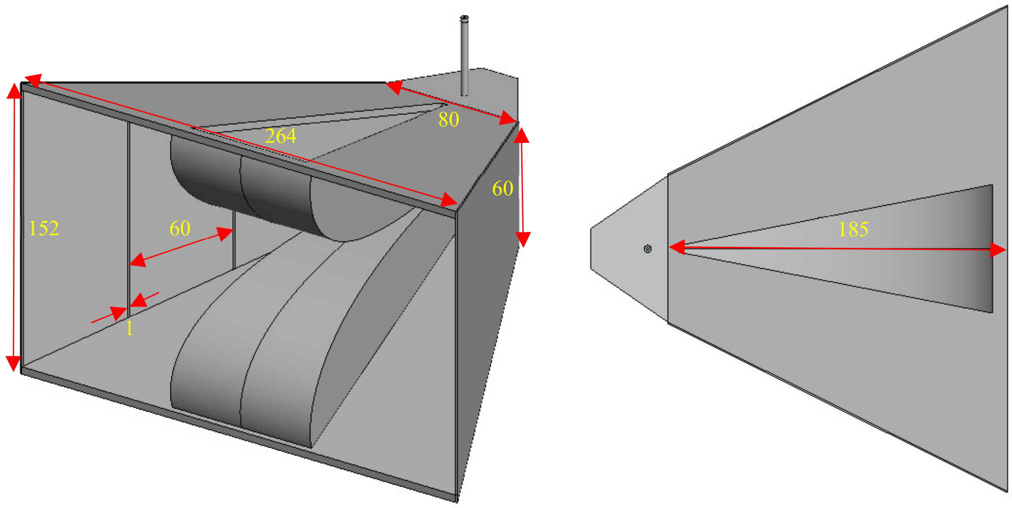

Figure 3.29. Flared waveguide and sidewall design, dimensions in mm.

The dimensions of the pyramidal flared waveguide are nominally 10% more than that of the 1-18 GHz DRGH as per the design in Section 3.4.1. Note that the final scaling is not exact due to further tuning and the impact of several practical factors when the mechanical design was performed. The *H*-plane aperture width was increased from 242 to 264 mm and the *E*-plane aperture from 136 to 152 mm. The flared waveguide axial length from the launcher aperture to the horn aperture was increased from 168.8 to 185 mm. The coax-to-waveguide interface discussed in the next section on the other hand has a slightly reduced cross-section compared to the 1-18 GHz DRGH. At the interface between the coax-to-waveguide launcher and the flared waveguide the waveguide width (*H*-plane) was reduced from 86 to 80 mm and the height (*E*-plane) from 66 to 60 mm.

3.5.3 Coax-to-Waveguide Launcher Design

The evolution of the coax-to-waveguide launcher design from a basic pyramidal cavity to the final geometry discussed in this section is presented in Section 3.4.1. The optimised dimensions used for the final simulations of Section 3.4.2 are shown in Figure 3.30.

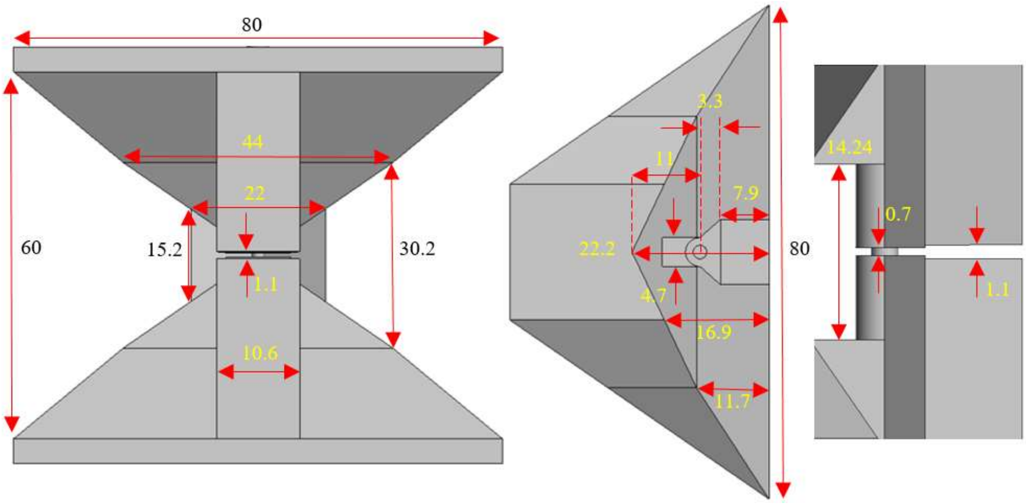

Figure 3.30. Coax-to-waveguide launcher design.

The mechanical implementation compared to the 1-18 GHz DRGH is shown in Figure 3.31. As mentioned before, the coax-to-waveguide launcher only consists of a single part, and due to the complexity of this part, was machined on a 5-axis CNC milling machine in aluminium. Except for the sidewalls, all the other parts and sub-assemblies of the DRGH, notably the coaxial feed and ridges are mounted with fasteners to the coax-to-waveguide launcher. Note that in both figures the portion of the ridges extending into the launcher is also shown for clarity. The ridges fit into gaps, shown in Figure 3.31(c), in the launcher. Figure 3.31(b) shows how the coaxial feed including the pin and RF connector is mounted to the launcher. The block at the rear of the waveguide launcher in Figure 3.31 (b) does not have an electrical function and is only used for mounting purposes, for example in an anechoic chamber or on a test stand or tripod. The final configuration can be described as a three-step pyramidal cavity with partially open *E*-plane sidewalls.

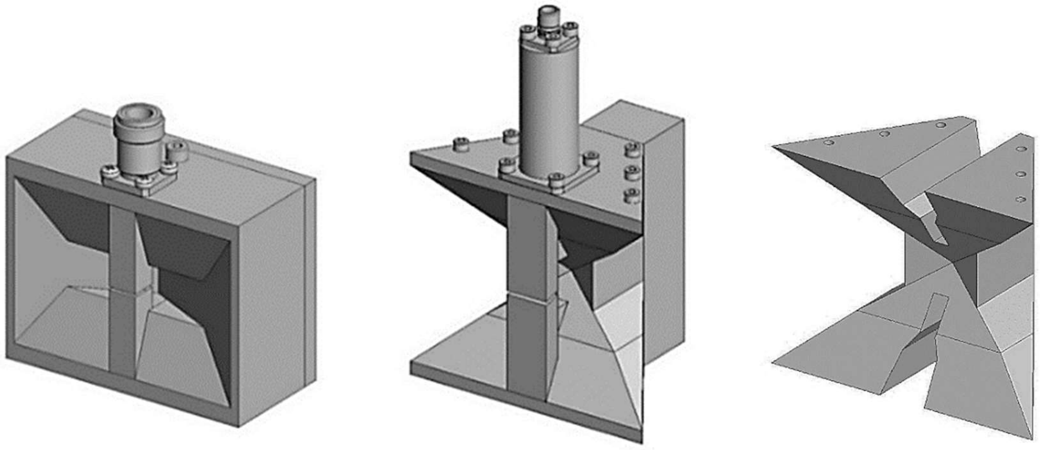

(a) (b) (c)

Figure 3.31. (a) Existing 1–18 GHz DRGH waveguide launcher, (b) new 0.5–18 GHz DRGH launcher and (c) new 0.5–18 GHz DRGH launcher with ridges removed.

3.5.4 Ridge Design

As shown in Section 3.4 the final ridge design does not have a constant width like the 1-18 GHz DRGH design from [14], but rather has a tapered width similar to [24], [25], increasing linearly from 10.6 mm at the coax-to-waveguide launcher aperture to 84.4 mm at the flared waveguide aperture. The ridges were machined in aluminium which along with the tapered width would result in very heavy parts, therefore, to reduce mass the ridges were hollowed out. The only drawback to this is an increase in cost due to longer machining times.

As mentioned before the ridge profile followed a cubic Bezier curve similar to [14], see Figure 3.32 for a comparison between the ridge profiles of [14] and this section. Lines are also drawn in this figure to show the Bezier control points. The profiles in this figure are aligned at the feed point. A parametric study was performed to find the control points that provided the best aperture-matching performance, see Table 3.1 for the final values. Note that in this table the axial distance (*x*) along the horn axis is measured from the feed point (*x*=0) inside the coax-to-waveguide launcher.

The dimensions of the ridge at the coax-to-waveguide launcher interface and the detail of the portion extending into the coax-to-waveguide launcher was shown in Figure 3.30. Using these dimensions (also shown in Figure 3.43) and the transverse resonance method $Z_{0\infty}$ was calculated at the coax-to-waveguide interface as $Z_{0\infty}$ =31 Ω. This value was used for the coaxial feed design, see Sections 3.4.2 and 3.5.1.

Table 3.1. Cubic Bezier control points of the final ridge profile (in mm).

Bezier point	**Description**	**Axial distance (x)**	**Perpendicular distance (z)**
P0	Start point	3.3	0.55
P1	Start tangent point	236.32	0.55
P3	End tangent point	203.99	75.99
P4	End point	204	76

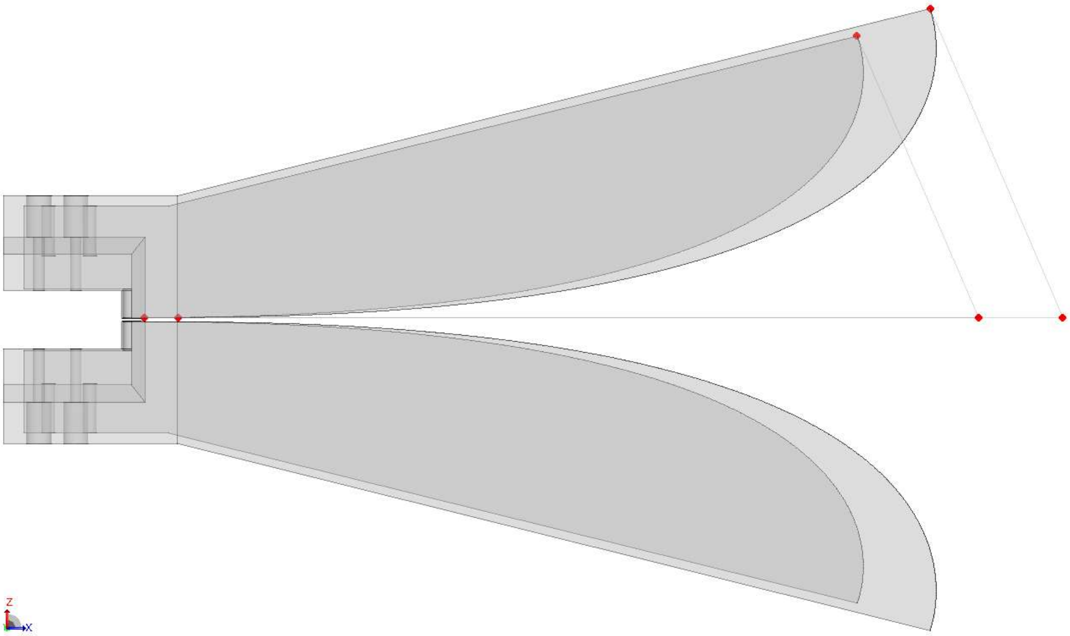

Figure 3.32. Ridge profile comparison 1-18 GHz (smaller) vs 0.5-18 GHz DRGH (larger).

As discussed in Section 3.4.1 and shown in Figure 3.21 and Figure 3.30 the ridge gap at the feed point is stepped down from 1.1 to 0.7 mm. The portion of the ridges stepped down and extended towards the rear of the antenna into the cavity of the coax-to-waveguide launcher, as discussed in Section 3.4.1 and shown in Figure 3.19, has a gap of 14.24 and a width of 4.7, see Figure 3.30. This extension mounts into gaps in the coax-to-waveguide launcher (see Figure 3.31(c)) and is extended far enough so that fasteners can be used to mount the ridges to the launcher as shown in Figure 3.32.

3.6 MEASURED RESULTS

The VSWR of the prototype antenna was measured at 401 points from 0.5-18 GHz using a VNA while gain and pattern measurements were performed in a tapered anechoic chamber, also using a VNA, see Figure 3.33. To cover the full 0.5-18 GHz band two different setups were used in the chamber. For the low band gain measurements were performed in 10 MHz steps from 0.5-2 GHz and for the high band the step size was 25 MHz from 2-18 GHz. The pattern measurement frequency step size was 50 MHz and 100 MHz for the low and high band setups respectively. All the radiation patterns were measured from 0° to 360° with 2° increments. The radiation patterns were measured for both co- and cross-polarisation in three cut planes, the *E*-, *H*-, and *+45*°-planes. The plots for several discrete frequencies are presented in Figure 3.34 and Figure 3.35, to prove that this antenna does not have pattern breakup at the high-frequency end of the band.

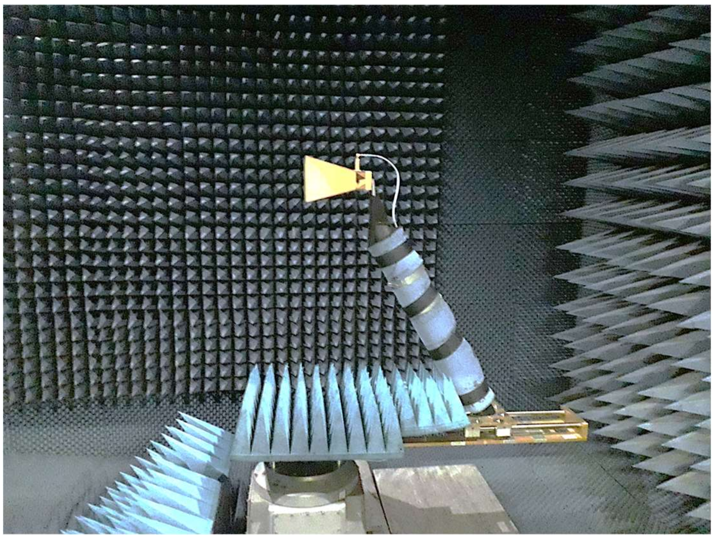

Figure 3.33. Tapered anechoic chamber measurement setup.

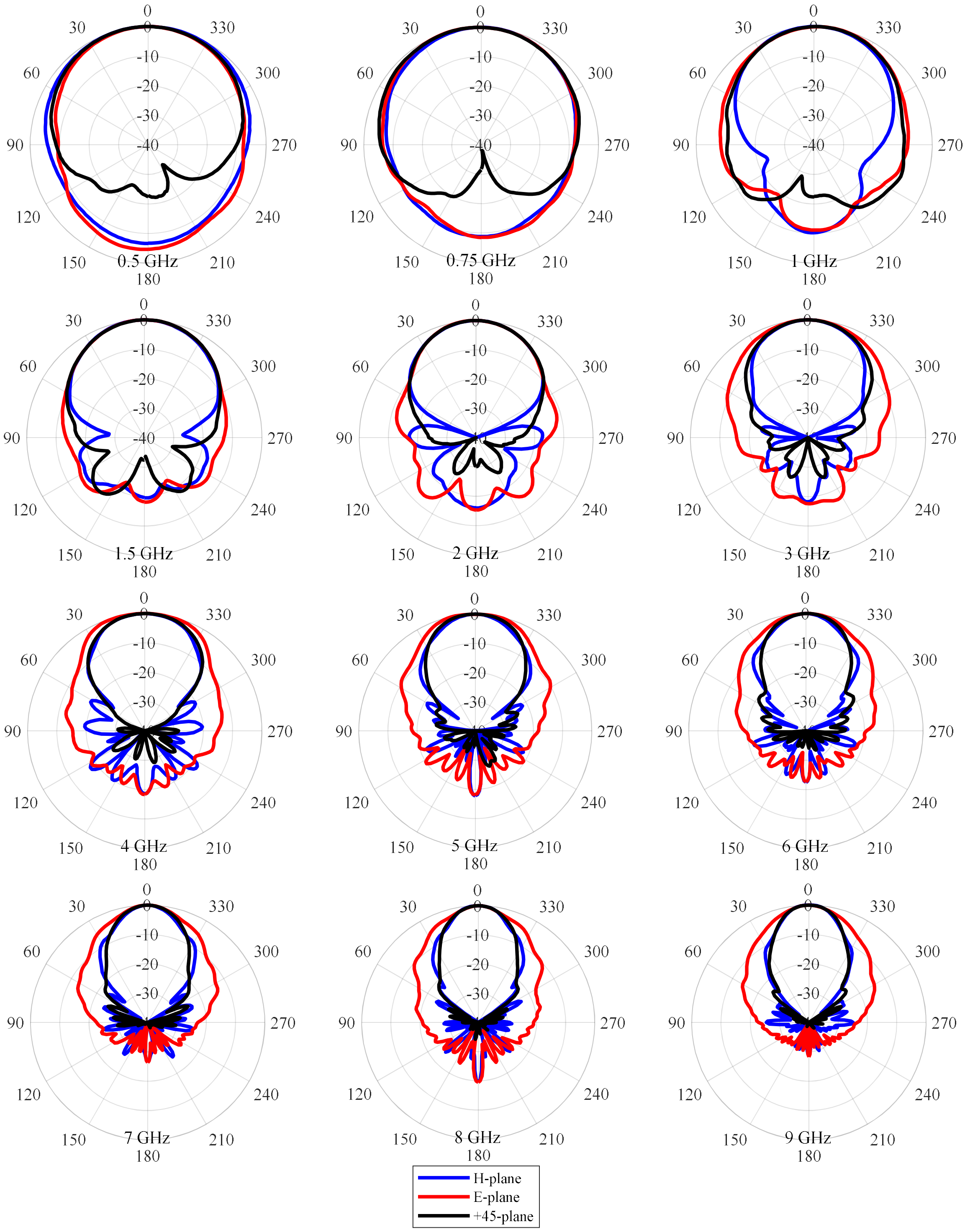

Figure 3.34. Measured co-polarised radiation patterns from 0.5 to 9 GHz of the 0.5–18 GHz DRGH.

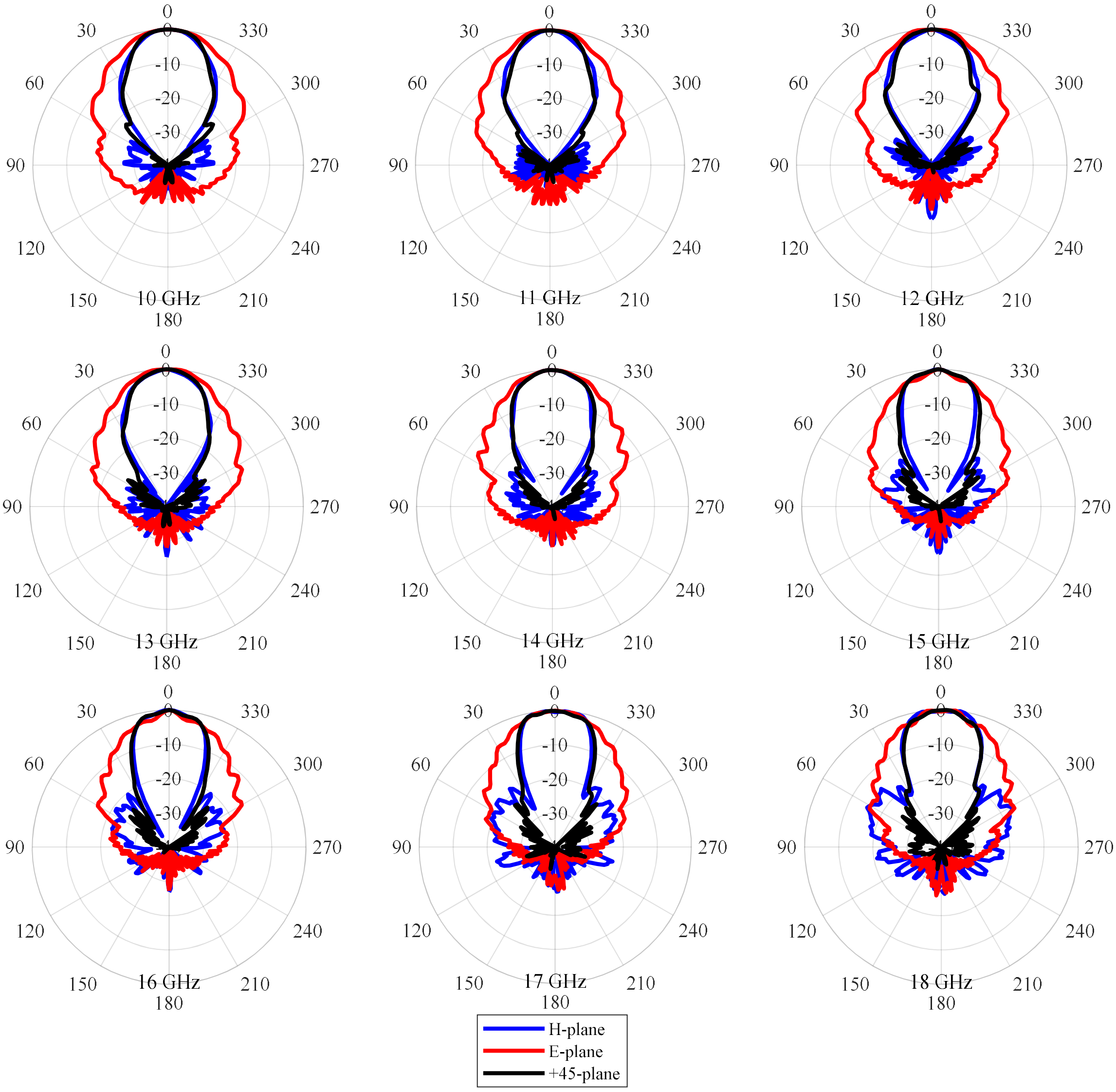

Figure 3.35. Measured co-polarised radiation patterns from 10 to 18 GHz of the 0.5–18 GHz DRGH.

3.6.1 Comparison to Simulated Results

The measured results are compared to the detailed EM model's simulated results in Figure 3.36(a) and Figure 3.36(b). The agreement between measured and simulated results is very good. The VSWR ripple above 12 GHz is due to manufacturing tolerances and a very sensitive feed region. The VSWR is below 2:1 over the whole band and below 1.5:1 above 3 GHz. The measured and simulated gain results are typically within the measurement accuracy of ±0.5 dB. The minimum gain at 0.5 GHz is approximately 4 dBi and increases to approximately 16 dBi at 16 GHz. The small differences in measured and simulated realised gain can be attributed to the difference in simulated and measured VSWR, manufacturing and measurement tolerances.

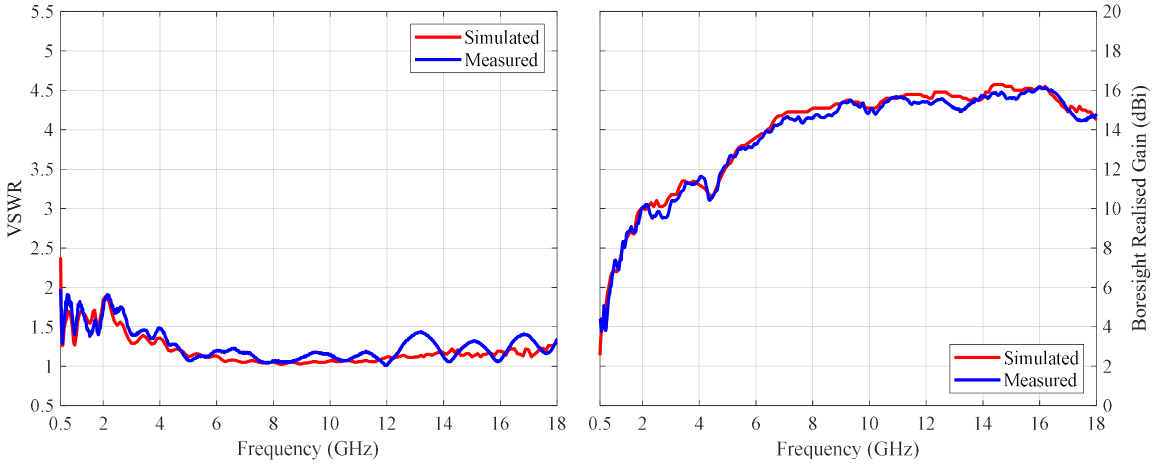

(a) (b)

Figure 3.36. (a) VSWR and (b) boresight gain comparison of the final simulated and measured results for the 0.5-18 GHz DRGH.

The measured cross-polar discrimination, shown in Figure 3.37, is typically better than 30 dB with the worst-case value of 27.5 dB at 850 MHz. The simulated cross-polar discrimination is not shown in Figure 3.37 since it is typically better than 100 dB.

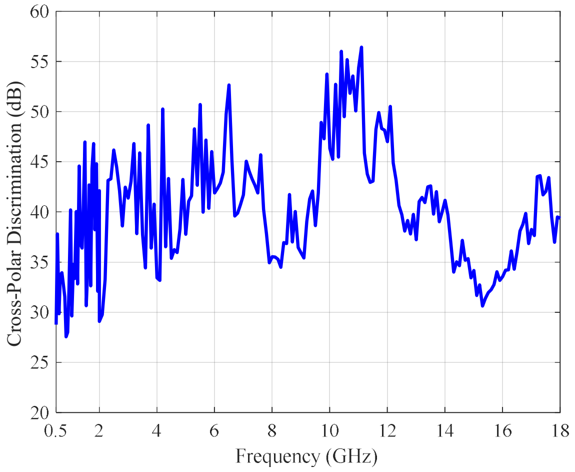

Figure 3.37. Measured boresight cross-polar discrimination for the 0.5-18 GHz DRGH.

The *E*- and *H*-plane 3dB beamwidth, side and back lobes extracted from the measured results are shown in Figure 3.38(a) and Figure 3.38(b), respectively, with excellent comparison between simulated and measured results. The *H*-plane beamwidth is slightly narrower than the *E*-plane, but both are very constant above 6 GHz, staying in a band between 20° and 40°. The side lobe level is typically well above 15 dB above 1 GHz and the back lobe level improves from 7 dB at 0.5 GHz to 20 dB at 18 GHz.

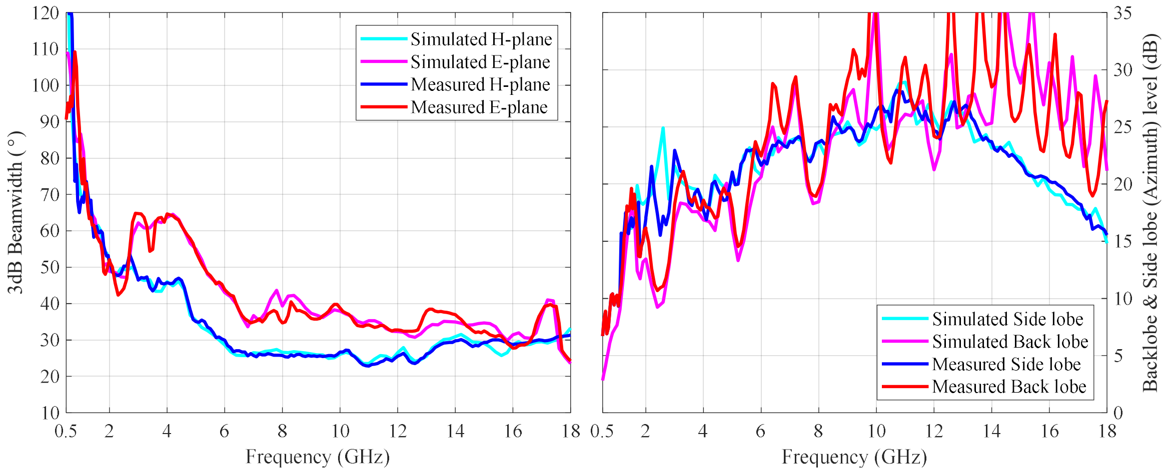

(a) (b)

Figure 3.38. (a) Beamwidth (3 dB), (b) back lobe and side lobe level comparison between simulated and measured results for the 0.5-18 GHz DRGH.

In the following sections, the measured result of the 0.5-18 GHz DRGH will be compared firstly to that of the 1-18 GHz DRGH used as bases for this design and then to other commercially available antennas.

3.6.2 Comparison to 1-18 GHz DRGH

This section provides a comparison between the measured results for the 1-18 GHz DRGH from [14] and the 0.5-18 GHz DRGH designed in this chapter. Both the VSWR and gain of the 0.5-18 GHz DRGH are similar or better than the 1-18 GHz DRGH in the 1-18 band, but the 0.5-18 GHz antenna works down to 500 MHz, see Figure 3.39(a) and Figure 3.39(b).

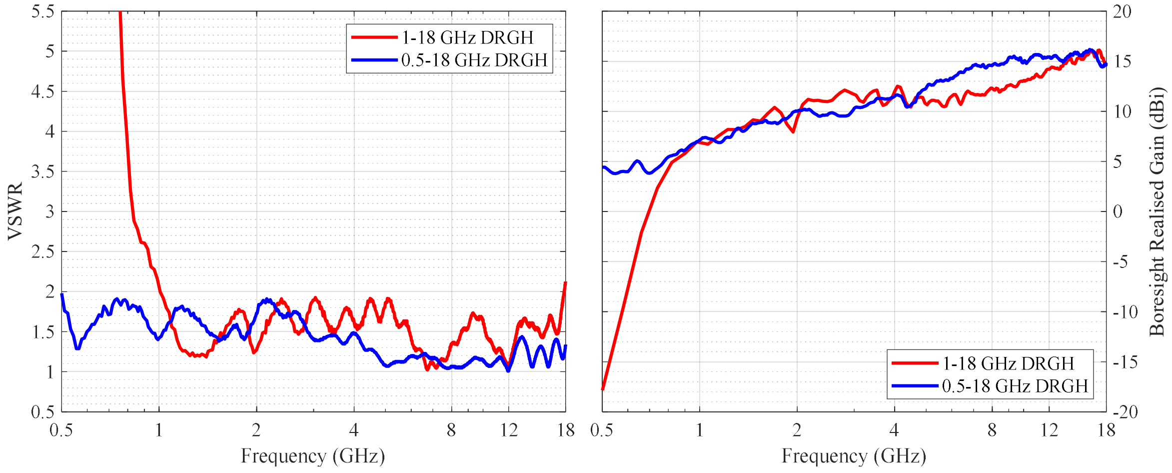

(a) (b)

Figure 3.39. (a) VSWR and (b) boresight gain comparison between measured results for the 1-18 GHz and 0.5-18 GHz DRGH.

The same result holds for the cross-polar discrimination (Figure 3.40), 3 dB beamwidth (Figure 3.41(a)), side and back lobe levels (Figure 3.41(b)), i.e. the performance of the 0.5-18 GHz DRGH is similar or better than the 1-18 GHz DRGH in the 1-18 GHz band, but the 0.5-18 GHz antenna works down to 500 MHz.

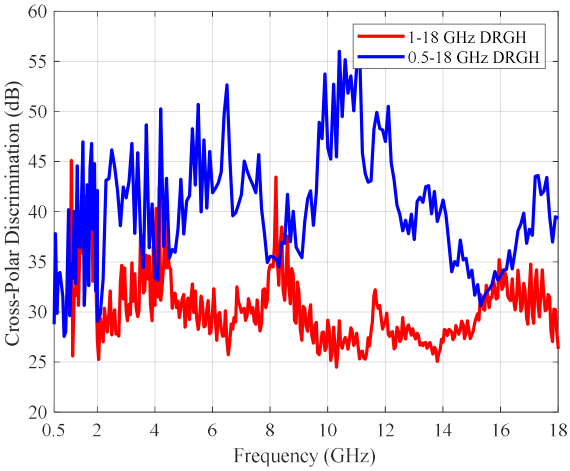

Figure 3.40. Comparison boresight cross-polar discrimination between measured results for the 1-18 GHz and 0.5-18 GHz DRGH.

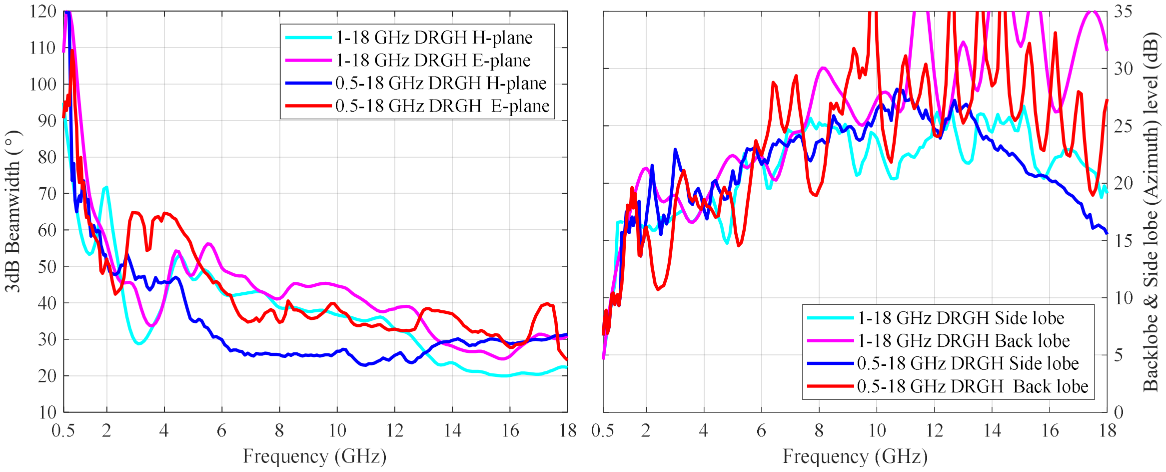

(a) (b)

Figure 3.41. (a) Beamwidth (3 dB), (b) back lobe and side lobe level comparison between measured results for the 1-18 GHz and 0.5-18 GHz DRGH.

In summary, the performance of both antennas is very similar in the overlapping band and thus the DRGH bandwidth was extended from 18:1 to 36:1 without any loss of performance.

3.6.3 Comparison to Commercially Available Antennas

Typical commercially available DRGH antennas operate either in the 0.5-3 GHz band (low) or in the 0.7-18 GHz band (high). Thus, in this section, the 0.5-18 GHz DRGH will be compared to several commercially available horn antennas that cover either the low or high band. Note that the low-band antennas were chosen based on having the smallest size (aperture and axial length) available, while still working down to 0.5 GHz.

The high-band antennas were chosen from the catalogues of some of the most reputable measurement antenna suppliers. Table 3.2 compares the aperture dimensions, axial length and mass of the six (three low- and three high-band) antennas chosen to compare to the 0.5–18 GHz DRGH antenna.

The low-band antennas are significantly larger with a corresponding increase in mass, while the high-band horns are comparable in size and mass to the 0.5-18 GHz DRGH. Figure 3.42(a) and Figure 3.42(b) compare the boresight gain of the 0.5–18 GHz antenna to the models listed in Table 3.2.

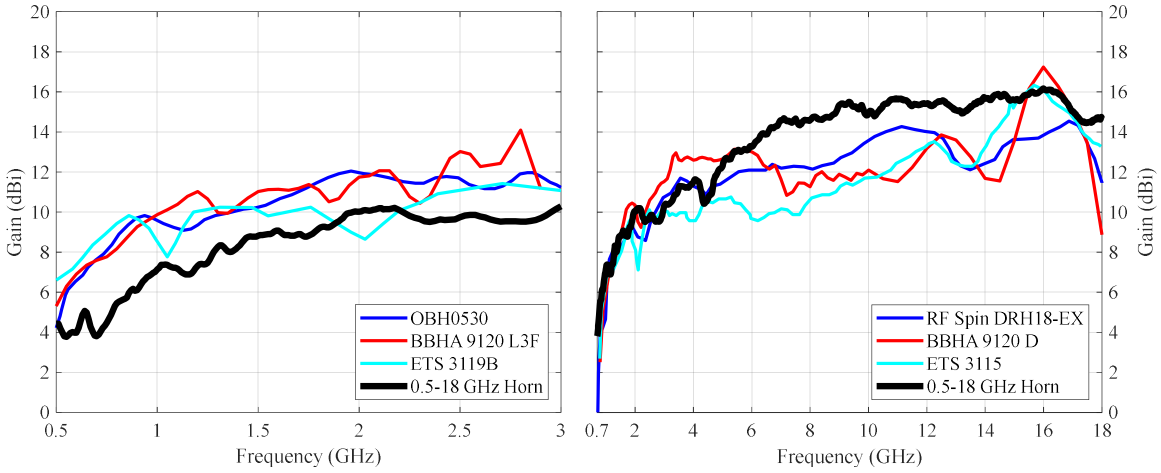

(a) (b)

Figure 3.42. (a) Low and (b) high band boresight gain comparison of the 0.5-18 GHz DRGH to several commercial DRGH antennas.

In the low-band, the 0.5–18 GHz antenna has around 2 dB less gain than the other antennas, which can be expected due to the significantly smaller size of the 0.5-18 GHz antenna. The gain of this antenna is still more than adequate for most applications in this band. Furthermore, it is also expected that if more gain is required, the antenna can be redesigned with a larger aperture and longer axial length to improve low-frequency gain. In the high band, the 0.5-18 GHz antenna has better gain over most of the band. The gain ripple of this antenna is also lower.

In summary, the 0.5–18 GHz DRGH antenna compares well in terms of size and performance to other commercial antennas that do not cover the full bandwidth and provides a very good size-to-performance trade-off with significantly better performance above 6 GHz and usable performance down to 0.5 GHz.

Table 3.2. Comparison to several commercial DRGH antennas.

Description	**Manufacturer**	**Aperture dimensions (mm)**	**Axial length (mm)**	**Mass (kg)**
Low Band 0.5-3 GHz				
OBH0530	Ocean Microwave	440 × 290	350	6.8
BBHA 9120 L3F	Schwarzbeck	416 × 243	342	3.8
ETS 3119B	ETS-Lindgren	488 × 314	400	5.2
High Band 0.7-18 GHz				
DRH18-EX	RF Spin	234 × 186	216	0.87
BBHA 9120 D	Schwarzbeck	245 × 142	195	1.3
ETS 3115	ETS-Lindgren	244 × 159	279	1.8
0.5–18 GHz Horn	Saab Grintek Defence	**264 × 152**	**185**	**1.78**

3.7 MODAL FIELD AND BANDWIDTH ANALYSIS

Using the Matlab script (see Section 2.5.1) implementing the transverse resonance method and the dimensions shown below in Figure 3.43 from Section 3.5 the cut-off frequency for the TE_{10} mode was found to be 421 MHz. With the feed pin/probe in the centre of the ridge, the next expected higher-order mode is TE_{30} [38]. In theory the TE_{20} mode is not excited, however, its cut-off frequency is 4.31 GHz, while the TE_{30} mode cut-off frequency is 4.36 GHz for a MUB, $\frac{\lambda_c^{10}}{\lambda_c^{30}}$, of 10.4:1. Yet through parametric studies in simulation ultimately a design with significantly more bandwidth; 36:1 was achievable. To further investigate this divergence in results a modal field and bandwidth analysis was performed using the transverse resonance method and the EM solvers FEKO and CST.

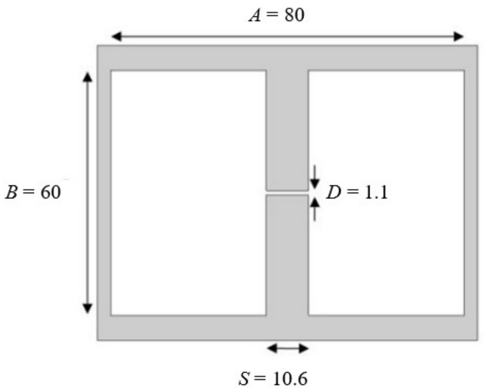

Figure 3.43. Double-ridged cross-section for transverse resonance calculations.

As in [38] using the transverse resonance method the TE_{10} and TE_{30} cut-off wavelengths, normalised by the dimension A, for $B/A = 0.75$ (60/80) and various values of S/A and D/B were calculated and can be seen in Figure 3.44. The resulting TE_{10}/TE_{30} bandwidth is shown in Figure 3.45. In Figure 3.44 the solid lines apply to TE_{10} and the dashed lines to TE_{30}. The values of D/B are indicated on the individual plotted lines. A red star marks the results using the values in Figure 3.43.

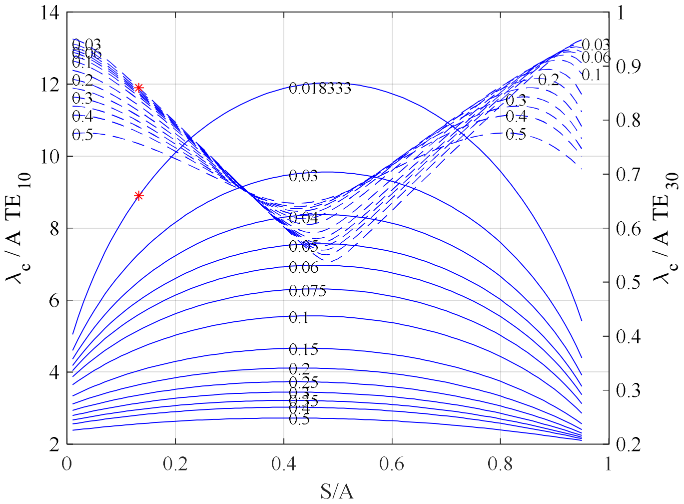

Figure 3.44. *TE_{10}* and *TE_{30}* mode cut-off wavelengths in double -ridged waveguide for various values of *S/A* (*x*-axis) and *D/B* (different lines) with *B/A* = 0.75.

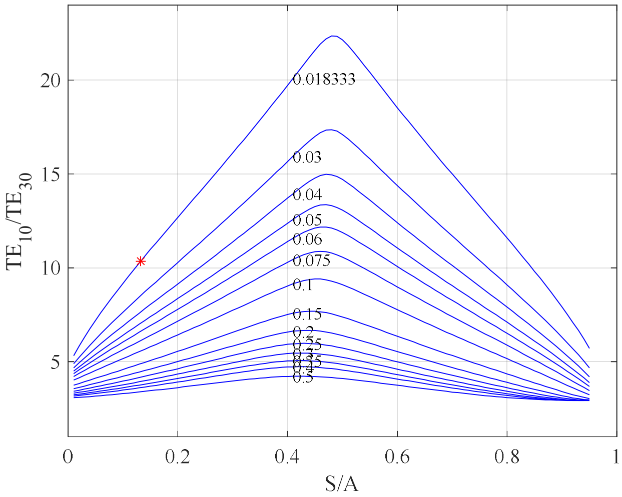

Figure 3.45. *TE_{10}/TE_{30}* bandwidth.

From these figures it is clear as stated in [38] that the MUB quickly increase with a decrease in *D/B* i.e. the smaller the ridge gap, the larger the bandwidth. Conventional wisdom would advocate the use of an *S/A* value between 0.4 and 0.5 for peak *TE_{10}/TE_{30}* bandwidth (nominally 22:1 in Figure 3.45) with a ridge gap as small as possible depending on the power handling requirement and ability to manufacture, however, as shown it was possible to achieve extended bandwidths with a non-standard design. One possible explanation is that the transverse resonance method is still an approximate method that relies on various assumptions, some of which might not be valid for a short axial length DRGH where the cross-section dimensions change quickly over axial length. Another possible reason is that using the definition of MUB, $\frac{{\lambda_c}^{10}}{{\lambda_c}^{30}}$, as defined in [38] and used extensively in literature when designing double-ridged horns is not applicable in some non-standard cases since the possibility exists that the TE_{30} does not exist or degenerates as shown in [80]. The results from this study show that the fact that a higher-order mode exists does not necessarily lead to degraded performance. The type of modes that could lead to performance degradation at the high-frequency end is expected to be modes that have maximum field intensity between the ridges [80].

To further investigate this, near-field calculations were performed in FEKO at the interface between the launcher and flared waveguide and halfway along the length of the flared waveguide. At the launcher and flared waveguide interface the higher-order modes can be evanescent or propagating. It is expected that further along the inside of the flared waveguide only propagating higher-order modes will exist. Figure 3.46 shows some of the near fields calculated in FEKO. A review of all the frequencies revealed that the field, basically TE_{10}, at the low-frequency end, increases in complexity as the frequency increases, indicative of the existence of propagating higher-order modes.

Figure 3.47 shows a near field cut taken through the *H*-plane, even at the highest frequency of operation the highest intensity field sits between the ridges and the field between the ridges stays mostly uniform, a maximum deviation of 1.7 dB is observed. The ripple in the field between the ridges increases with an increase in frequency as does the field outside the ridges. As long as the ripple in the field between the ridges as well as the field outside the ridges is controlled the pattern will not deteriorate significantly.

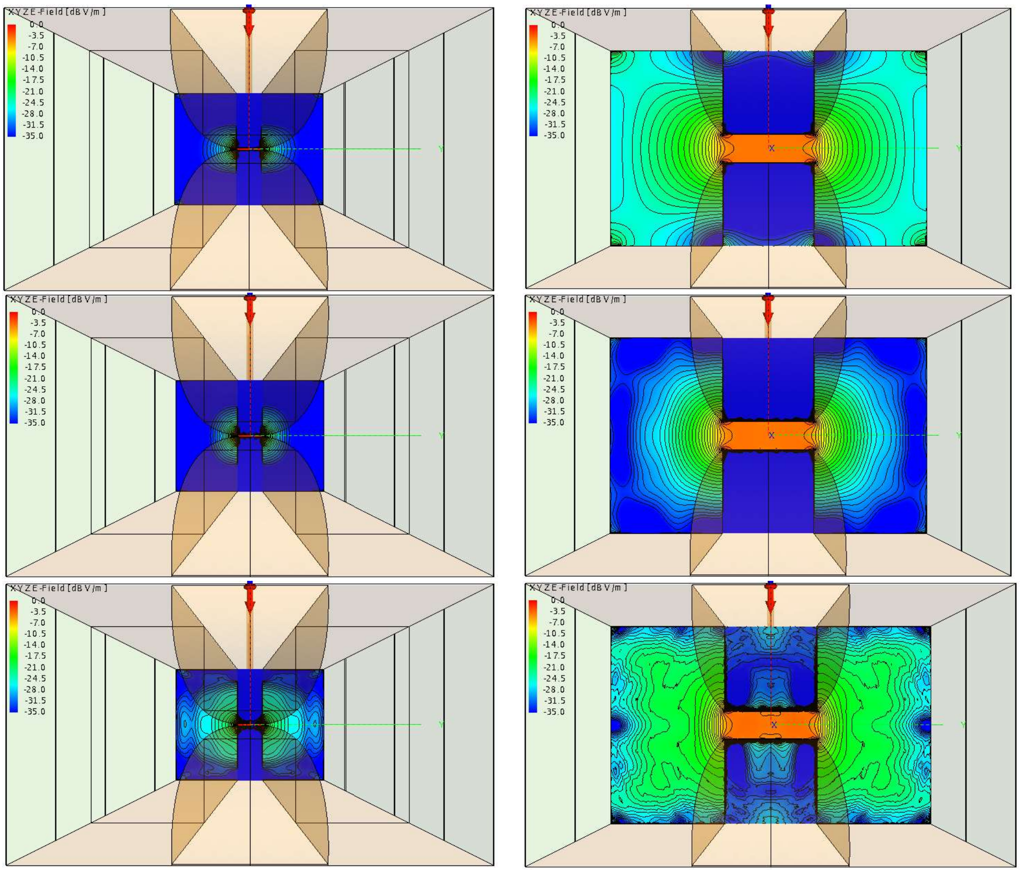

Figure 3.46. Near field calculations, (top) 0.5 GHz, (middle) 9.25 GHz and (bottom) 18 GHz for the 0.5-18 GHz DRGH at the launcher and flared waveguide interface (left) and inside the flared waveguide (right)

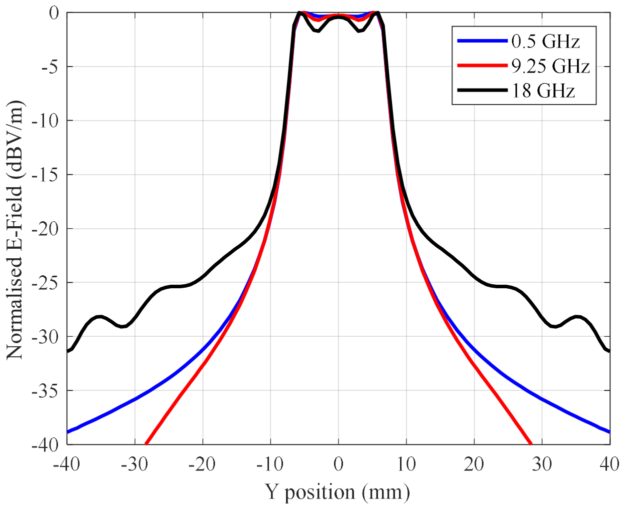

Figure 3.47. Near field cut for calculations at launcher and flared waveguide interface.

Simulations were subsequently performed at frequencies above 18 GHz, the VSWR and boresight gain can be seen in Figure 3.48. At first glance the antenna operates up to at least 22 GHz, however, looking at the radiation patterns it is clear that the pattern starts to deteriorate above 19 GHz, see Figure 3.49.

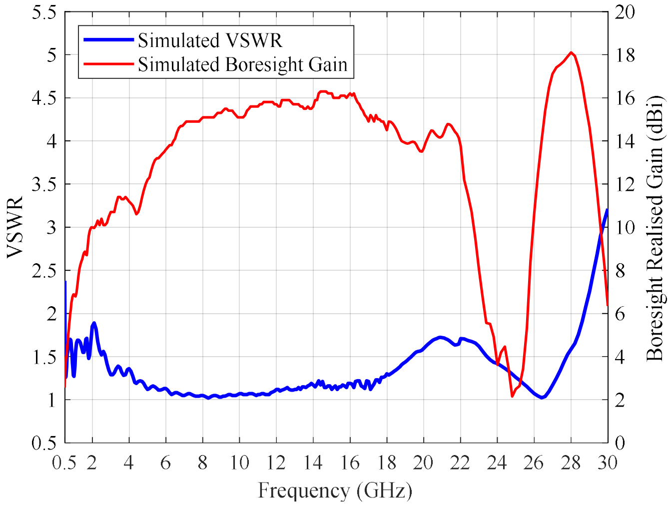

Figure 3.48. Extended frequency range simulated VSWR and boresight gain for the 0.5-18 GHz DRGH.

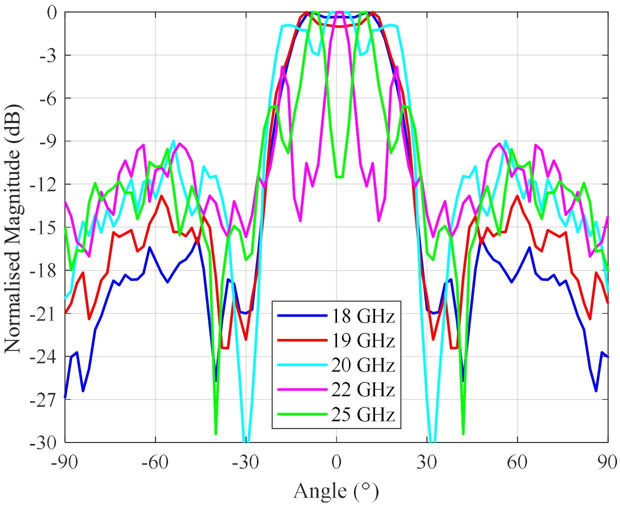

Figure 3.49. Extended frequency range simulated *H*-plane patterns for the 0.5-18 GHz DRGH.

Ripple in the main beam increases dramatically forming large side lobes above 20 GHz. The unwanted radiation outside the main beam also increases gradually to a level above -10 dB at 22 GHz. The pattern completely breaks up at 25 GHz, with a large null on boresight. Figure 3.50 shows the results for a near field cut in the *H*-plane which when compared to Figure 3.47 can provide some guidance, i.e. the *E*-Field ripple should be less than 2 dB inside the ridge gap and the *E*-Field magnitude outside the gap should be nominal monotonically decreasing to a level less than -20 dB at a distance of more than the ridge width away from the centreline.

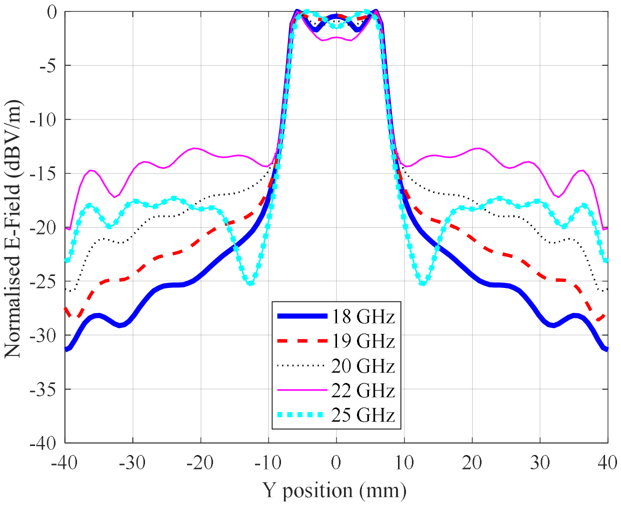

Figure 3.50. Near field cut for calculations at the launcher and flared waveguide interface above 18 GHz.

Since FEKO can only calculate the total electric fields, a modal study was performed in CST using the dimensions from Figure 3.43. It was found that at least 25 modes are present within the 0.5-18 GHz bandwidth. The modal patterns are shown in Figure 3.51 (calculated at 9.25 GHz) and Table 3.3 provides the applicable information. The mode number increases from left to right, top to bottom in Figure 3.51. The first modal pattern (top left, TE_{10}) compares well to the near fields shown in Figure 3.46, calculated in FEKO, however, it is interesting to note that the cut-off frequency for the TE_{10} mode as calculated using the transverse resonance method was found to be 421 MHz while CST predicts a cut-off frequency of 130 MHz. The calculated TE_{30} mode cut-off frequency is the same as CST i.e. 4.36 GHz.

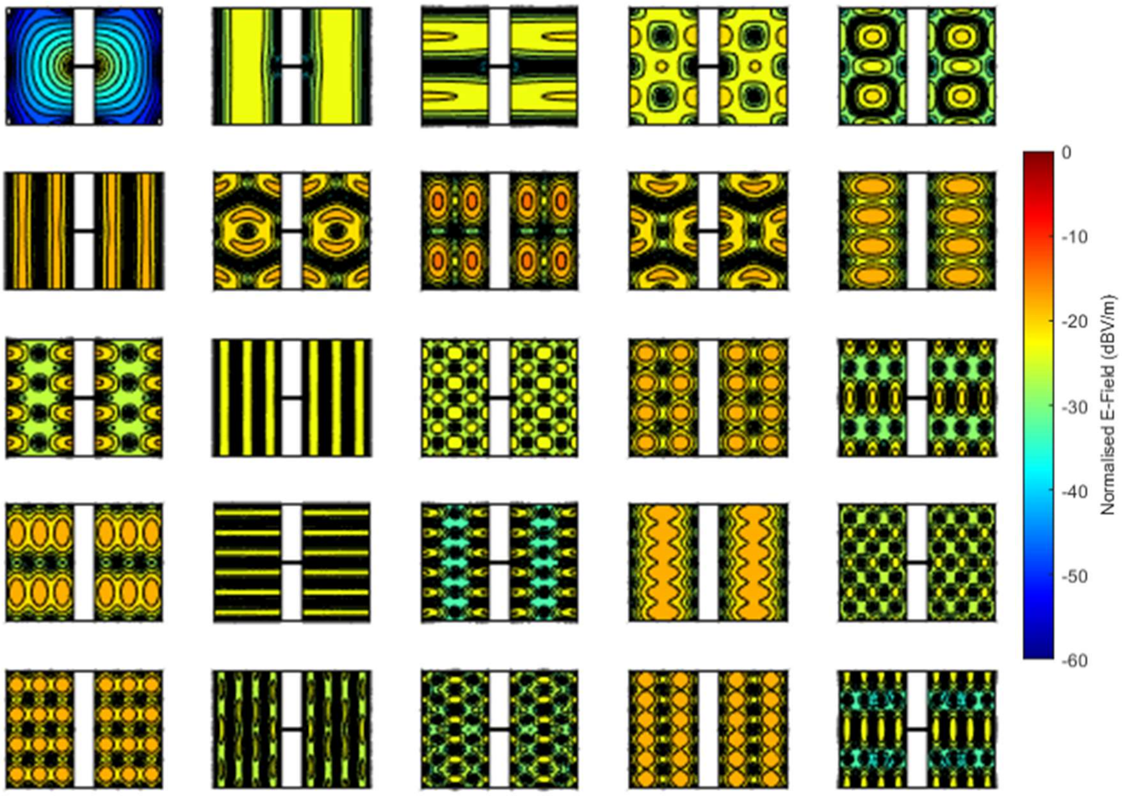

Figure 3.51. Mode patterns calculated at 9.25 GHz.

Figure 3.52 shows a cut through the *H*-plane for the different modes. The TE_{10} mode compares well to the total field calculated for 9.25 GHz in Figure 3.47 which would indicate that at least at 9.25 GHz the operation is higher-order mode free. It is clear from the performance of the designed 0.5-18 GHz DRGH antenna that although the double-ridged waveguide supports higher-order modes, these modes are either not excited or the coupling from the coax-to-waveguide launcher to the higher-order modes is so small that they do not impact the input impedance or radiation patterns of the DRGH. This also clearly shows that it is not always correct to use the metric $\frac{{\lambda_c}^{10}}{{\lambda_c}^{30}}$ to determine the MUB of ultra-broadband DRGH antennas.

Table 3.3. CST Mode information.

Mode Nr.	Type	f_c (GHz)	Mode Nr.	Type	f_c (GHz)
1	TE	0.13	14	TM	13.21
2	TE	4.36	15	TE	13.89
3	TE	5.03	16	TM	13.89
4	TE	6.65	17	TE	14.99
5	TM	6.6	18	TE	15.59
6	TE	8.65	19	TM	15.6
7	TE	9.99	20	TE	16.3
8	TM	9.98	21	TM	16.37
9	TE	10	22	TE	17.26
10	TM	10.89	23	TE	17.29
11	TE	10.9	24	TM	17.3
12	TE	12.97	25	TE	17.96
13	TE	13.21			

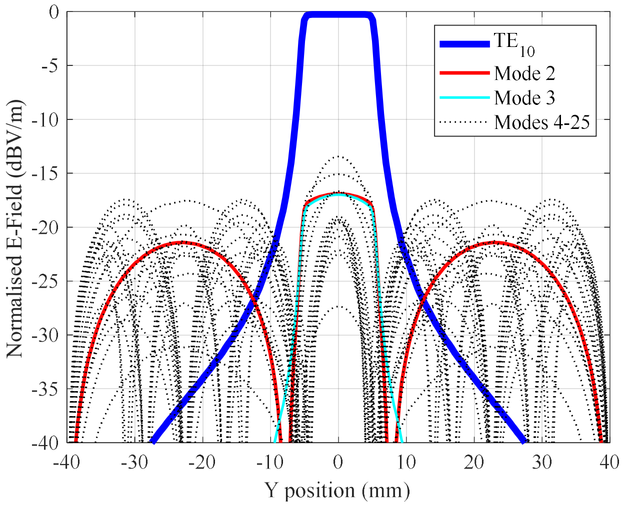

Figure 3.52. Mode pattern *H*-plane cuts for Figure 3.51.

3.8 SUMMARY

This chapter showed how a 36:1 (0.5-18 GHz) DRGH was designed from the original 1-18 GHz DRGH. The chapter started by presenting the requirements to which the 0.5-18 GHz design should adhere. EM simulations were used extensively in this chapter with a detailed discussion on the implementation of the 1-18 GHz DRGH in FEKO in Section 3.2. Using this model as a starting point an investigation was performed into the bandwidth-limiting parts and or sub-assemblies of the antenna in Section 3.3 with the findings utilised in Section 3.4 to experimentally design an extended bandwidth DRGH. Most of the design changes were done on the coax-to-waveguide launcher and ridges as indicated by the findings of Section 3.3. The subsequent mechanical design and manufacture presented in Section 3.5 yielded a prototype, measured in Section 3.6, which meets the requirements as set out in Section 3.1.

Due to the excellent comparison between measured and simulated results, it is also clear that an accurate EM simulation model is an indispensable tool for the design of extended bandwidth DRGH antennas. The modal study of Section 3.7 showed that although the designed double-ridged waveguide supports higher-order modes, these modes are either not excited or the coupling from the coax-to-waveguide launcher to the higher-order modes is so small that they do not impact the input impedance or radiation patterns of the antenna. This also indicates that it is not always correct to use the metric $\frac{\lambda_c{}^{10}}{\lambda_c{}^{30}}$ to determine the MUB of these antennas since in some non-standard cases the possibility exists that the TE_{30} does not exist or degenerates [80] and some higher-order modes do not necessarily lead to degraded performance. The increased operational bandwidth of the antenna presented in this chapter now makes it possible for a single antenna to cover the full frequency range from 0.5 to 18 GHz, as opposed to at least two antennas in the past. Even though the production cost for the proposed horn may be higher than a conventional 1-18 GHz DRGH antenna, due to the complexity of the ridges and the larger size of the antenna, requiring only one horn will be much more cost-effective.

CHAPTER 4 0.5-50 GHZ DRGH DESIGN

Typical anechoic chamber antenna measurement setups split the 0.5-40 GHz band into 0.5-2 GHz, 2-18 GHz and 18-40 GHz setups with several DRGH antennas covering these frequency ranges used as source and reference antennas. To enable a single band measurement setup to cover the full 0.5-40 GHz band would require a 0.5-40 GHz DRGH. Furthermore, the VNAs at the author's disposal work up to 50 GHz and thus operation up to 50 GHz would be desirable. This chapter shows how the 0.5-18 GHz design from Chapter 3 and [45] was used to further investigate what parts and or sub-assemblies of the DRGH limits the bandwidth and how these parts and or sub-assemblies can be redesigned to extend the DRGH bandwidth to 100:1 (0.5-50 GHz), [87].

The requirements to which the antenna must adhere are outlined in Section 4.1. Section 4.2 shows how the EM model of the 0.5-18 GHz DRGH developed in Chapter 3 can be improved to ensure accurate simulations up to 50 GHz. The investigation into the design limits is shown in Section 4.3. As in Chapter 3, the different parts and sub-assemblies of the DRGH are removed or adjusted step by step and the effect on the performance is observed. The order of removal/adjustment was kept the same as in Chapter 3. Just as in Chapter 3 it was found that a redesign of the coax-to-waveguide launcher and ridges are required to further extend the bandwidth. It was also necessary to use a 2.4 mm connector to allow operation up to 50 GHz. As this would limit the power handling of the antenna it was decided to remove the power handling requirement and, therefore, also the restriction on the use of absorbers and/or lenses. This design is more suitable for antenna measurement applications and EMC/I tests where high power handling is not required.

Section 4.4 shows how the various parts and or sub-assemblies were redesigned to extend the bandwidth and ensure good performance. The final simulated results for the new 0.5-50 GHz DRGH design are also presented in Section 4.4. From the electrical design, a mechanical design for a prototype was performed and the prototype was manufactured, mostly using 3D printing as shown in Section 4.5. The prototype was tested in an anechoic chamber, the measured results from these tests are presented in Section 4.6. Finally, the chapter is summarised in Section 4.7.

4.1 REQUIREMENTS

From Section 3.3.1 it was already clear that for operation up to 50 GHz, it would be necessary to use a 2.4 mm connector. This connector would significantly reduce the DRGH power handling ability to less than 16 W CW at 50 GHz [88], therefore the restriction that absorbers and/or a lens cannot be used was removed. From the study in Section 2.6 it is clear that the use of absorbers and lenses could aid in extending the bandwidth of DRGH antennas. This would limit the application of such a DRGH to antenna measurement (source and reference, power handling requirement 1 W CW or less) and specific EMC/I tests that do not require high power. The rest of the requirements in terms of VSWR, aperture size, gain, radiation pattern and polarisation performance were kept the same as in Section 3.1.

4.2 EM MODEL OF 0.5-18 GHZ HORN

For simulations up to 50 GHz the mesh element size needs to be reduced for the 0.5-18 GHz DRGH EM model with a corresponding significant increase in resource requirements. It would not be feasible to run a large amount of simulations using the detailed model of Figure 3.23(b) and initial investigations showed that the basic model of Figure 3.23(a) would not be accurate enough for simulations above 18 GHz. A model, as shown in Figure 4.1(b), was therefore created with several improvements implemented to increase accuracy as follows:

- The sidewall material was modelled using FEKO's thin dielectric sheet approximation (0.8 mm thick) with the electrical properties of FR4, i.e. a dielectric constant of 4.8 and loss tangent of 0.017 instead of infinitely thin metallic grids without any substrate material.
- An SMA connector model was added with the dielectric core modelled using the SEP and the electrical properties of PTFE i.e. a dielectric constant of 2.08 and loss tangent of 0.0009.
- Metallic triangles having the conductivity of gold (4.098×10^7 S/m, feed), aluminium (3.816×10^7 S/m, mechanical parts) and copper (5.813×10^7 S/m, sidewall strips) replaced the lossless PEC triangles.
- All mechanical triangles on machined parts were modified to have a surface roughness equivalent to typical machining tolerances, Root Mean Square (RMS) of 22×10^{-6} m.

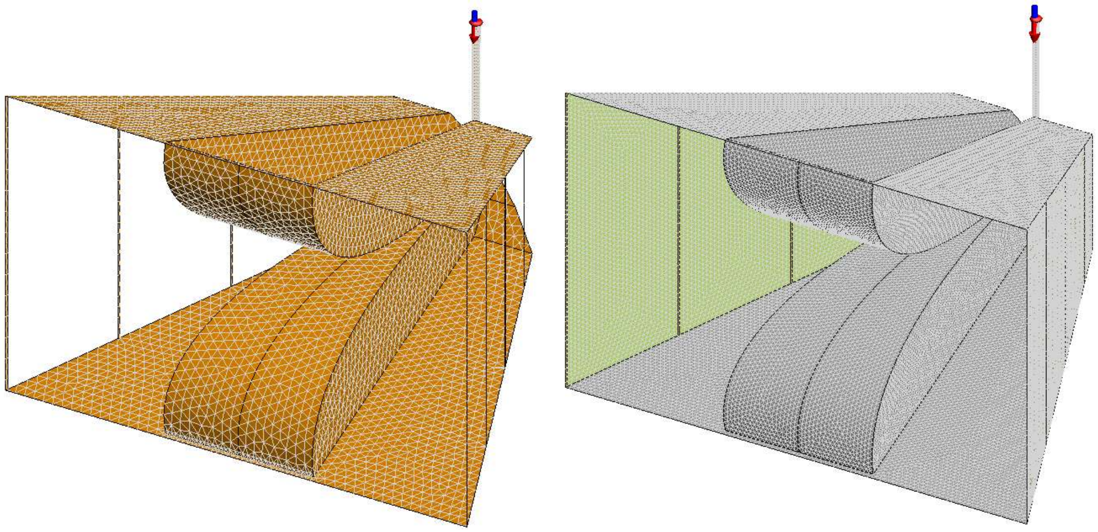
(a) (b)

Figure 4.1. (a) Basic and (b) improved 0.5-18 GHz DRGH FEKO meshed models.

Apart from the wavelength being reduced to that of the new highest simulation frequency of 50 GHz, the same typical mesh element settings were used as described in Section 3.2. The final model consisted of 98 038 triangles of which 97 562 were metallic triangles in free space, 448 metallic triangles coinciding with the surface of a dielectric and 28 triangles for the surface of a dielectric. The simulation frequency step size was set to 500 MHz above 18 GHz. To verify this model additional measurements were performed in the 18-40 GHz band using a standalone VNA for the VSWR and a small rectangular anechoic chamber using another VNA for the gain and pattern measurements in 100 MHz steps, see Figure 4.2. At this stage, the 50 GHz VNA and a reference antenna working up to 50 GHz were not available so they have been carried out up to 40 GHz.

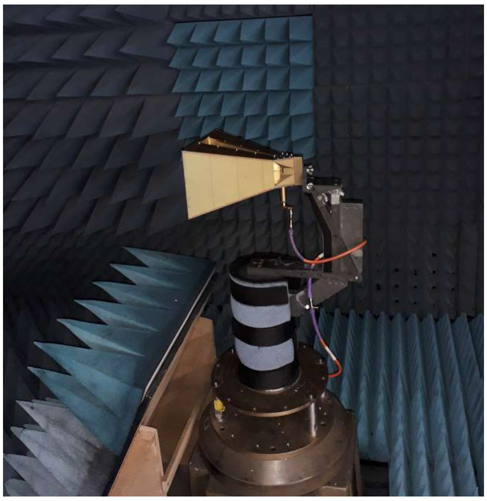

Figure 4.2. Small rectangular anechoic chamber measurement setup.

The comparison between the measured and simulated VSWR is shown in Figure 4.3(a). The VSWR stays below 2:1 to just before 29 GHz despite the antenna having an SMA connector which is typically rated to at most 26.5 GHz. The comparison between the measured and simulated vertical polarised boresight gain is shown in Figure 4.3(b). From the dips and peaks in gain, it is clear the pattern breaks up above 20 GHz. This was confirmed by looking at the simulated 3D patterns, see Figure 4.4. Clearly most of the radiation is still directed along the ridges, but something is causing pattern break-up. In the past, the reason for the gain dips and pattern deterioration has been widely accepted as the existence of higher-order modes, but it will be shown further on in this chapter that the cause is also related to reflections and diffraction from the cavity and sidewalls.

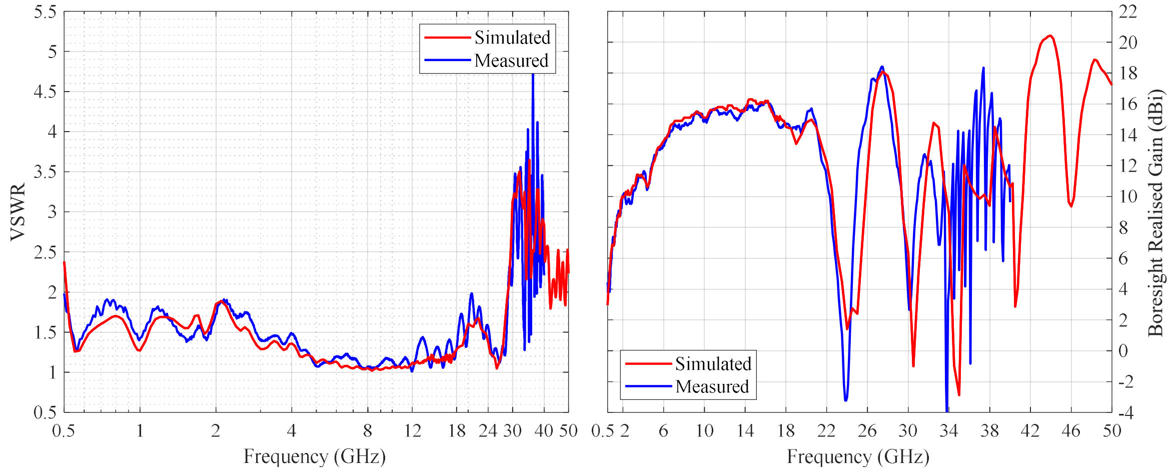

(a) (b)

Figure 4.3. (a) VSWR and (b) boresight gain comparison between simulated and measured results for the 0.5-18 GHz DRGH.

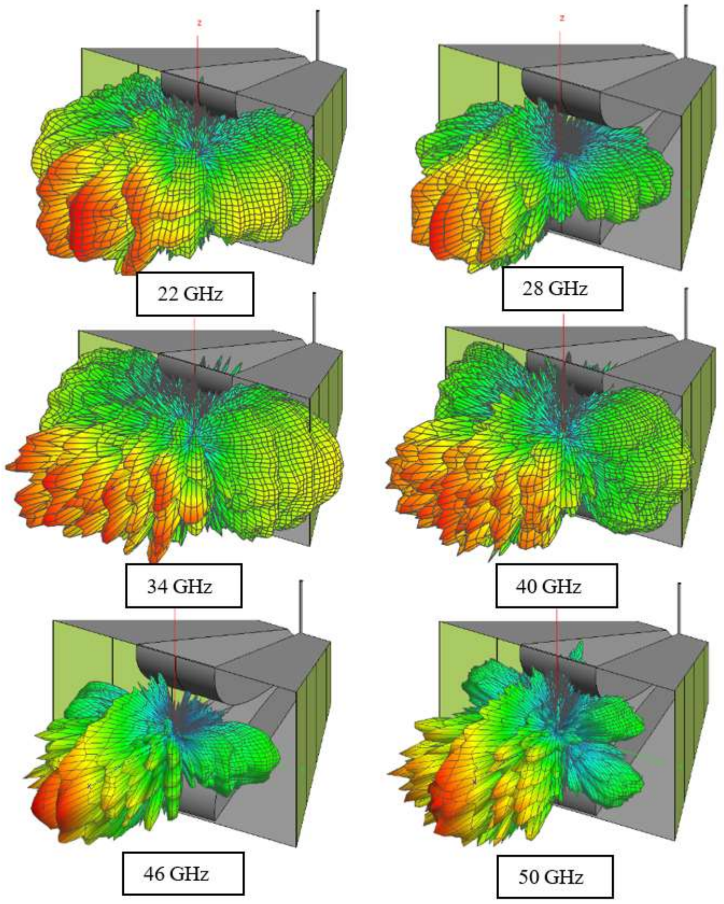

Figure 4.4. Selected 3D patterns in the millimetre Wave (mmW) band.

4.3 INVESTIGATION INTO DESIGN LIMITS

This section follows a similar investigative process as that one shown in Chapter 3, Section 3.3 with the EM model discussed in the previous section used as the basis for the study. As a first step, however, all the dimensions of the model were scaled by a factor of 0.5 to determine the parametric space. The parametric space is nominally defined by the dimensions of the original design and the scaled design as the maximum and minimum dimensions, respectively.

4.3.1 Scaled Design

Figure 4.5(a) shows the VSWR and Figure 4.5(b) the gain, as expected the scaled model has decent performance from 1 GHz to 36 GHz. Although the gain and VSWR look acceptable from 36 GHz to 43 GHz, a review of the 3D patterns revealed the start of pattern breakup just above 36 GHz. It was hypothesized that reducing some of the dimensions of the horn antenna while keeping others unchanged could potentially enable wider operational bandwidth. It would, however, be necessary to identify which parameters need to be held constant and which parameters need to be reduced.

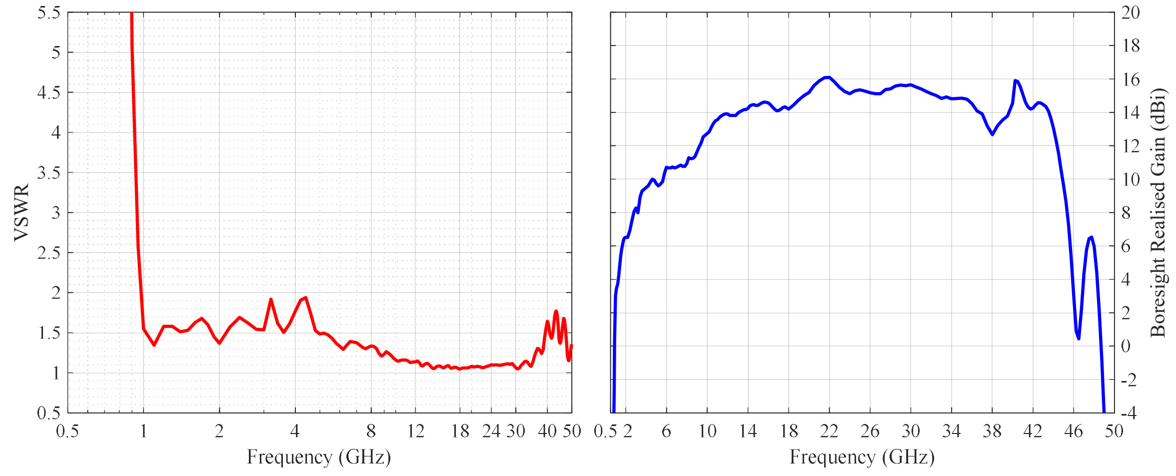

(a) (b)

Figure 4.5. (a) VSWR and (b) boresight gain for the scaled 0.5-18 GHz DRGH.

4.3.2 Coaxial Feed Investigation

It was decided to remove two possible sources of modes in the 0.5-18 GHz design. Firstly, the connector model (SMA) was removed from the FEKO model since the SMA could have modes above 26 GHz. Secondly, the coaxial feed impedance taper design from Section 3.5.1 was evaluated using (3.2) and it was found that it could support higher-order modes from 32.4 GHz. Using the information and equations in Section 3.3.1 the design was thus changed as follows to shift the higher-order mode cut-off frequency to above 40 GHz:

- The outer conductor diameter was changed to 2.92 mm.
- The inner conductor feed diameter at the connector end was changed to 1.27 mm.
- The inner conductor feed diameter at the ridge end was changed to 1.7 mm.

This design transforms the impedance from 50 Ω at the connector end to 32 Ω at the ridge feed point (see Section 3.3.1) over a length of approximately 75 mm with a cut-off frequency of 41 GHz. The simulated results, comparing the updated coaxial feed design with the original design are shown in Figure 4.6(a) and Figure 4.6(b).

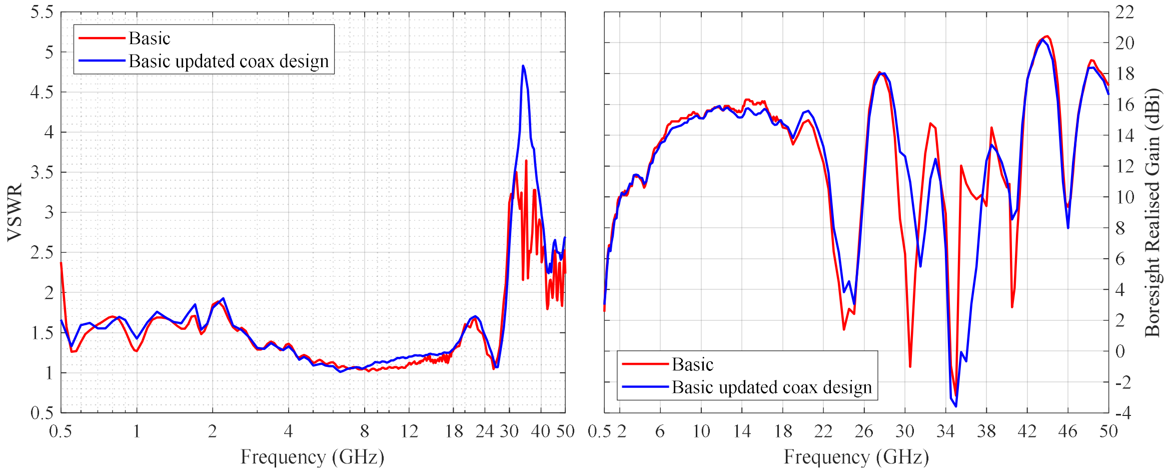

(a) (b)

Figure 4.6. (a) VSWR and (b) boresight gain comparison for the coaxial feed change.

The most notable impact these changes had was that the VSWR above 30 GHz changed from having several spikes to a single peak with increased magnitude and the changes in the gain dips in terms of frequency and magnitude between 30 and 42 GHz. Thus, as before, it looks like the coaxial feed design is not the bandwidth limiting factor in the 0.5-18 GHz DRGH design.

4.3.3 Sidewall Investigation

In this section, the effect of the sidewalls was evaluated. Figure 4.7(a) to Figure 4.7(d) shows the four simulation models used, in Figure 4.7(a) the reference model as described in Section 4.3, in Figure 4.7(b) the model with the dielectric substrate of the *E*-plane sides removed, in Figure 4.7(c) the model with the dielectric *E*-plane sides and grids removed and the model with both the *E*- and *H*-plane sides removed in Figure 4.7(d).

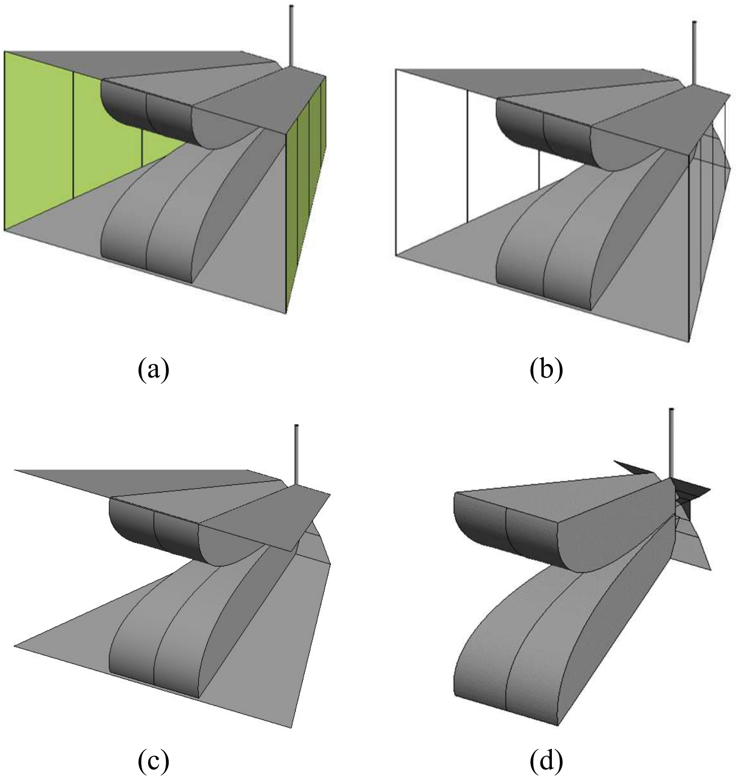
(a) (b)

(c) (d)

Figure 4.7. (a) Reference model , (b) model without dielectric substrate in *E*-plane sides, (c) model without *E*-plane sides and (d) model without *E*- and *H*-plane sides for the sidewall investigation.

The VSWR and boresight gain results for these simulations can be seen in Figure 4.8(a) and Figure 4.8(b). From these figures, the following were observed:

- Removing the dielectric substrate of the *E*-plane sides had virtually no effect on the VSWR, but influenced the gain above 20 GHz with a significant improvement above 40 GHz.
- Removing the *E*-plane grid as well had very little further effect on the mmW gain but resulted in degraded VSWR performance below 2 GHz which resulted in less gain below 2 GHz as well, similar to what was seen during the design investigation in Chapter 3.
- The additional removal of the *H*-plane sides degraded the VSWR and gain below 2 GHz further and had a slight effect on the gain between 22 GHz and 26 GHz.

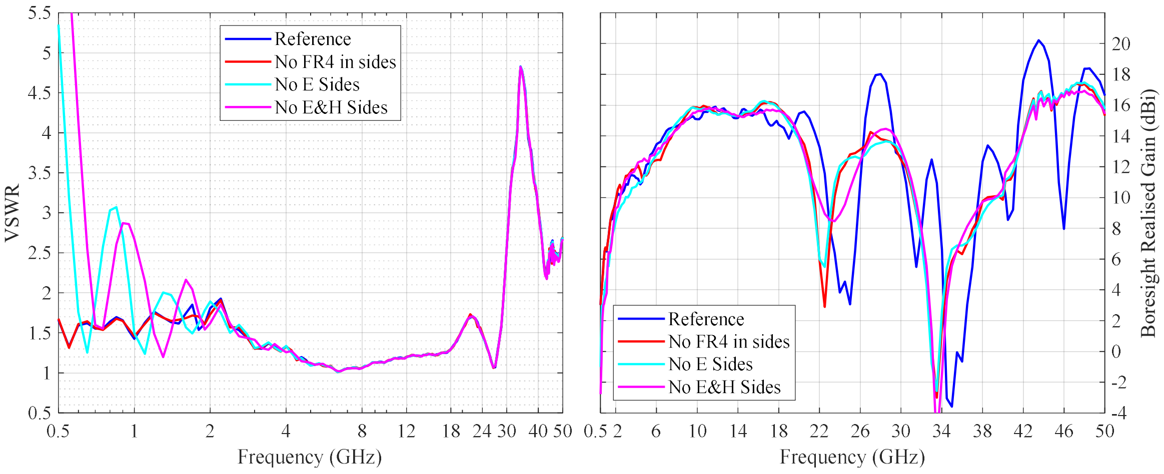

(a) (b)

Figure 4.8. (a) VSWR and (b) boresight gain comparison for the sidewall investigation.

The impact of the sidewalls on the gain between 20 GHz and 50 GHz looks deceptively small, just a slight frequency shift of peaks and dips, however, looking at the 3D patterns reveals that the sidewalls have a significant impact on the patterns. Due to the large volume of the results only a few examples are shown, Figure 4.9 shows the 3D vertical polarised pattern at 22 GHz for the four models of Figure 4.7 sequentially from left to right, top to bottom and Figure 4.10 shows the patterns at 28 GHz, Figure 4.11 at 34 GHz, Figure 4.12 at 40 GHz and Figure 4.13 at 46 GHz.

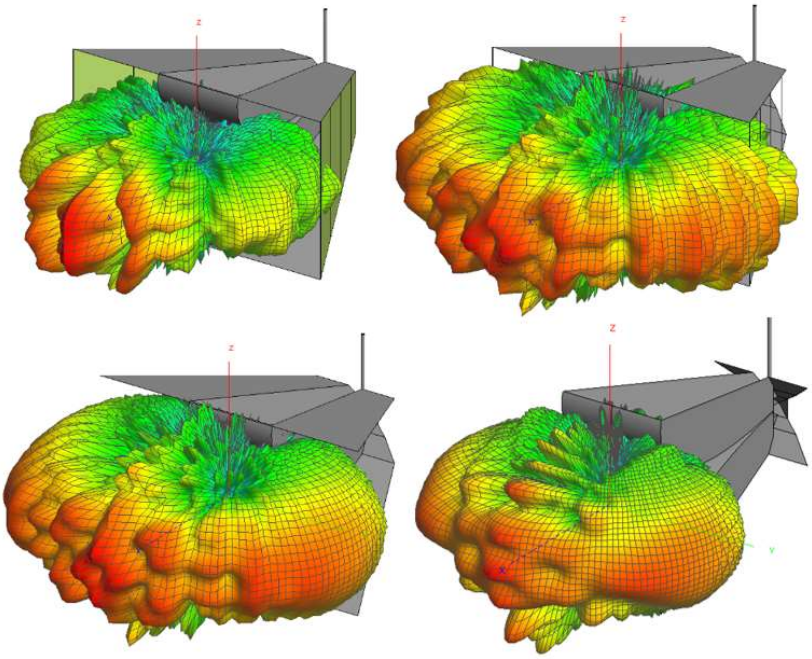

Figure 4.9. 3D patterns for the sidewall investigation at 22 GHz.

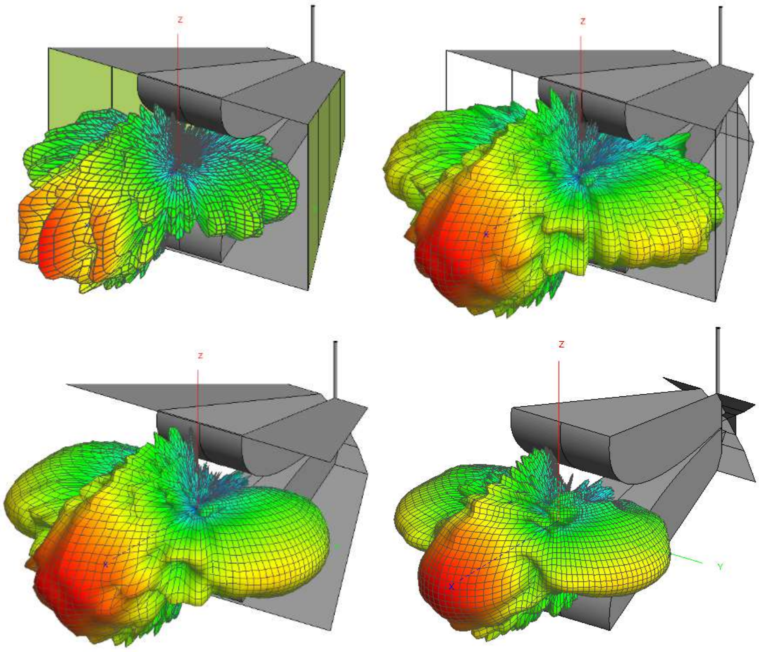

Figure 4.10. 3D patterns for the sidewall investigation at 28 GHz.

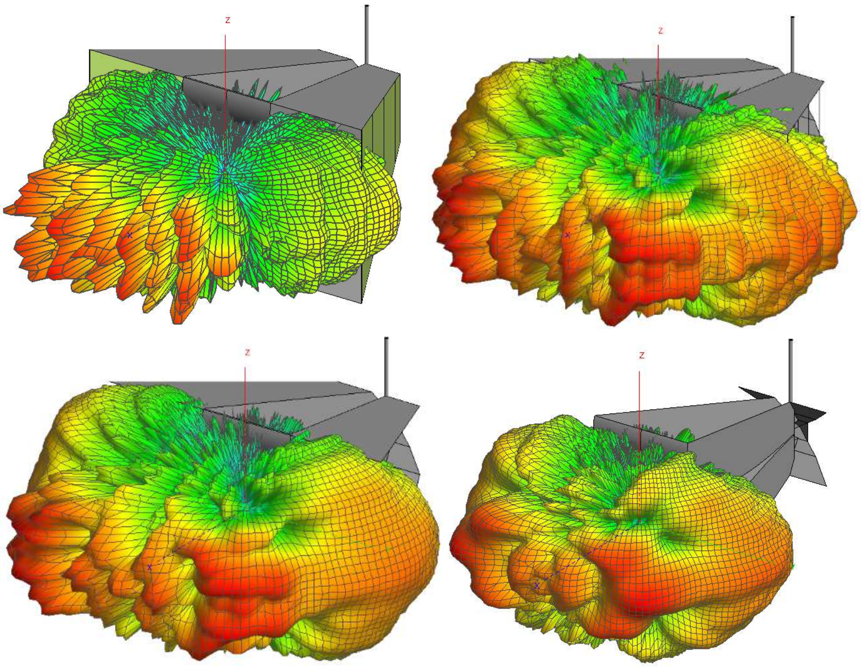

Figure 4.11. 3D patterns for the sidewall investigation at 34 GHz.

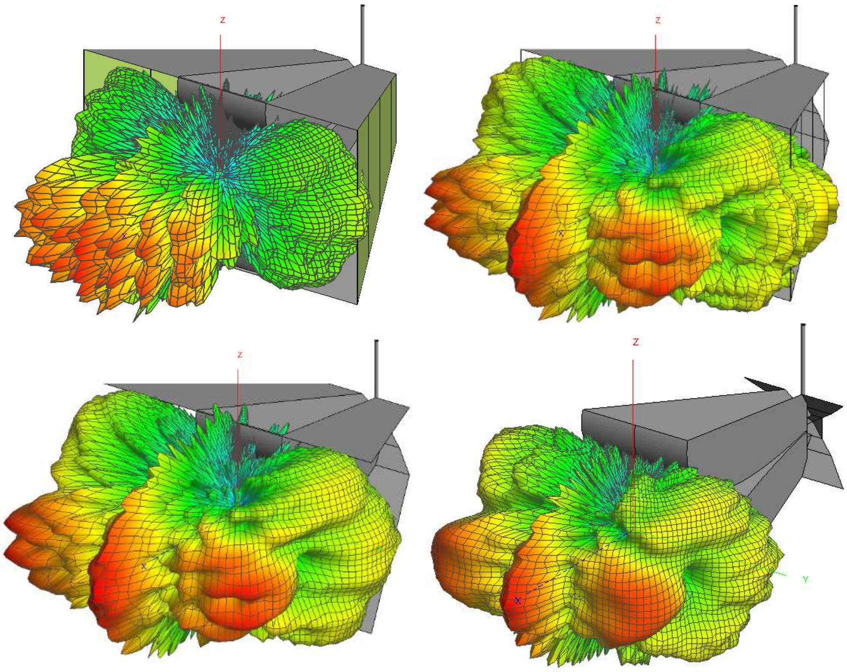

Figure 4.12. 3D patterns for the sidewall investigation at 40 GHz.

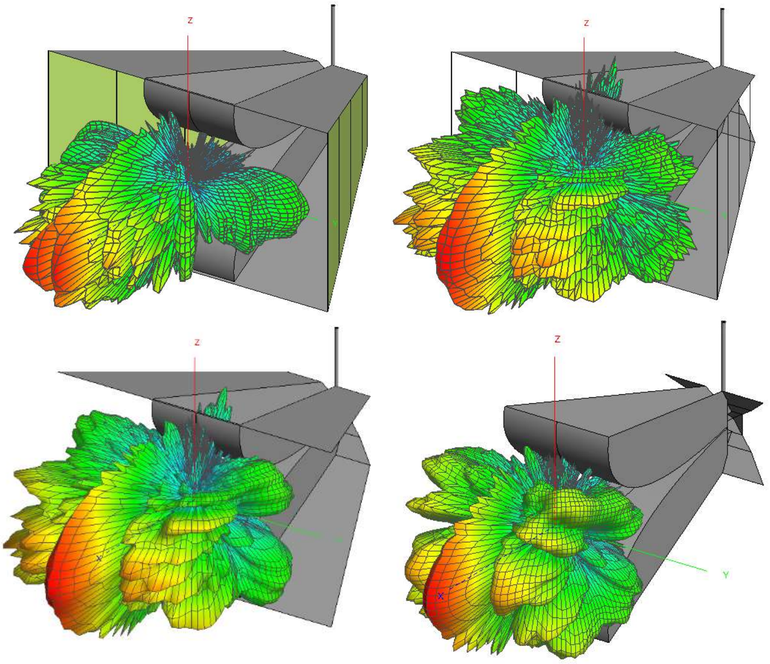

Figure 4.13. 3D patterns for the sidewall investigation at 46 GHz.

As can be seen from these figures the sidewalls have a significant influence on the ripple structure in the main beam as well as the side lobes. As seen before in the investigation of Chapter 3 it does look like the sidewalls affect the DRGH usable bandwidth with a decrease in performance and bandwidth with removal of the sidewalls at the low end of the frequency band. Furthermore, the sidewalls influence the radiation pattern performance at the high-frequency end, especially above 40 GHz where the dielectric substrate of the *E*-plane sidewalls causes significant degradation.

4.3.4 Coax-to-Waveguide Launcher Investigation

Similar to Section 3.3.3 for the first set of coax-to-waveguide launcher tests the model without any sidewalls was used from the previous section as a starting point. The cavity was modified step by step, by removing parts of the cavity until there was no cavity remaining. The models are shown in Figure 4.14(a) to Figure 4.14(d), in Figure 4.14(a) the basic model, in Figure 4.14(b) the model with forward cavity flares removed, in Figure 4.14(c) the model with inner cavity flares apart from the section directly behind the ridge removed and the model without a cavity in Figure 4.14(d).

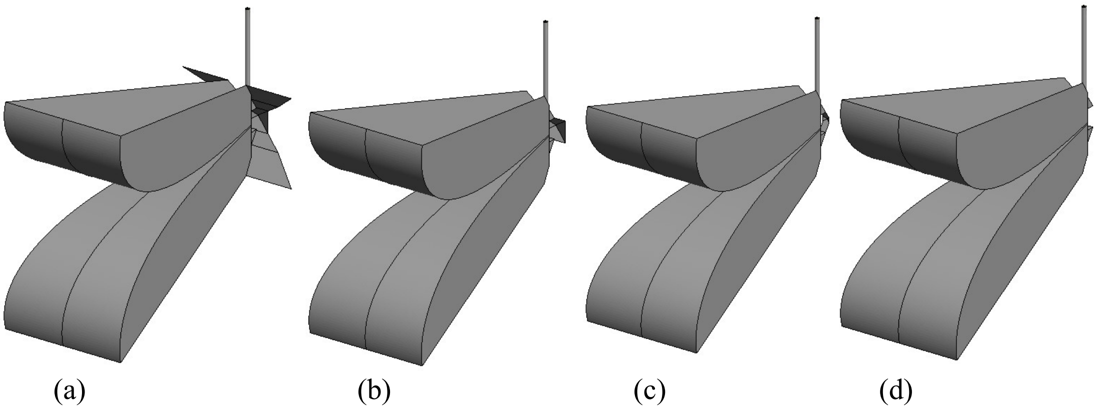
(a) (b) (c) (d)

Figure 4.14. (a) Reference model, (b) model without forward cavity flares, (c) model without inner cavity flares and (d) model without cavity for the cavity investigation with no sidewalls.

The VSWR and boresight gain results for these simulations can be seen in Figure 4.15(a) and Figure 4.15(b), respectively. From these figures, the following was observed:

- Removing the first section of the cavity had very little effect on both the VSWR and gain.
- For the next step there are more significant changes, the VSWR peaks increase around 0.85 GHz and reduce around 33.5 GHz. The gain improves around 22.5 GHz and above 36 GHz but reduces around 28 GHz and above 43 GHz.
- Removing the full cavity significantly degrades the VSWR below 1 GHz while the sharp gain dip around 34 GHz improves to above 5 dBi.

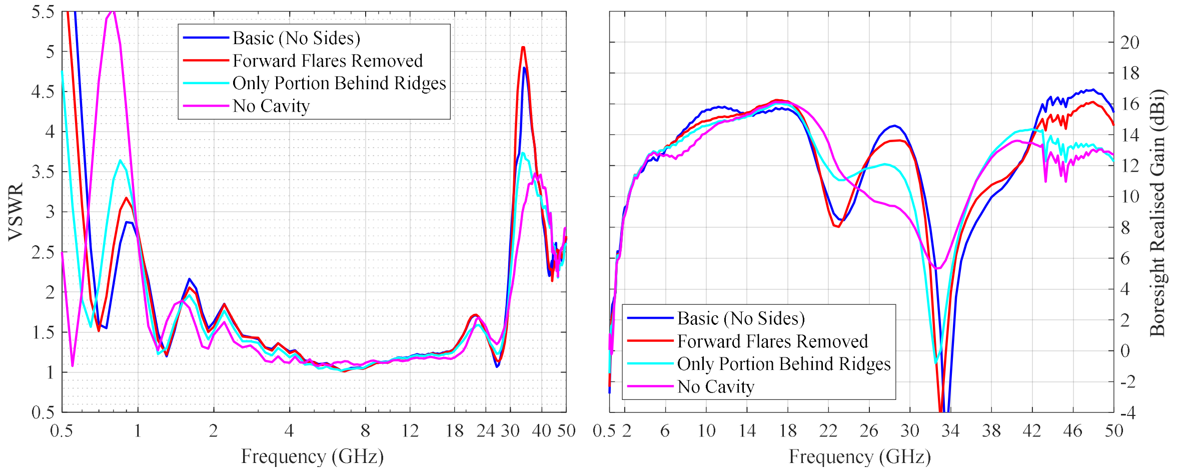

(a) (b)

Figure 4.15. (a) VSWR and (b) boresight gain comparison for the cavity investigation.

Similar to the impact of the sidewalls, the impact of the cavity on the patterns above 20 GHz is significant with a few examples being shown in Figure 4.16 to Figure 4.20.

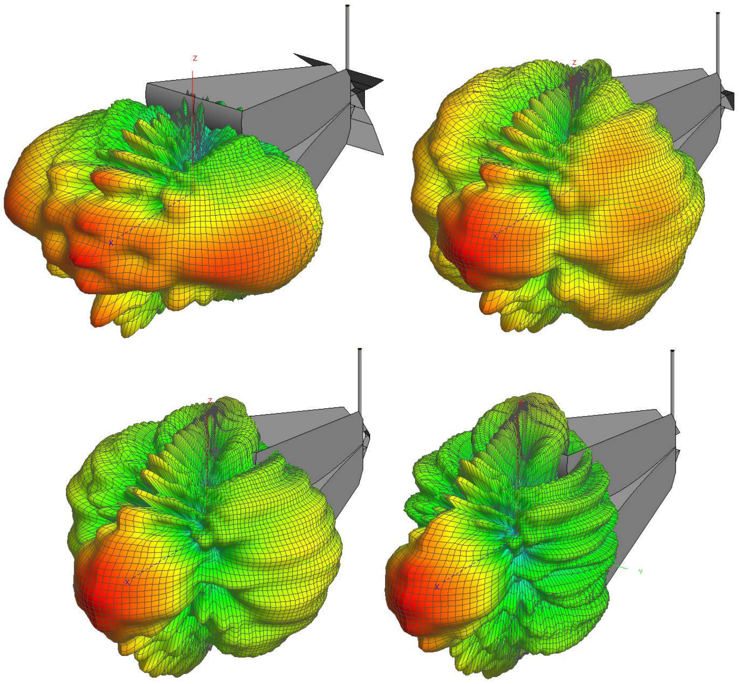

Figure 4.16. 3D patterns for the cavity investigation at 22 GHz.

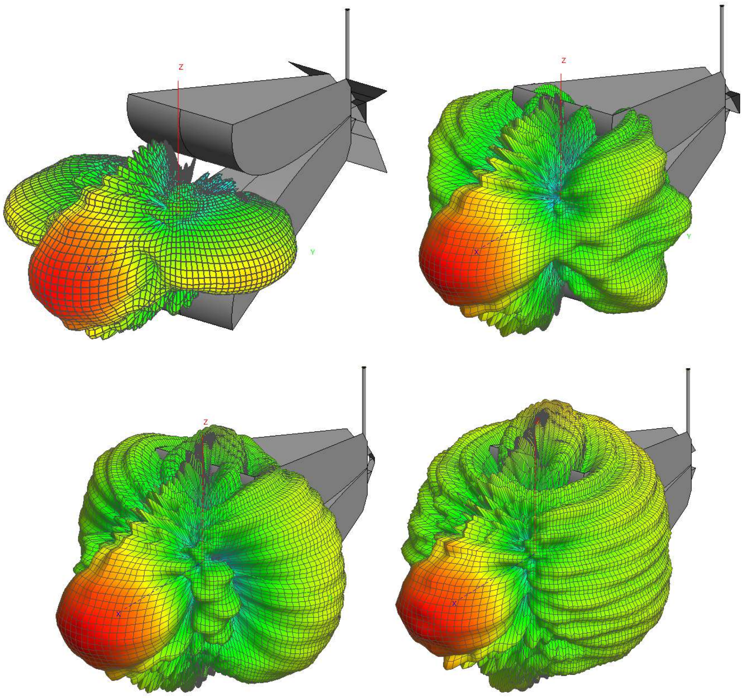

Figure 4.17. 3D patterns for the cavity investigation at 28 GHz.

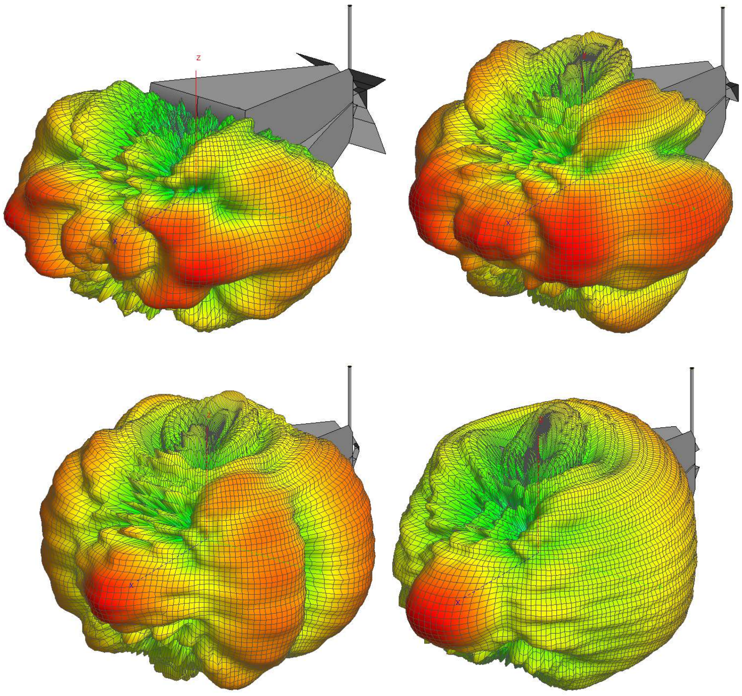

Figure 4.18. 3D patterns for the cavity investigation at 34 GHz.

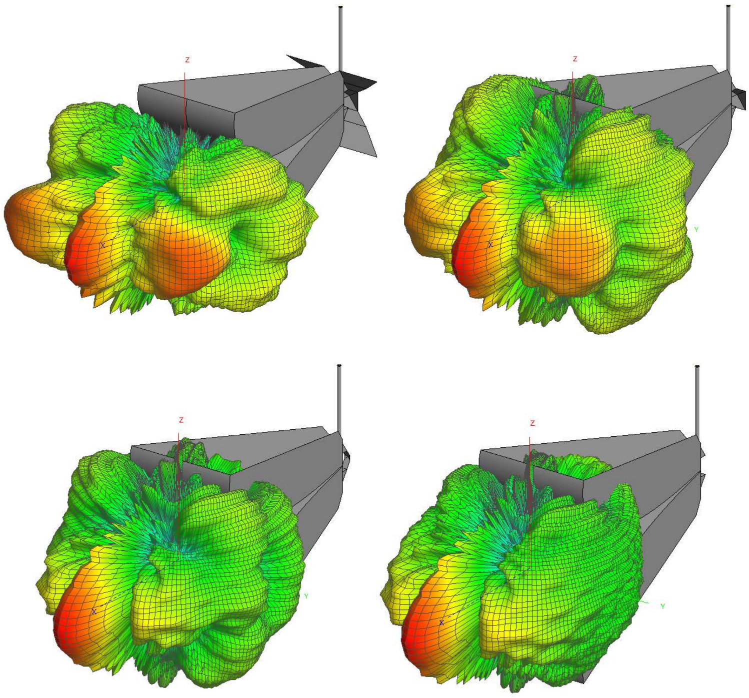

Figure 4.19. 3D patterns for the cavity investigation at 40 GHz.

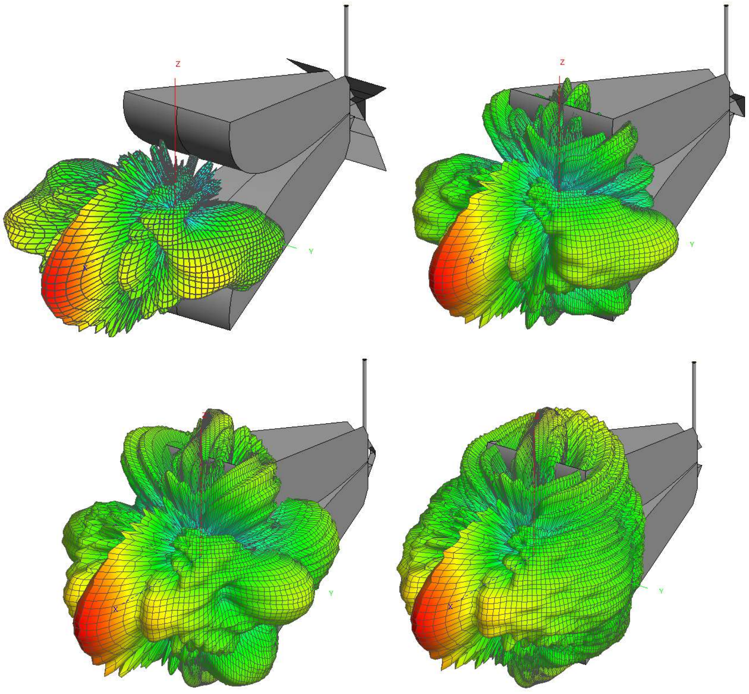

Figure 4.20. 3D patterns for the cavity investigation at 46 GHz.

A review of all the 3D patterns over the full 0.5-50 GHz band shows that for the case of no sidewalls and no cavity, a usable main beam is maintained over the full frequency range. There is, however, a significant back lobe, the worst case being only 5 dB below the main lobe. It was also found that above 20 GHz side lobes start to appear and increase to around 10 dB below the main lobe. It is suspected that the pattern breakup at high frequencies, especially in the mmW band is due to these side lobes and back lobes interacting with the cavity and sidewalls. The results in this and the previous section show that the 0.5-18 GHz DRGH sidewalls and coax-to-waveguide launcher design cause significant pattern deterioration in the mmW band. Apart from that, the performance of the 0.5-18 GHz DRGH ridge design on its own is also far from desirable.

4.3.5 Ridge Investigation

In the next step of the investigation, the ridge design was investigated using the last model of the previous section as a starting point. For faster simulations, the model was adjusted by removing the impedance transformer and replacing it with a constant width feed pin with a diameter of 1.7 mm inside the ridge gap with a 1 mm extension, for practical implementation of the FEKO waveguide feed, into the ridge with an outer diameter of 2.92 mm see Figure 4.21(a) and Figure 4.21(b).

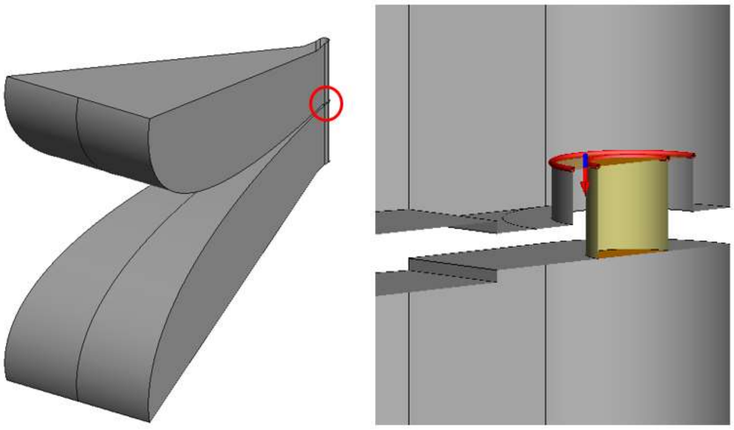

(a) (b)

Figure 4.21. (a) Simplified FEKO ridge with (b) close-up view of the simplified feed.

The structure of the ridge around the feed was also simplified since removing the cavity in the previous section introduced several sharp corners and steps. The effect of these changes can be observed in Figure 4.22(a) for the VSWR and Figure 4.22(b) for the gain. Some of the gain ripple is reduced as well as most of the highest VSWR peaks.

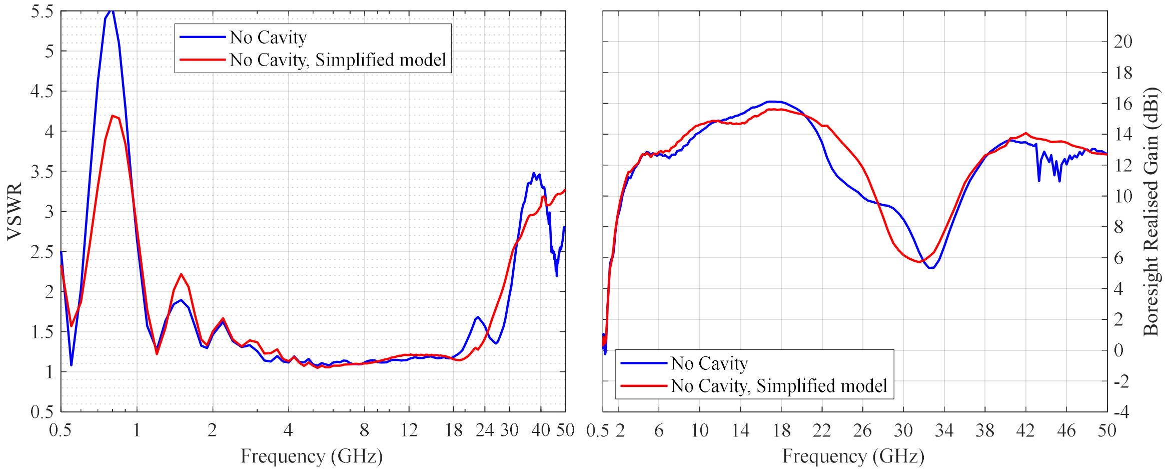

(a) (b)

Figure 4.22. (a) VSWR and (b) boresight gain comparison for the simplified ridge model.

The effect of several ridge parameters was then investigated by performing a parametric study, with the following parameters adjusted:

- Ridge gap.
- Ridge width - note the ridge width taper angle was kept the same, only the width at the start of the ridge was changed.

The parametric adjustment was performed using a scale factor less than 1 to reduce the ridge parameters' dimensions since it is to be expected that for a higher frequency of operation, the ridge parameters need to become smaller, refer to Section 4.3.1. The parameters were first scaled independently starting with the ridge gap. Figure 4.23(a) shows the VSWR and Figure 4.23(b) the gain for a scale factor from 1 to 0.5 in increments of 0.05 for the ridge gap. As the gap size decreases the VSWR degrades across the band, indicating a change in ridge impedance, with significant increases in VSWR observed around 800 MHz and above

30 GHz. The gain stays mostly the same with only the dip around 32 GHz becoming deeper with reduced gap size. Looking at the patterns reveals the cause of this dip which is the degradation of the beam from a "flat top" at a scale factor of 1 to the point that the beam splits into two lobes between 28 GHz to 35 GHz for smaller scale factors, see for example the results at 31.5 GHz in Figure 4.24.

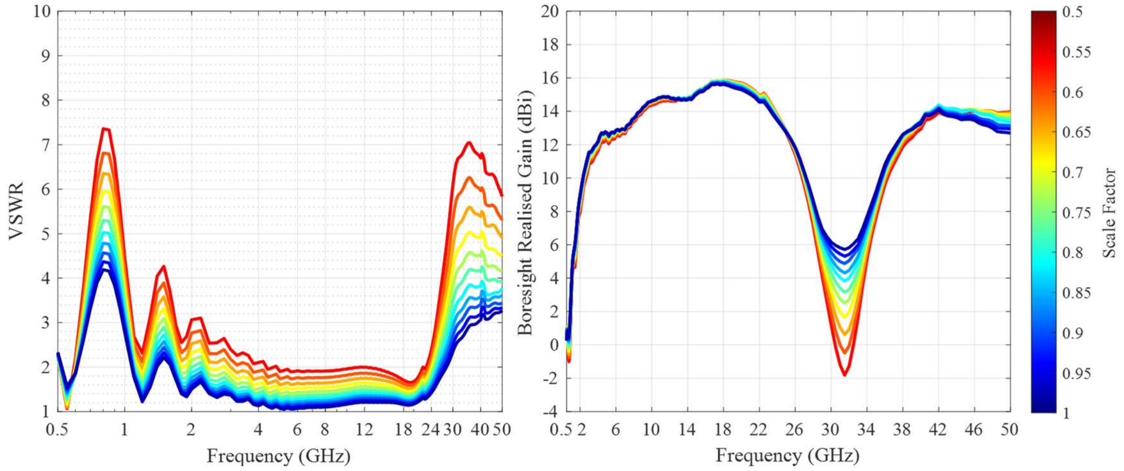

(a) (b)

Figure 4.23. (a) VSWR and (b) boresight gain comparison for the ridge gap parametric study.

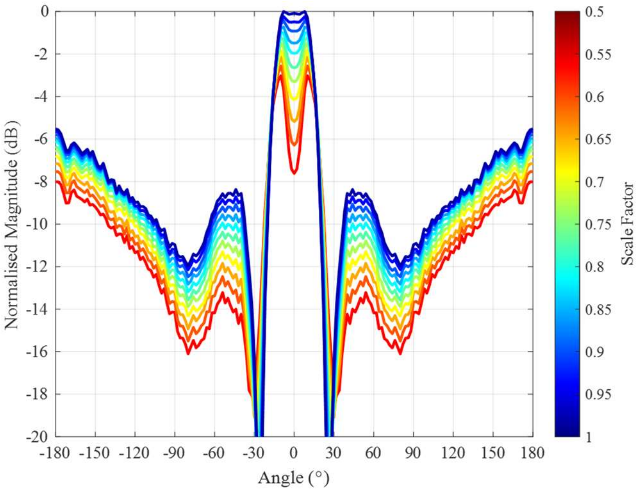

Figure 4.24. Comparison of the *H*-plane patterns at 31.5 GHz for the ridge gap parametric study.

Next, the ridge width was investigated - note that the feed pin and feed outer conductor size are related to the ridge width as the ridge width must be larger than the outer conductor by some margin to accommodate the feed. For practical implementation, the ridge width should be 1 mm larger than the outer conductor diameter for a minimum wall thickness of 0.5 mm for the outer conductor. A feed pin diameter of 0.51 mm and an outer conductor diameter of 0.9 mm were used, for an impedance of 34 Ω at the feed point. Figure 4.25(a) shows the VSWR and Figure 4.25(b) the boresight gain for a scale factor from 1 to 0.5 in 0.05 increments for the ridge starting width. Reducing the ridge starting width significantly improved the VSWR and gain above 24 GHz although between 2 and 24 GHz the VSWR degrades slightly indicating that the ridge impedance over this frequency range does vary slightly.

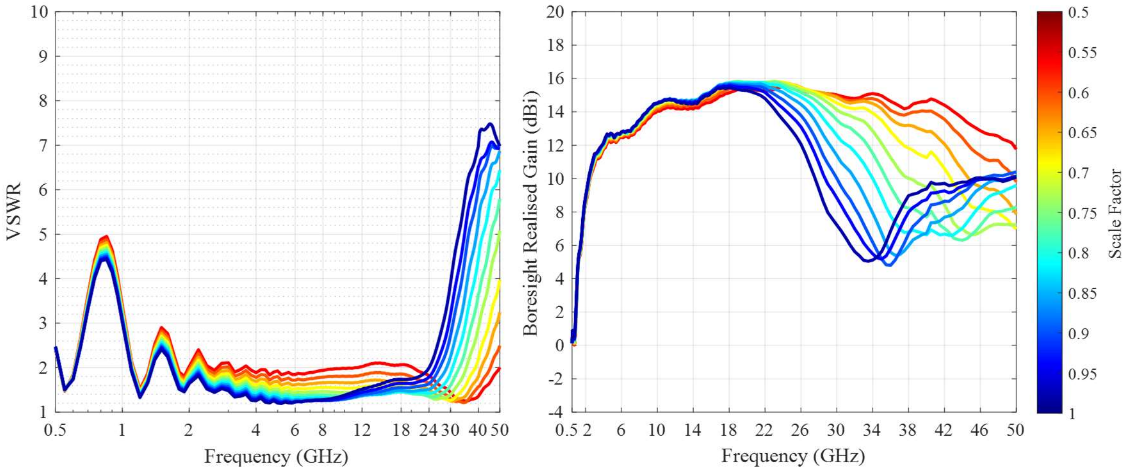

(a) (b)

Figure 4.25. (a) VSWR and (b) boresight gain comparison for the ridge width parametric study.

In the next step the ridge gap, starting ridge width, and feed parameters (feed pin and outer conductor diameter) were all scaled together, starting with the model used in the ridge gap investigation and using a scale factor from 1 to 0.5 in 0.05 increments. Figure 4.26(a) and Figure 4.26(b) show a significant improvement in the VSWR and gain above 24 GHz. Interestingly the VSWR below 24 GHz showed nearly no effect which indicates that scaling the ridge width and ridge gap together, i.e. keeping the ratio of ridge gap to width constant, keeps the characteristic ridge impedance constant over most of the frequency range. It was found that a scale factor of 0.5 or less resulted in a 3D radiation pattern with a well-formed main beam over the full frequency range.

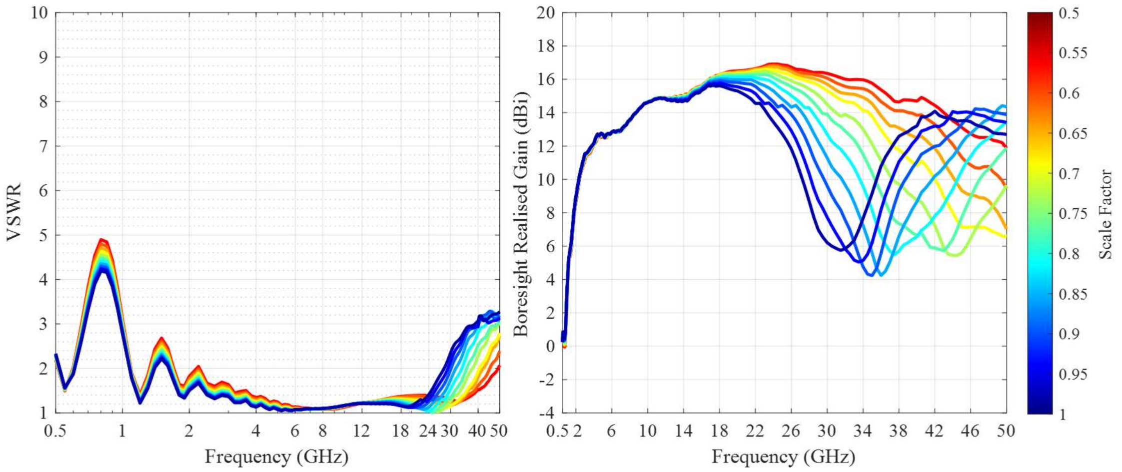

(a) (b)

Figure 4.26. (a) VSWR and (b) boresight gain comparison for the combined ridge gap and width parametric study.

In summary, Figure 4.23(a) and Figure 4.23(b) show that the gain dip at 32 GHz becomes deeper and the VSWR especially below 2 GHz and above 24 GHz degrades if the ridge gap is reduced and the ridge width is kept constant. Figure 4.25(a) and Figure 4.25(b) show that reducing the ridge width in isolation removes the dip in the gain at 32 GHz and improves the VSWR above 24 GHz, but the VSWR between 2 and 24 GHz increases. Figure 4.26(a) and Figure 4.26(b) show that by decreasing both the ridge gap and width the gain performance improves, the VSWR below 2 GHz and above 24 GHz remains the same, and the VSWR performance between 2 and 24 GHz improves significantly.

These parametric studies show that by finding the optimal values of the ridge gap and width the VSWR and gain performance of the DRGH can be improved significantly in the mmW band without a dramatic effect on the performance below 18 GHz.

4.3.6 Summary

The results of the investigation in this section indicate that redesigning the coaxial feed, coax-to-waveguide launcher and ridges is needed to extend the DRGH upper-frequency limit in the mmW band and thus increase the bandwidth. Changes to the sidewall design are also necessary to ensure good performance in the mmW band since it was found that the sidewalls influence the radiation pattern performance at the high-frequency end with the dielectric substrate of the *E*-plane sidewalls causing significant degradation.

4.4 ELECTRICAL DESIGN AND SIMULATION

In this section, the knowledge gained from the previous section is used to design the 0.5-50 GHz DRGH. Extensive use was made of experimentation using the EM models from the previous section as shown in Section 4.4.1. The final models and simulation results are presented in Section 4.4.2.

4.4.1 EM Experimental Design

As a first step, the coaxial feeding assembly was designed. For operation up to 50 GHz, it would be necessary to make use of a 2.4 mm connector. A typical pin diameter that can be used with these connectors is 0.51 mm, thus the feed pin diameter was set to 0.51 mm. For this design, it was decided to keep the feed pin constant and taper the outer conductor i.e. the hole in the top ridge since it would be easy to obtain a constant, standard diameter, brass rod for a feed pin in this size. Also, it was already envisaged that the feed assembly would be 3D printed and thus it was anticipated that printing the tapered outer conductor should be straightforward.

The outer conductor was tapered from a diameter of 1.2 mm at the connector end (approximately 51 Ω) to 0.9 mm (approximately 34 Ω) at the feed point. This resulted in a minimum cut-off frequency of 111 GHz. Due to the small sizes, it would be harder to manufacture a taper of the same length as on the 0.5-18 GHz DRGH, especially when extending it beyond the coax-to-waveguide launcher cavity. Thus, the taper length was restricted to approximately half of the 0.5-18 GHz DRGH *E*-plane cavity dimension (30 mm). Although the 0.5-50 GHz coax-to-waveguide launcher was not designed yet, it was expected that the cavity size would have to be at least the same size as the 0.5-18 GHz design to allow operation down to 0.5 GHz.

The ridge design was based on the parametric studies done on the ridge gap and ridge width in Section 4.3.5. Scaling the ridge width of the 0.5-18 GHz DRGH at the feed (4.7 mm) by 0.5 would result in a ridge width of 2.35 which was rounded to the nearest half mm (2.5 mm). Scaling the ridge gap of the 0.5-18 GHz DRGH at the feed (0.7 mm) by 0.5 would result in a ridge gap of 0.35 which was rounded to the nearest 0.1 mm (0.4 mm). The straight section of ridge along the axial length of the horn from the feed point was 3.3 mm in the 0.5-18 GHz design, scaling this by 0.5 would result in a length of 1.65 mm, but this was reduced slightly to 1.25 mm. The ridge was extended in the opposite direction until the wall thickness of the coaxial feed was at least 0.5 mm since thinner walls would become difficult to manufacture. The back end of the ridge was left square for simplicity's sake.

The ridge profile was again implemented using a Bezier curve with the parameters optimised so that the profile would transition smoothly into the 0.5-18 GHz DRGH ridge profile despite having different starting parameters, for example, the ridge gap, see Table 4.1. The FEKO model of this design is shown in Figure 4.27.

Table 4.1. Cubic Bezier control points of the final ridge profile (in mm)

Bezier point	Description	Axial distance (X)	Perpendicular distance (Z)
P0	Start point	1.25	0.2
P1	Start tangent point	225.32	0.2
P3	End tangent point	192.99	75.99
P4	End point	193	76

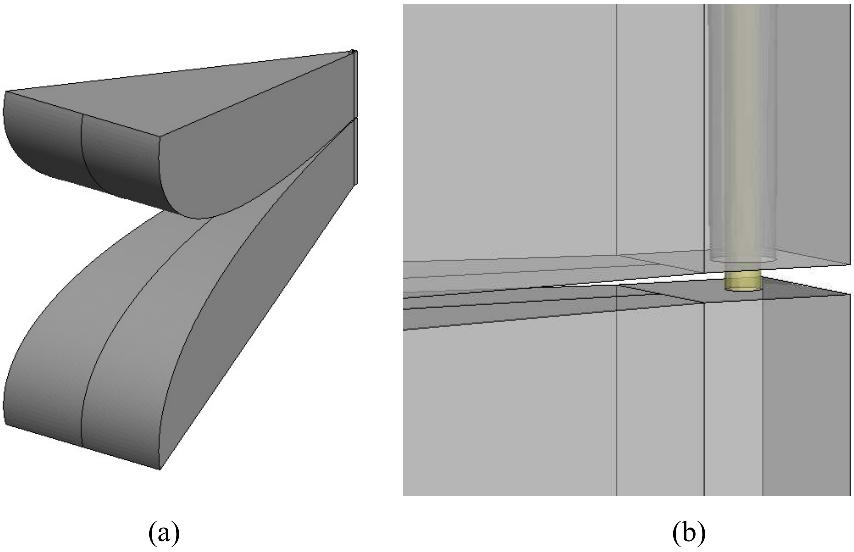

Figure 4.27. (a) FEKO model starting ridge design and (b) close-up view of the feed assembly.

Figure 4.28(a) show the simulated VSWR and Figure 4.28(b) the boresight gain for the model in Figure 4.27. The VSWR and gain performance below 2 GHz is poor, but it was expected that this would improve significantly when adding the sidewalls as was seen in Chapter 3. The design has good VSWR and gain performance from 2 GHz to 42 GHz, but above 42 GHz the VSWR goes above 2:1 and the gain drops down to 11 dBi.

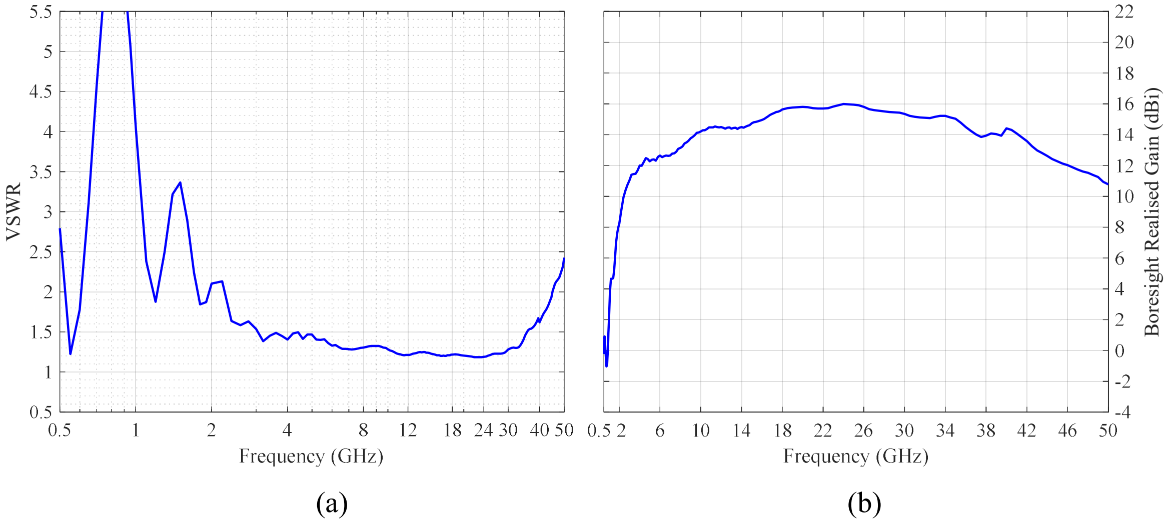

Figure 4.28. (a) VSWR and (b) boresight gain comparison for the initial ridge design.

For the physical implementation of the horn, the antenna needs a structure to which the top and bottom ridges can be connected. This function is performed by the coax-to-waveguide launcher which also ensures that the energy entering the horn through the connector and down the coaxial impedance transformer is guided along the ridges in the boresight direction. Effectively the cavity or coax-to-waveguide launcher acts as a balun.

Vivaldi antennas can be considered a 2D implementation of the 3D ridges in a DRGH. A structure similar to the balun of a conventional Vivaldi antenna, shown in Figure 4.29 was thus investigated. Parametric studies were performed to determine the diameter of the slot line open or circular cavity as well as the distance between the circular cavity and coaxial feedline. Figure 4.30 and Figure 4.31 show the results for these parametric sweeps. It was found that decreasing the circular cavity diameter initially improves the low-frequency VSWR performance, specifically the peaks at 0.5 and 0.85 GHz, and then quickly degrades it beyond 16 mm. Increasing the distance between the circular cavity and the feedline deteriorates the high-frequency performance. For the current design, it was decided to use a cavity diameter of 16 mm, positioned as close as possible to the feedline.

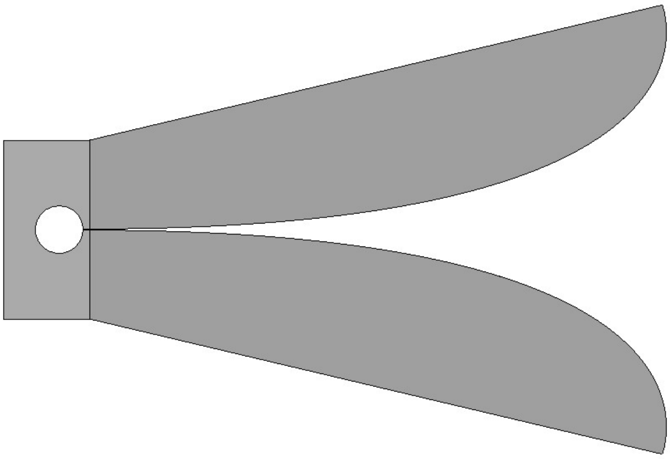

Figure 4.29. Ridges with Vivaldi feeding structure/circular cavity.

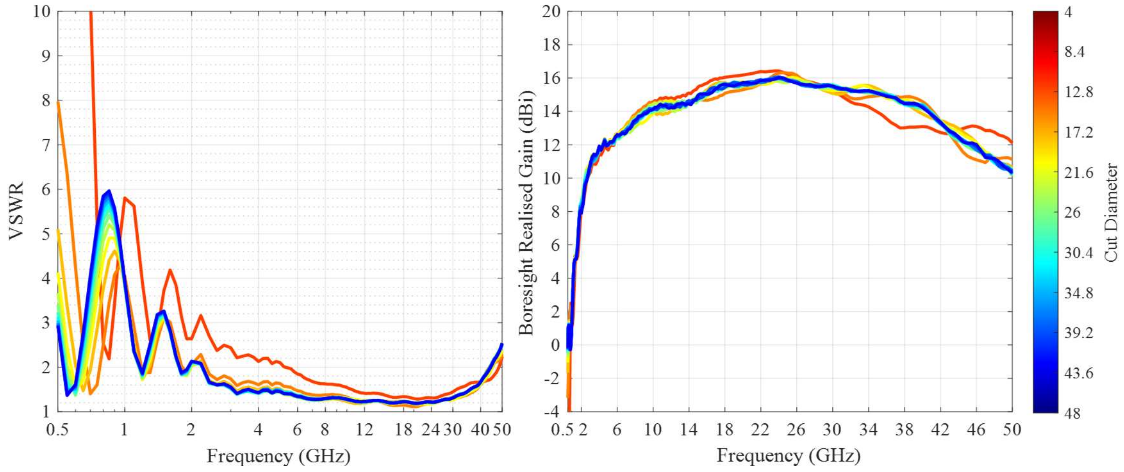

(a) (b)

Figure 4.30. (a) VSWR and (b) boresight gain performance for different circular cavity dimensions.

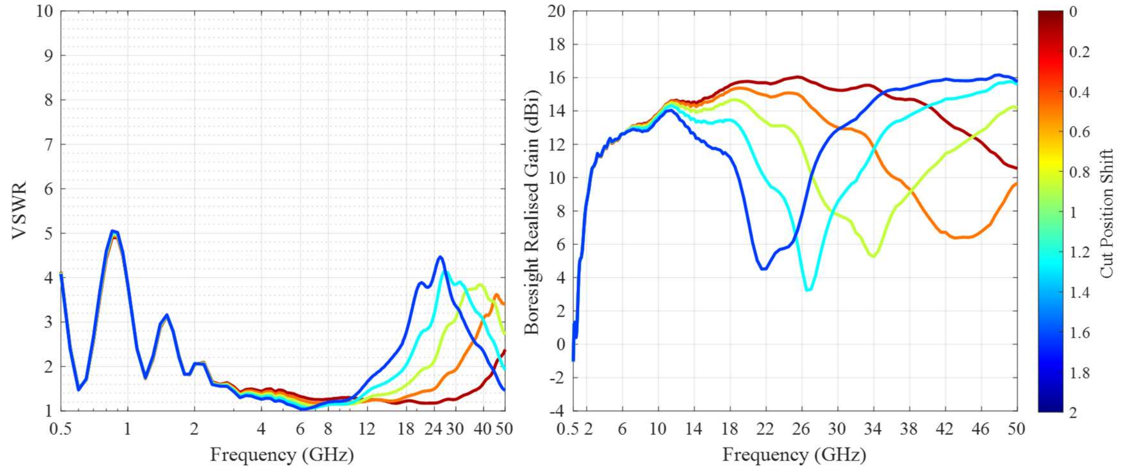

(a) (b)

Figure 4.31. (a) VSWR and (b) boresight gain performance for different distances between the circular cavity (16 mm diameter) and feed point.

This coax-to-waveguide launcher improved the impedance performance but there was still significant radiation backwards and to the sides, see Figure 4.32. It was, however, decided to first perform the flared waveguide design before the experimental design of a cavity surrounding the coax-to-waveguide launcher.

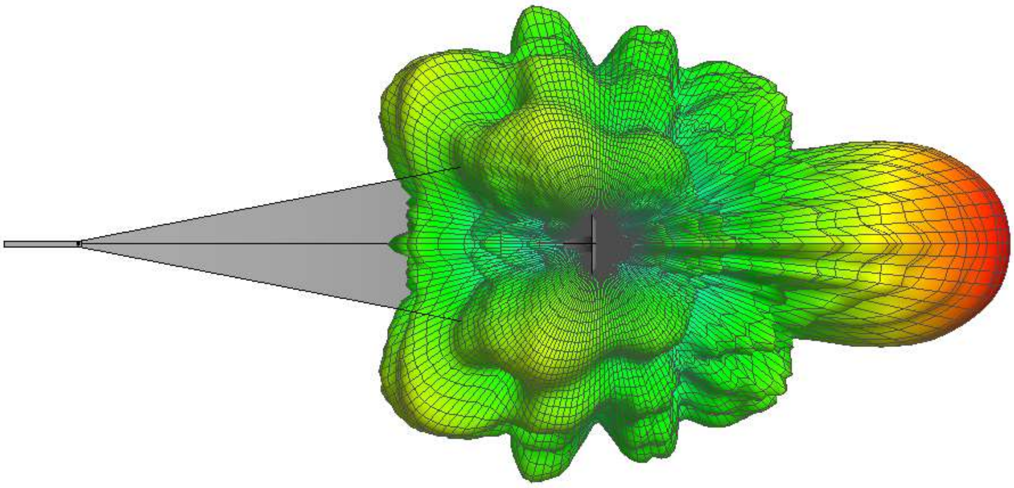

Figure 4.32. Radiation pattern at 40 GHz showing side and back lobes.

The *E*-plane sidewall electrical design was implemented as thin grids without any dielectric supports with a strip width of 1 mm and a strip gap of 60 mm (λ/10 at 0.5 GHz). Except for the removal of the dielectric substrate, this is the same design as for the 0.5-18 GHz DRGH. The *E*- and *H*-plane aperture dimensions were kept the same as in the 0.5-18 GHz DRGH design, i.e. 264×152 mm and the same for the other end of the flared waveguide at the launcher interface, i.e. 80×60 mm.

The flared waveguide axial length was increased slightly (194.55 mm) so that the starting point of the flare would align with that of the ridge Bezier curve. Figure 4.33 shows the FEKO model for this design. Figure 4.34(a) and Figure 4.34(b) show the VSWR and gain result comparison of the FEKO model with and without sidewalls. The addition of the sidewalls, as expected, significantly improves the VSWR and gain below 2 GHz, but does introduce some ripple in gain at higher frequencies. These gain ripples are most probably caused by the side lobes, similar to that shown in Figure 4.32 reflecting from the sidewalls, comparing Figure 4.32 to Figure 4.35.

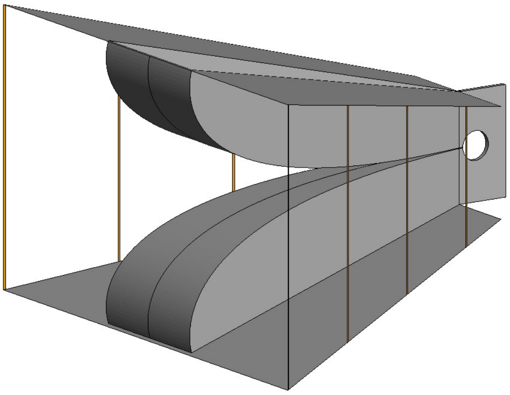

Figure 4.33. Ridges with Vivaldi feeding structure/circular cavity and sidewalls.

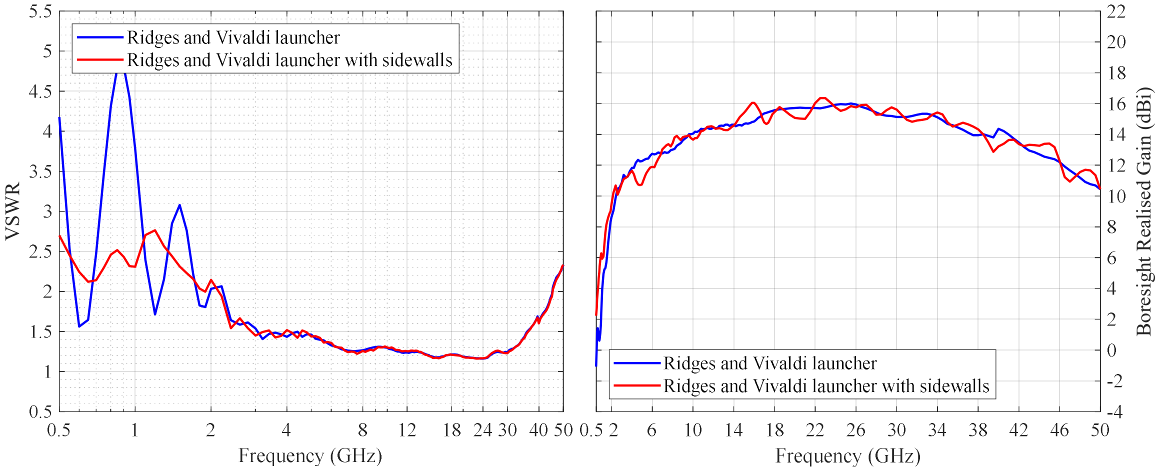

(a) (b)

Figure 4.34. (a) VSWR and (b) boresight gain comparison with and without sidewalls.

This coax-to-waveguide launcher improved the impedance performance but there was still significant radiation backwards and to the sides. Since the 2.4 mm connector already limits the power handling capability of the DRGH, an absorber-filled cavity similar to that used on spiral antennas [89] to suppress the backward radiation was added to the Vivaldi structure. The box for the absorber-filled cavity has the same width and height as the waveguide to launcher interface i.e. 80×60 mm. The depth of the cavity was chosen as 31 mm so that the top of a 0.75-inch absorber would nominally coincide with the centre of the circular cavity.

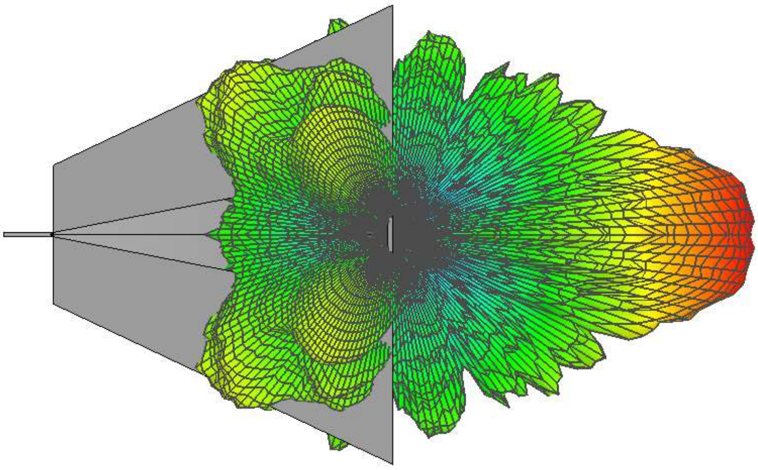

Figure 4.35. Radiation pattern at 40 GHz showing side and back lobes after sidewalls added.

The absorber can either be of the foam type for example Eccosorb AN-74 or honeycomb which would be better for higher power handling. Similar to [89] a honeycomb absorber with hexagonal cells was used in the simulation model. The honeycomb structure was created using a dielectric material coated with a resistive material and graded with an increase towards the bottom of the cavity to maximise absorption, see Figure 4.36.

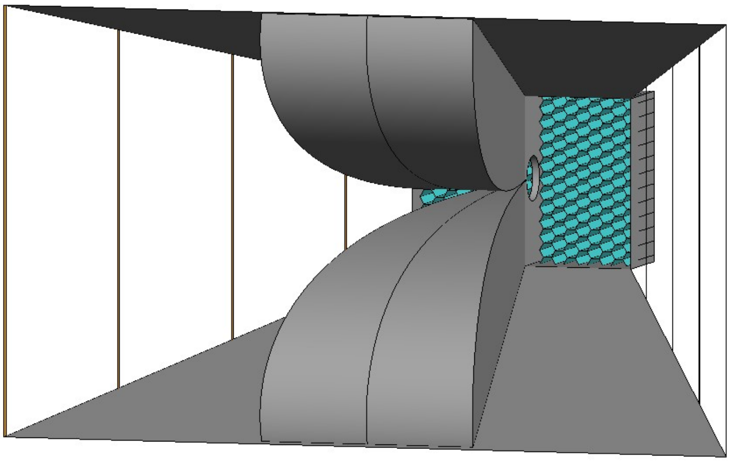

Figure 4.36. FEKO model with absorber filled box.

Figure 4.37 shows the simulated results for the FEKO model of Figure 4.36. As seen in Figure 4.37(a) the VSWR improves slightly below 1 GHz while as seen in Figure 4.37(b) the gain ripple peaks increase slightly at higher frequencies. This is most probably due to additional reflection from the cavity. The back lobes are, however, reduced significantly, see for example Figure 4.38.

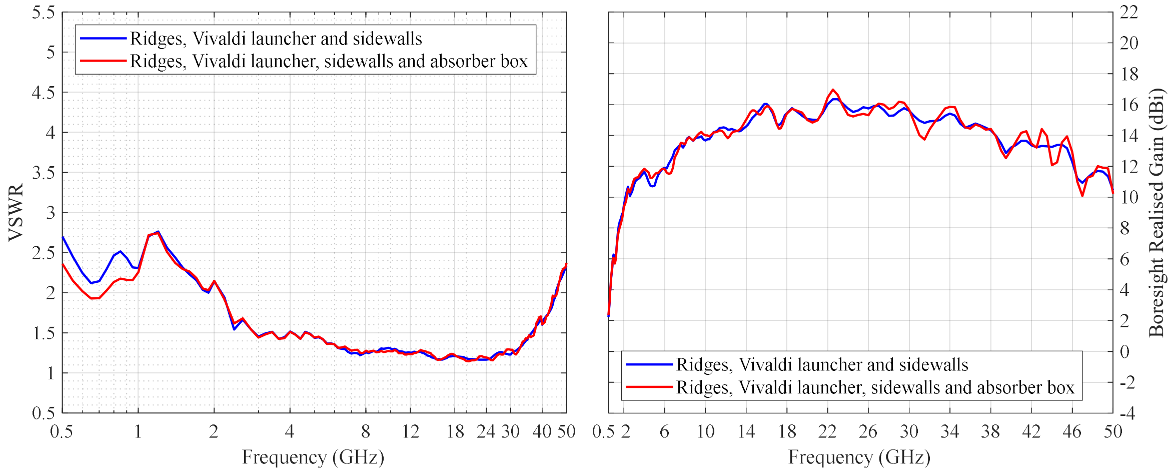

(a) (b)

Figure 4.37. (a) VSWR and (b) boresight gain comparison with and without absorber box.

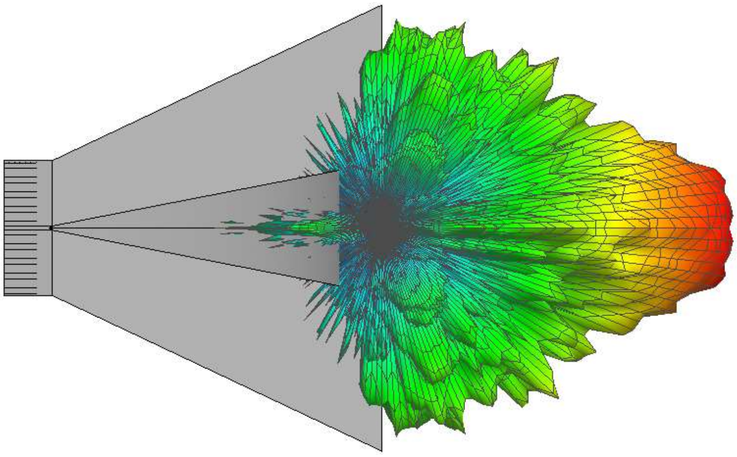

Figure 4.38. Radiation pattern at 40 GHz showing side and back lobes with absorber box added.

These results were very close to the required performance. Some desirable improvements identified were a reduction of the VSWR to less than 2:1 below 2 GHz and above 44 GHz and an improvement of the gain above 38 GHz to be above 14 dBi.

4.4.2 Final Simulation Model and Results

At this stage it was suspected that the ridge gap and width had to be reduced further in order to improve the high frequency performance, but a way had to be found to do this without sacrificing low frequency performance. The hypothesis was that if this could be done for only a portion of the ridge it would be possible. After further experimentation using the last FEKO model as a starting point it was found that adding a smaller sub-ridge inside the main ridge, as well as applying three separate main ridge width tapers improved the high-frequency gain and low-frequency VSWR performance, see Figure 4.39(a) and Figure 4.39(b). The implementation of the sub-ridge and separate main ridge width tapers are shown in Figure 4.40 (a) to Figure 4.40 (d).

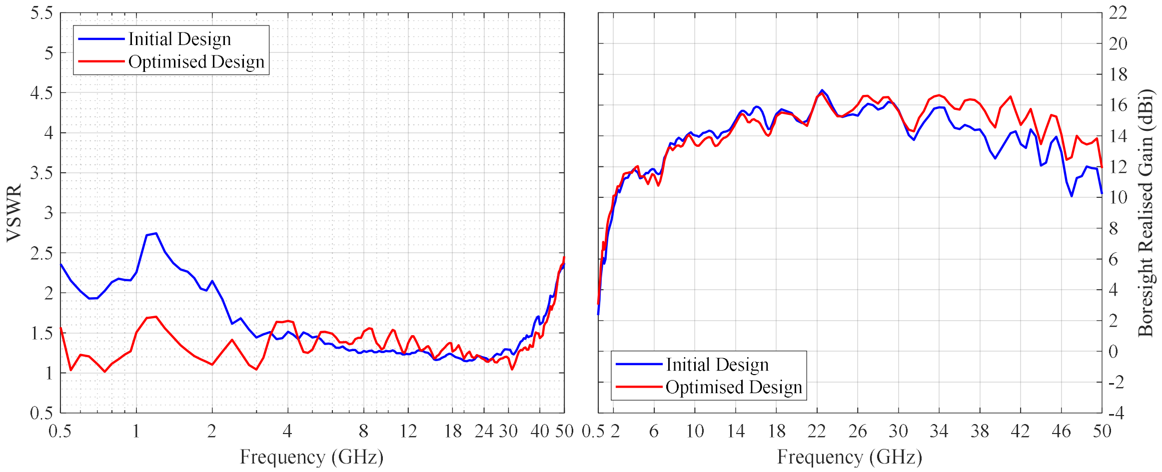

(a) (b)

Figure 4.39. (a) Simulated VSWR and (b) boresight gain comparison between the initial and optimised 0.5-18 GHz DRGH design.

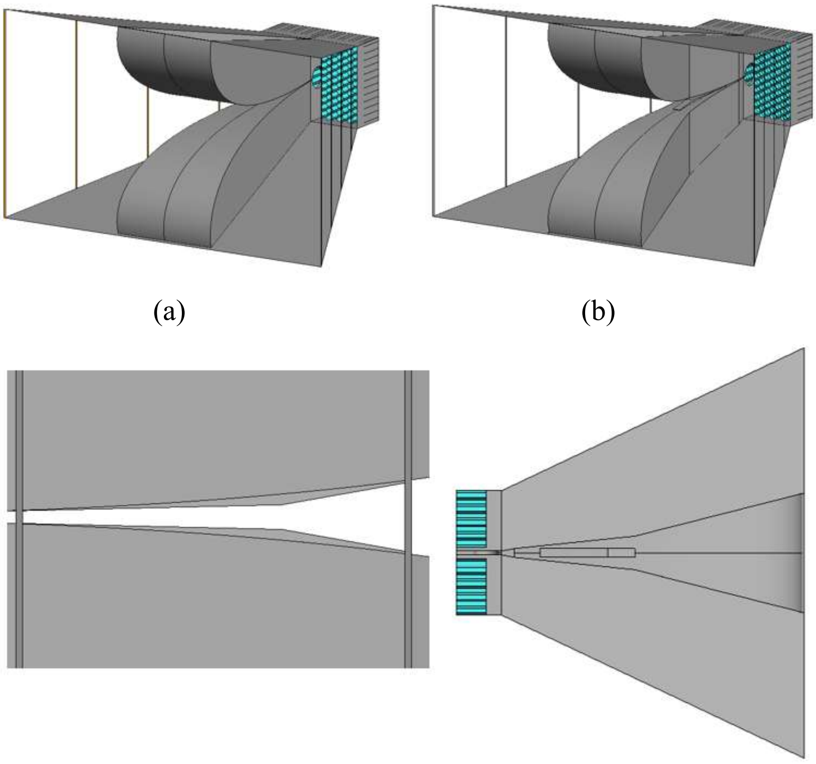

(a) (b)

(c) (d)

Figure 4.40. (a) Initial and (b) optimised FEKO model for 0.5-50 GHz DRGH with (c) side view of sub-ridge and (d) cut view showing the sub-ridge and stepped tapers of the main ridge.

The width of the sub-ridge is 6.5 mm. It starts where the main ridge gap is 1.45 mm. The first section of the sub-ridge is a linear taper at an angle of 1.3° with the horn axis. The second section of the sub-ridge starts where the sub-ridge gap is 3.43 mm, it also has a linear taper, but at an angle of 11° with the horn axis. Linear tapers for the main ridge width were implemented as follows: The first section with a taper angle of 11° with the horn axis until the ridge width is 5.61 mm. The second section with a taper angle of 5.88° until the ridge width is 21.61 mm and the final section with a taper angle of 14.26° for the rest of the ridge.

At this stage the design was good enough so that a prototype could be manufactured to verify the simulated results and for use in further experimental investigations and optimisation.

4.5 PROTOTYPE DESIGN AND MANUFACTURE

The practical model was created from the FEKO EM simulation model by replacing infinitely thin faces with parts having finite thickness. The *E*-plane sidewall grid strip width was eventually increased to 3 mm since 1 mm turned out not to be sturdy enough. The model was split into various parts and or sub-assemblies i.e. the ridges, *E*- and *H*-plane sidewalls, cavity, and feed section. Detail was also added to the various parts, e.g. holes for fasteners with the hole sizes determined from standard tables to allow tapping and fitment of helicoil thread inserts. Most of the parts were designed to be manufactured using additive manufacturing, the method of choice for rapid manufacturing of low-cost parts and prototypes. Figure 4.41 shows the final mechanical design of the antenna.

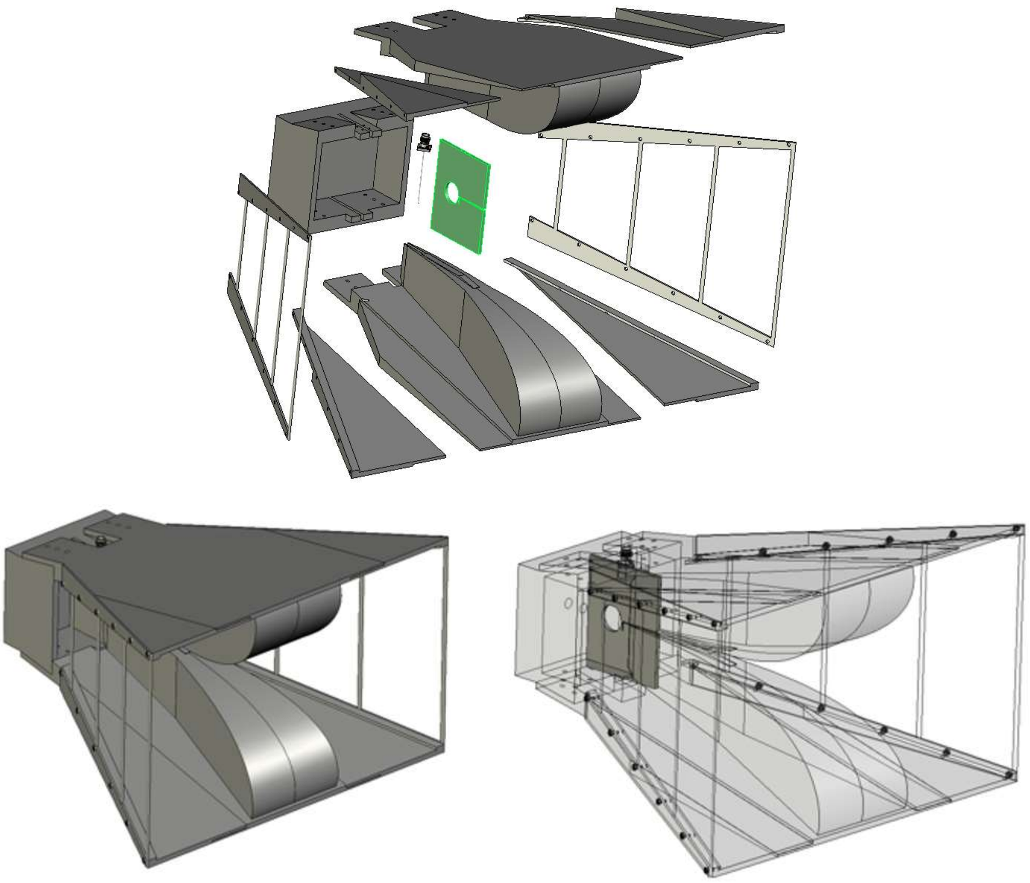

Figure 4.41. Mechanical design of the 0.5-50 GHz DRGH.

The parts not manufactured using additive manufacturing were the Southwest Microwave model 1412-04SF 2.40 Jack (F) .375” square flange connector, the feed pin consisting of a 0.5 mm brass rod and various Stainless Steel (SS) 316 fasteners and helicoil thread inserts. The design of the different parts was performed keeping in mind practical considerations for additive manufacture, such as the size of the parts, alignment on the print bed, support requirements, etc. As an example, the ridges were combined with the *H*-plane sidewalls but had to be split into three sections since the corners did not fit on the print bed.

STL files were exported from the mesh created in FEKO and imported into the slicer software used by the various printers utilised, see for example Figure 4.42. Here detail such as layer height, wall thicknesses, fill factor, etc. was set up as required.

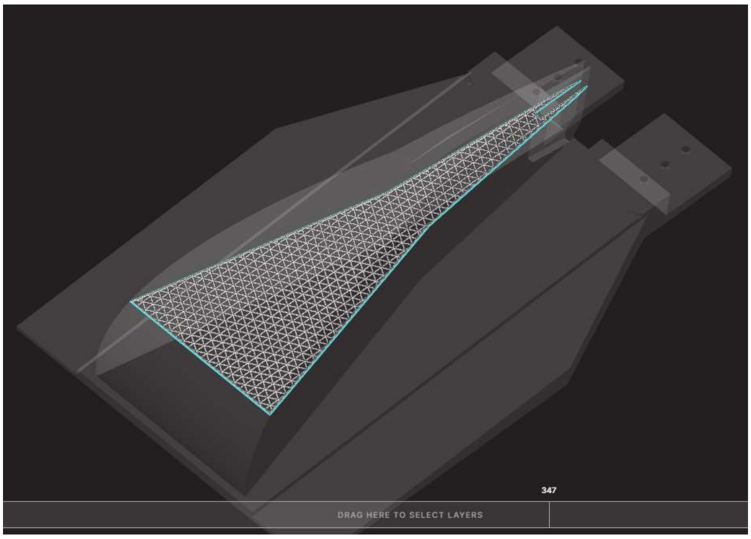

Figure 4.42. View in Eiger slicer (from Markforged) of one of the ridge sections.

Apart from the feed section highlighted in green in Figure 4.41, all of the parts were printed in plastic and metallised using silver conductive spray (842AR from MG Chemicals), see for example Figure 4.43.

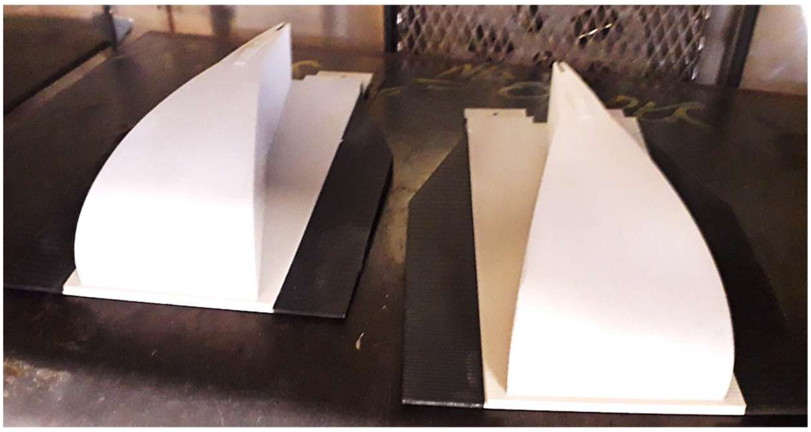

Figure 4.43. Ridges in oven after application of silver conductive spray.

The various parts were manufactured as follows: The *E*-plane grids were printed on a VSHAPER in PC-ABS, coated with silver conductive spray. The *H*-plane flares, ridges, and cavity were printed on a Markforged Mark Two in Onyx, coated with silver conductive spray. Due to the extremely small sizes of the feed section FDM printing in plastic would not be suitable for this part and the feed section was therefore printed using DMLS on an EOS M290 in SS316.

The feed pin was first soldered onto the bottom ridge of the feed section after etching the solder point. The connector was then mounted onto the feed section with the pin sliding into the connector collet. At this stage the feed section could be measured on its own, see Figure 4.44 (a). The absorber was cut to size and glued into the cavity with attention given to the orientation i.e. ensuring the side least loaded was nearest to the feed point. The feed section was then inserted into the absorber-filled cavity of the coax-to-waveguide launcher, see Figure 4.44 (b).

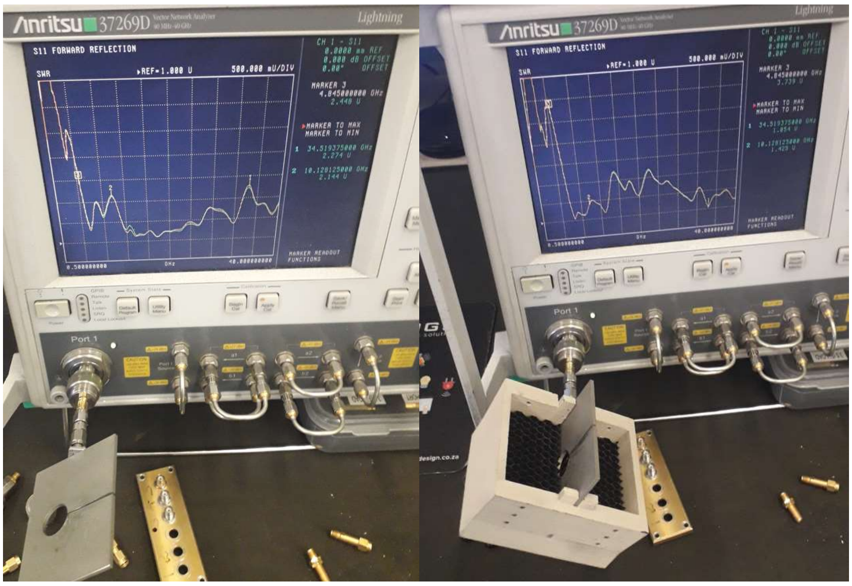

(a) (b)

Figure 4.44. (a) Feed section and (b) feed section with absorber filled coax-to-waveguide launcher cavity VSWR tests.

The rest of the parts were assembled using fasteners and helicoil thread inserts placed in the holes of the printed parts after tapping. During assembly of the coax-to-waveguide launcher to the ridges, silver conductive epoxy (EPO-TEK H20E) was used to glue the ridges to the feed section, see Figure 4.45.

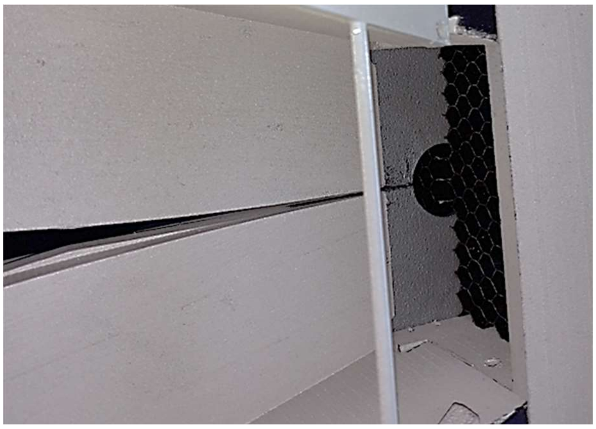

Figure 4.45. Close-up view of coax-to-waveguide launcher and flared waveguide interface.

4.5.1 Prototype Manufacture Design Modifications

The initial measured VSWR result was very poor, and it was determined that the printing tolerances inside the feed section, specifically the coaxial impedance taper, were not good enough. There were obstructions inside the hole that caused the feed pin to short-circuit upon final assembly. To solve this problem the hole was drilled to a constant diameter of 1.2 mm. Several experiments were conducted, and it was found that the remaining ripple is due to weak reflections from the cavity edges not covered by the absorber as well as the thin sidewall strips. A foam absorber (Eccosorb LS26) was placed on the uncovered cavity edges and the grid sidewall strips were painted using a carbon conductive paint (Yshield NSF34). These changes slightly improved the VSWR, gain, and pattern ripple. Photos of the final prototype are shown in Figure 4.46 and the measured results are presented in the next section.

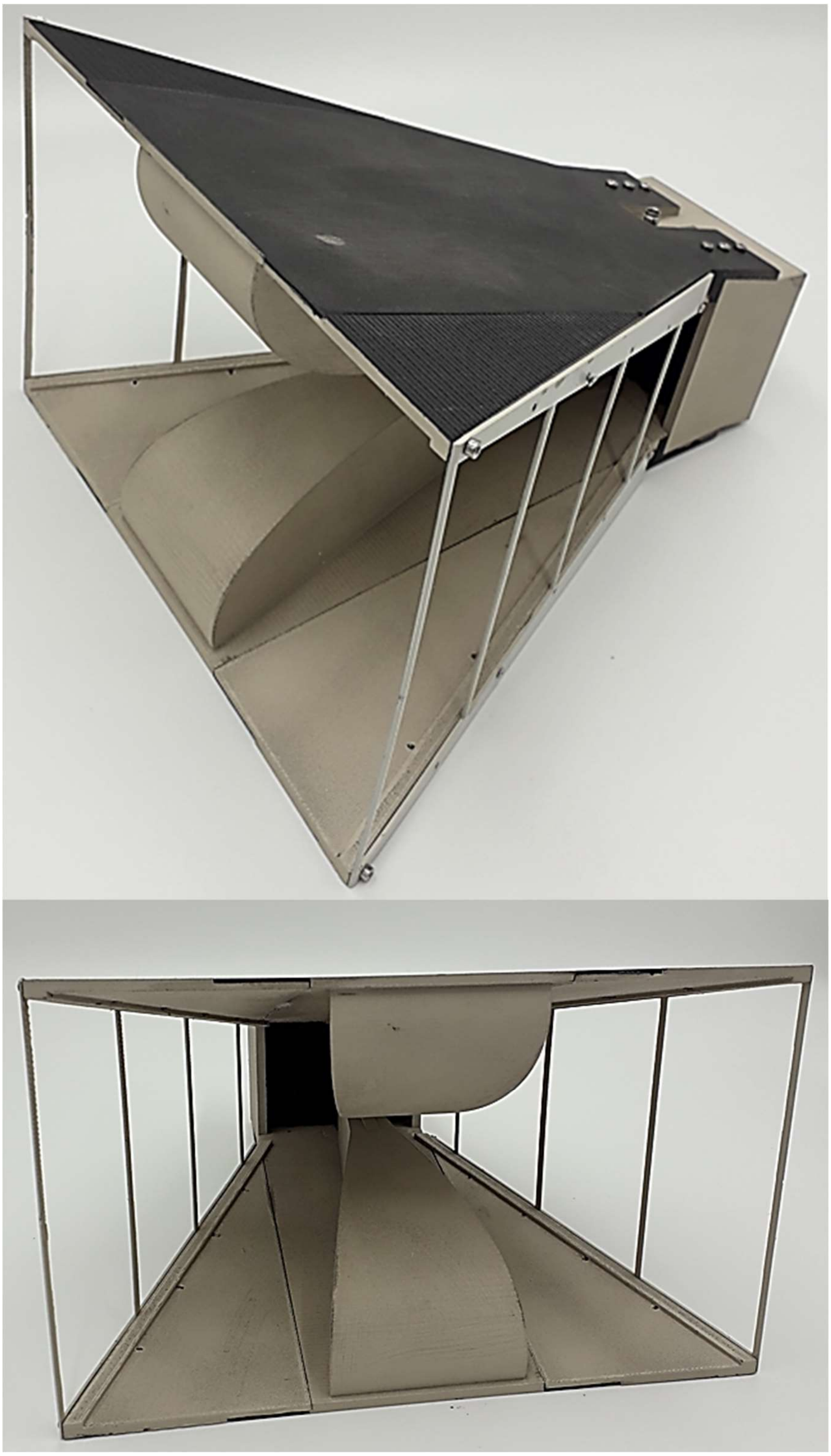

Figure 4.46. Final prototype of the 0.5-50 GHz DRGH.

4.6 MEASURED RESULTS

The VSWR of the prototype antenna was measured in 801 points from 0.5-50 GHz using a VNA while gain and pattern measurements were performed in both tapered and rectangular anechoic chambers. To cover the full 0.5-50 GHz band three different setups were used. The first two setups in a tapered anechoic chamber were similar to that used to measure the 0.5-18 GHz DRGH, see Figure 4.47(a). An additional setup was used in a rectangular chamber to measure 18-50 GHz in 250 MHz steps for both gain and pattern measurements, Figure 4.47(b). Several measured *E*- and *H*-plane radiation patterns are shown in Figure 4.48 and Figure 4.49.

(a) (b)

Figure 4.47. (a) Tapered and (b) rectangular anechoic chamber measurement setups.

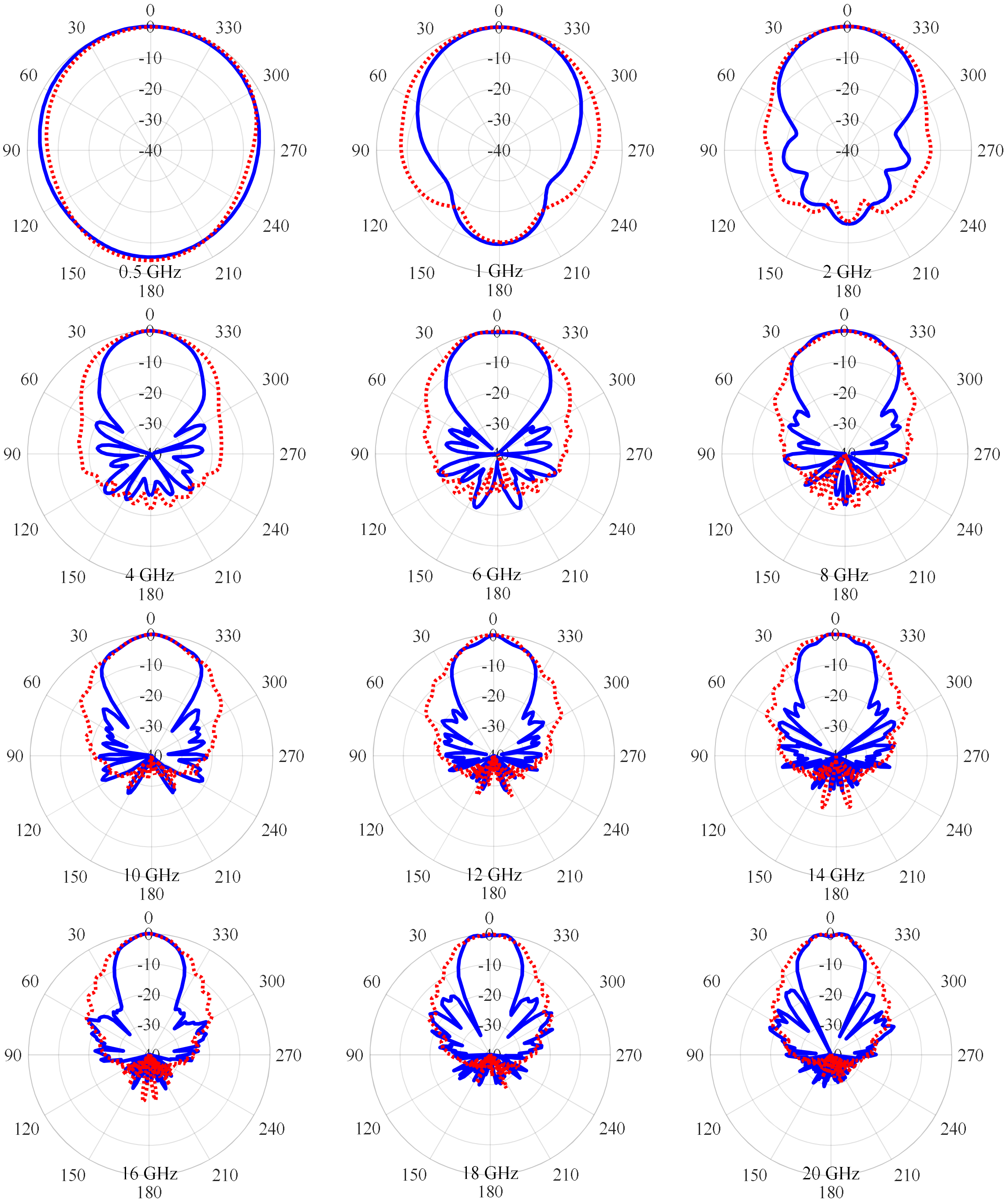

Figure 4.48. Measured co-polarised radiation patterns from 0.5 to 20 GHz of the 0.5–50 GHz DRGH.

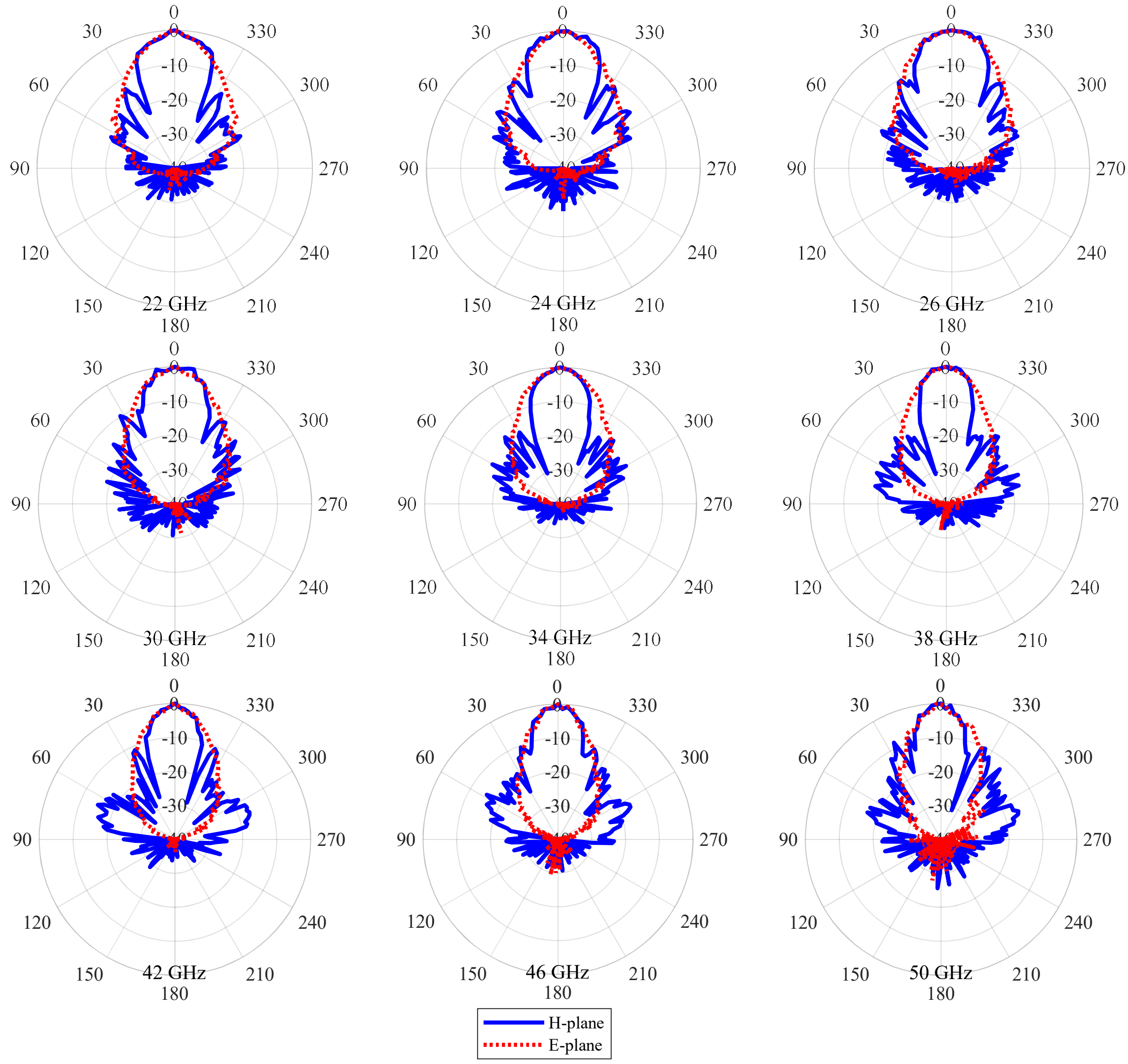

Figure 4.49. Measured co-polarised radiation patterns from 22 to 50 GHz of the 0.5–50 GHz DRGH.

4.6.1 Comparison to Simulated Results

The FEKO model of Section 4.4.2 was updated based on the physical implementation and design modifications as discussed in Section 4.5 as follows; the conductivities of various sections of the simulation model were updated with the properties of the materials used in the prototype i.e. conductive paint, SS316 for the feed, and brass for the feed pin. The actual final thickness of several parts and sub-assemblies were added to the model where deemed necessary. The accuracy of the feed model was improved by the addition of a numerical model for the 2.4 mm connector and the implementation of the modification of the feed outer conductor to a constant 1.2 mm diameter which was required due to manufacturing tolerances. The foam absorber on the cavity edges and carbon paint on the sidewall strips were also added. Figure 4.50 shows the final FEKO model.

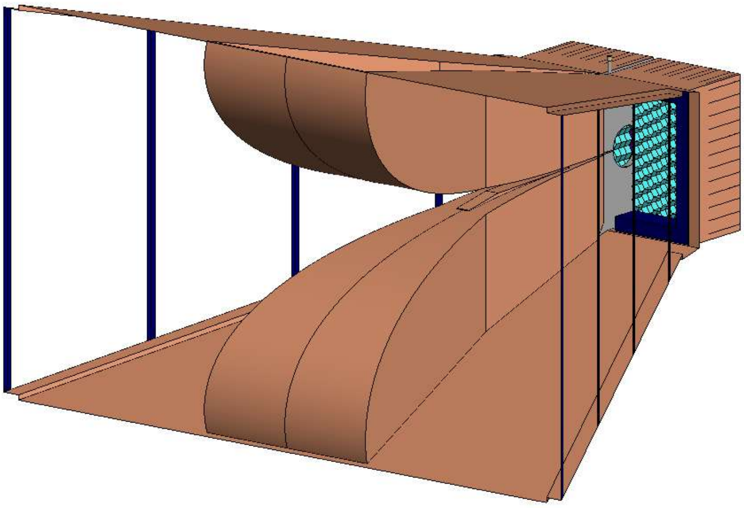

Figure 4.50. Final FEKO model of the 0.5-50 GHz DRGH design.

The comparison between measured and simulated VSWR and boresight gain is shown in Figure 4.51(a) and Figure 4.51(b), respectively. The maximum measured VSWR is 2.03:1. The deviations between measured and simulated results can be attributed to manufacturing tolerances, especially since printed silver-plated parts were used for which the manufacturing tolerances are significantly worse when compared to machined parts. There is also good comparison between the measured and simulated gain. The gain does have some ripple due to ripples in the main beam pattern, but no pattern breakup was observed in either the measured or the simulated results. The measured cross-polar discrimination, shown in Figure 4.52, is typically better than 30 dB with the worst-case values between 27 and 28 dB around 0.5 GHz, 7.3 GHz and above 42 GHz.

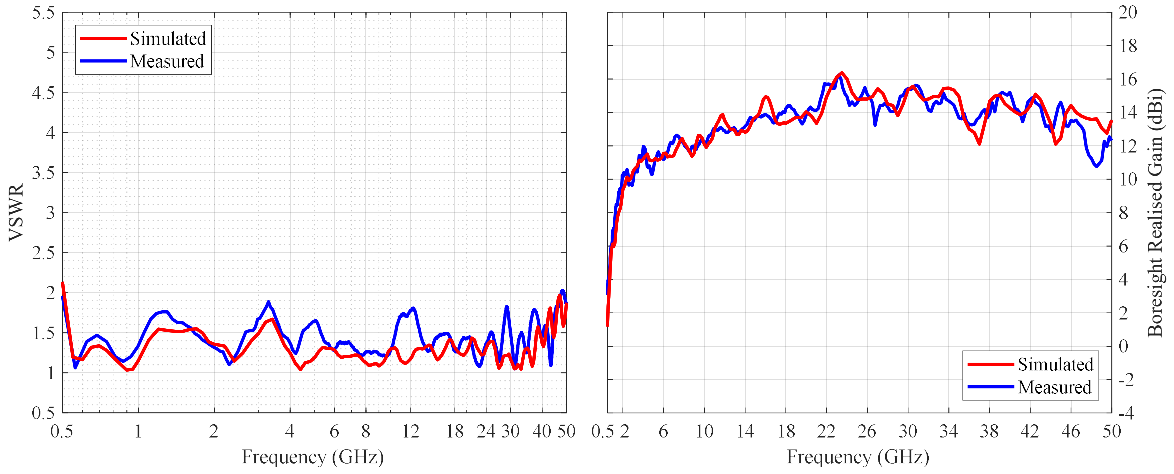

(a) (b)

Figure 4.51. (a) VSWR and (b) boresight gain comparison of final simulated and measured results for the 0.5-50 GHz DRGH.

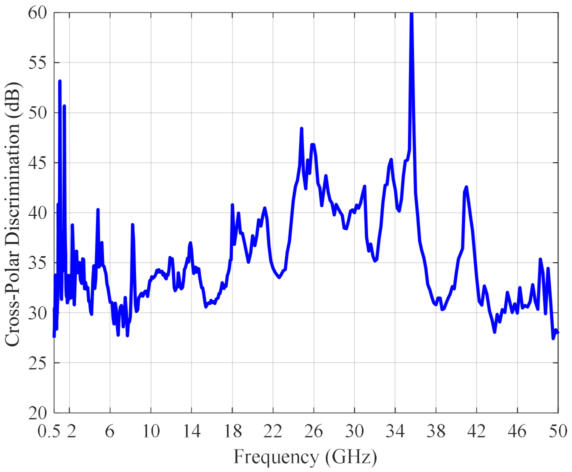

Figure 4.52. Measured boresight cross-polar discrimination of the 0.5-50 GHz DRGH.

The *E* and *H*-plane 3dB beamwidth, side and back lobes extracted from the measured results are shown in Figure 4.53(a) and Figure 4.53(b), with the simulated and measured results comparing favourably. The *E*- and *H*-plane beamwidth is nominally similar and decreases from around 60° at 2 GHz to 15° at 50 GHz. The side lobe level is typically above 15 dB between 1.5 GHz and 18 GHz and typically above 10 dB in the mmW band. The back lobe level improves from 4 dB at 0.5 GHz to 25 dB or better above 10 GHz.

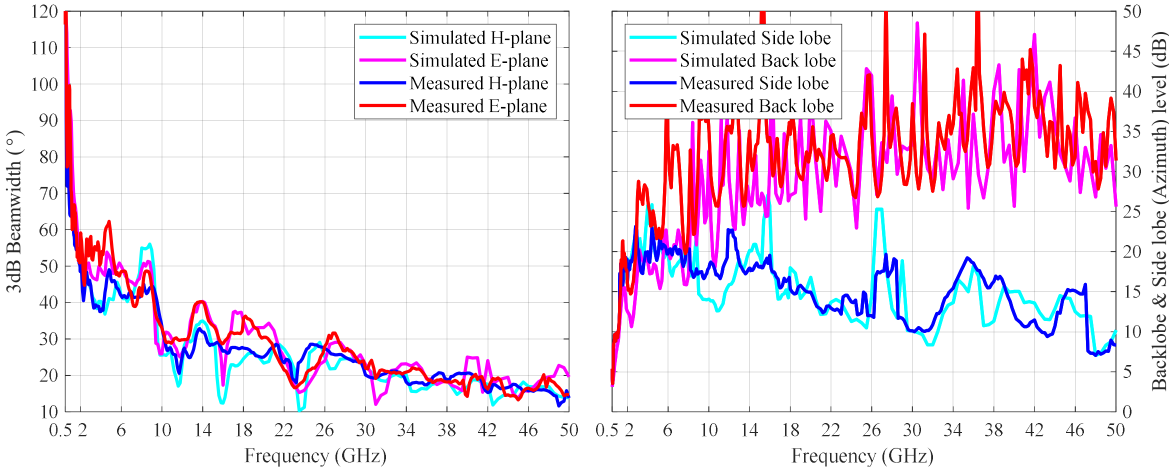

(a) (b)

Figure 4.53. (a) Beamwidth (3 dB), (b) back lobe and side lobe level comparison of the simulated and measured results for the 0.5-50 GHz DRGH.

4.6.2 Comparison to 0.5-18 GHz DRGH

This section provides a comparison between the measured results for the 0.5-18 GHz DRGH design from Chapter 3 and the 0.5-50 GHz DRGH designed in this chapter. Both the VSWR of the 0.5-18 GHz DRGH and the 0.5-50 GHz DRGH are nominally below 2:1 across the entire bandwidth of each antenna, respectively, see Figure 4.54(a). The gain is similar below 5 GHz, but between 5 GHz and 16 GHz the 0.5-18 GHz DRGH typically has 2 dB more gain, Figure 4.54(b). This is due to significant differences in the design of the ridges, the smaller ridge gap and ridge width reduces the effective radiating aperture in the 0.5-50 GHz

DRGH. In addition, the conductive spray used for the 0.5-50 GHz DRGH has significantly more loss than the aluminium parts used in the 0.5-18 GHz DRGH.

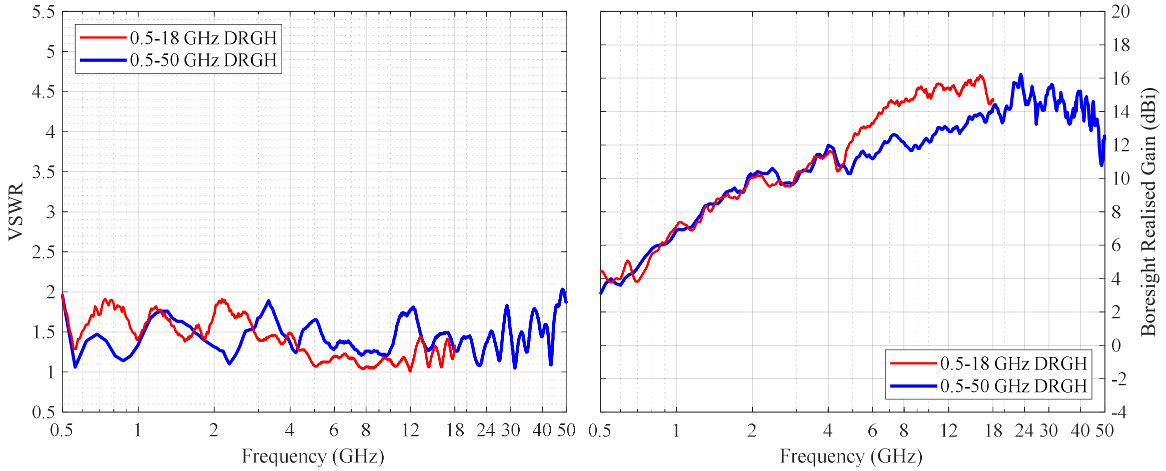

(a) (b)

Figure 4.54. (a) VSWR and (b) boresight gain comparison of the measured results for the 0.5-18 GHz vs 0.5-50 GHz DRGH.

The cross-polar discrimination (Figure 4.55), is similar below 2 GHz and above 12 GHz and in the rest of the band the 0.5-18 GHz DRGH has around 5 dB better cross-polar discrimination.

Apart from the *H*-plane beamwidth of the 0.5-18 GHz DRGH being narrower between 5 and 10 GHz, the beamwidth for both antennas is very similar, see Figure 4.56(a). The narrower *H*-plane beamwidth of the 0.5-18 GHz DRGH partially explains the higher gain of the 0.5-18 GHz DRGH above 5 GHz. The side and back lobe levels are also very similar for both antennas, see Figure 4.56(b).

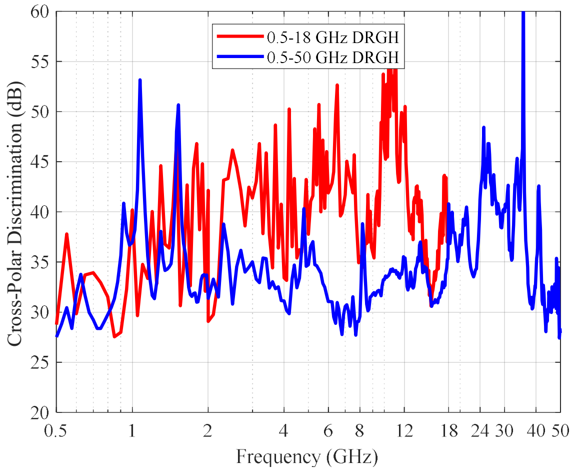

Figure 4.55. Boresight cross-polar discrimination comparison for the 0.5-18 GHz vs 0.5-50 GHz DRGH.

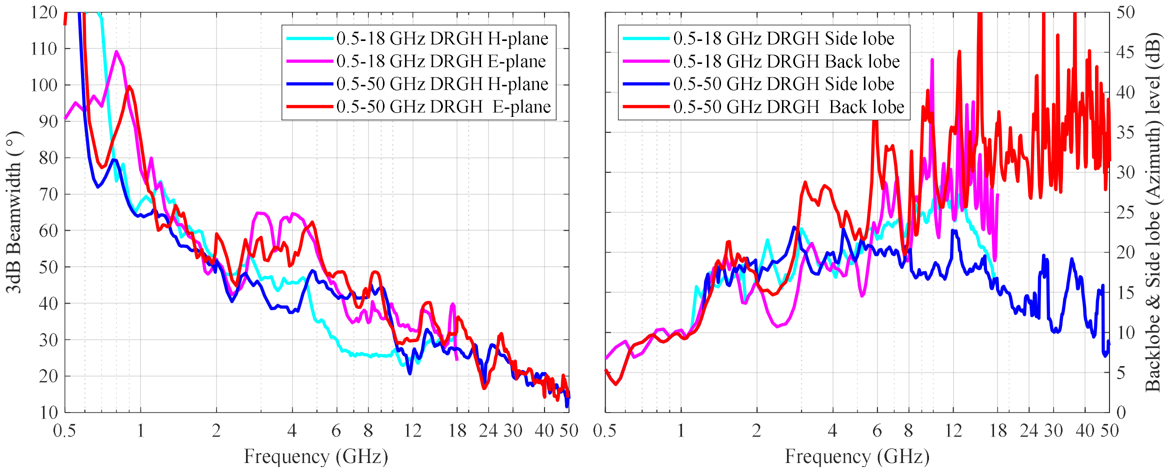

(a) (b)

Figure 4.56. (a) Beamwidth (3 dB), (b) back lobe and side lobe level comparison of the measured results for the 0.5-18 GHz vs 0.5-50 GHz DRGH.

In summary, the performance of both antennas is very similar in the overlapping band and thus the DRGH bandwidth was extended from 36:1 to 100:1 without significant performance deviations. It would, however, be desirable to improve the boresight gain and side lobes above 46 GHz by 2 dB or more.

4.6.3 Power Handling Investigation

To investigate whether the power handling capability of the antenna would be constrained by the 2.4 mm connector or the honeycomb absorber the final simulation model was re-run and the power density inside the absorber was calculated when the antenna source input power was set to the maximum 2.4 mm power handling, see [88] and Figure 4.57.

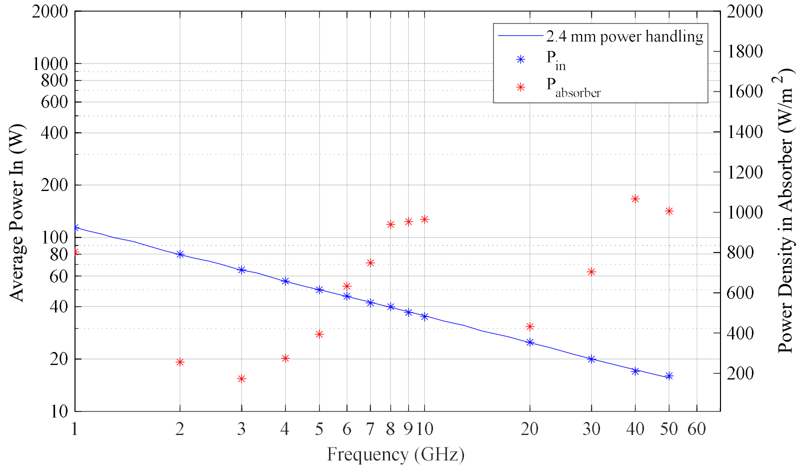

Figure 4.57. Simulated power density calculations in the absorber filled cavity of the 0.5-50 GHz DRGH.

The maximum power density inside the absorber was found to be less than 1.1 kW/m^2, this is well within the claimed power handling of a honeycomb absorber e.g. between 3 kW/m^2 (2 W/inch^2) to 15 kW/m^2 (10 W/inch^2), see [90] - [94]. Thus, this antenna would be suitable for use in applications where the required power handling does not exceed the maximum power handling of a 2.4 mm connector i.e. 114 W CW at 1 GHz down to 16 W CW at 50 GHz.

4.7 SUMMARY

This chapter showed how a 100:1 (0.5-50 GHz) DRGH was designed using the 0.5-18 GHz DRGH designed in Chapter 3 as a starting point. This chapter started by presenting the requirements to which the 0.5-50 GHz design should adhere, which is similar in most aspects to the 0.5-18 GHz requirements except for the removal of the high power requirement and the obvious increase of the required upper-frequency operational limit. EM simulations were again used extensively with a detailed discussion in Section 4.2 on the improvements implemented on the FEKO model of the 0.5-18 GHz DRGH to enable accurate simulations above 18 GHz.

The updated model was then used to investigate the bandwidth-limiting parts and or sub-assemblies of the antenna in Section 4.3 using the same approach as in Section 3.3. It was found that the bandwidth was limited by the existing coax-to-waveguide launcher and ridge design. Additionally, it was found that in the mmW-band severe performance degradation of the radiation patterns is caused when the grid sidewalls are implemented on a PCB with dielectric substrate.

In Section 4.4 the ridges were redesigned with the ridge gap and width optimised using the parametric studies from Section 4.3. A sub-ridge and several tapered ridge width sections in the main ridge were also introduced to improve performance. The coax-to-waveguide launcher was redesigned with a cavity filled with a honeycomb absorber, similar to cavity-backed spiral antennas, and the feeding section was implemented with a novel 3D printed sub-assembly based on the feeding section of a typical Vivaldi antenna. The detailed prototype design, making extensive use of 3D printing, was presented in Section 4.5 and the measured results for the prototype are shown in Section 4.6.

CHAPTER 5 PROPOSED DESIGN METHOD

In the previous two chapters, an existing DRGH design was used as a starting point to investigate, optimise and extend the bandwidth of the existing design. The designs presented in the previous chapters can of course be scaled to cover other frequency ranges, but the ultimate aim would be to have a design approach or method that would allow one to design a completely new DRGH antenna with very specific requirements. This chapter proposes a method that can be used to design a basic DRGH, excluding the waveguide launcher, starting with a very specific set of requirements. This design can then be used as a starting point for further optimisation. Depending on the desired bandwidth EM simulation can be used to design the waveguide launcher using either a stepped pyramidal cavity as in Chapter 3 or an absorber-filled cavity as shown in Chapter 4.

5.1 PROPOSED METHOD TO DESIGN A WIDEBAND DRGH

The proposed method is as follows:

1. Choose the lowest and highest frequency of operation, f_l and f_h as well as the desired characteristic impedance Z_0 and boresight gain G_l at f_l.
2. The interface between the flared waveguide and launcher assembly should be designed next, this means finding the values of A, B, S and D, see Figure 2.10. As mentioned in [38] the MUB increases very rapidly as the ridge gap D becomes small, thus choosing a very small ridge gap is advisable. Examples of ridge gap dimensions that can be used as a guideline are D = 1.1 mm to D = 0.7 mm for operation up to f_h = 18 GHz, refer to Chapter 3, [14] and [45]. For operation up to f_h = 50 GHz the ridge gap should be in the order of D = 0.4 mm, refer to Chapter 4 and [87]. The ridge gap can be scaled using these values as guidelines for an alternative f_h. Of course, making

the ridge gap too small might not be possible due to manufacturing tolerances or requirements on power handling. As seen from the graphs in [38], [80] and from the discussion in Section 3.7 a smaller value for *D/B* results in a larger MUB. The *D/B* ratio in [14] is approximately 0.015 and in [45], 0.018 to 0.012 depending on what value is used for the ridge gap, while in [87] the *D/B* ratio is 0.007. So as a guideline, a good starting value for *D/B* is $D/B = k_1 = 0.01$ from which *B* can be calculated. According to [80] the TE_{30} mode is skipped if the conditions of (5.1) and (5.2) are met thus resulting in increased MUB.

$$\frac{(A-S)/2}{B} = \frac{1}{2} \tag{5.1}$$

$$\frac{S}{B} < \frac{1}{2} \tag{5.2}$$

A constant k_2 is defined that modifies (5.2) to become (5.3). Using (5.3) it is found that the value for k_2 in the designs presented in [14], [45] and [87] varies from 0.35 to 0.08 so a value of $k_2 = 0.1$ is proposed as a starting value for new designs. The dimension *S* can then be calculated from (5.3) and subsequently *A* from (5.1).

$$S = 0.5 \cdot B \cdot k_2 \tag{5.3}$$

Using the transverse resonance method as defined in (2.6) to (2.9), (2.14), (2.15) and (2.20) to (2.22) the TE_{10} mode cut-off frequency f_c and characteristic impedance Z_0 can be calculated from the values of *A*, *B*, *S* and *D*. If f_c is greater or significantly less than f_l or if Z_0 does not match the desired impedance, the values of k_1 and or k_2 can be iteratively adjusted and the calculation re-run. For some cases, it might be necessary to settle with an impedance that does not exactly match the desired impedance, for example, 30 Ω or 40 Ω instead of 50 Ω.

3. The next step is to determine the flared waveguide aperture dimensions. In general, especially at high frequencies where the ridges dominate the radiation characteristics and for wide bandwidths, it is not possible to use the effective aperture formula to

calculate the gain of DRGH antennas. This formula can still be useful as a guideline to find the nominal aperture size needed to achieve the desired gain at the low-frequency end where the ridges have less of an effect on the gain. The effective aperture can be calculated from (5.4) where λ_l is the wavelength in metre at the lowest frequency and G_l the desired gain at the lowest frequency.

$$A_{eff} = \frac{\lambda_l^2}{4\pi} G_l \tag{5.4}$$

The physical aperture area (A_{phys}) is then found by dividing the effective aperture by the aperture efficiency. A good starting point is to use a value of 0.7 to 0.8 for the aperture efficiency at the lowest frequency, see Figure 22 in [87]. A good starting value for the ratio of the *H*-plane aperture width (A_{ap}) to *E*-plane aperture width (B_{ap}), is $A_{ap}/B_{ap} = 1.75$. Note that for the 0.5-18 GHz and 0.5-50 GHz DRGH antennas designed in Chapters 3 and 4, the ratio was 264/152 ≈ 1.74. Another guideline is to use the requirements on DRGH apertures as set out in [41] i.e. for the 0.2-1 GHz DRGH an aperture of 94.5×69 cm is required (ratio of approximately 1.37) and for the 1-18 GHz DRGH an aperture of 24.2×13.6 cm is required (ratio of approximately 1.85). The physical area of the aperture is just A_{ap} multiplied by B_{ap}, thus using the chosen ratio of A_{ap}/B_{ap} and the physical aperture calculated earlier the *H*- and *E*-plane aperture dimensions can be calculated.

4. According to [38] the axial length (*L*) of the flared waveguide assembly should be reasonably long to ensure proper impedance transformation using ridges, in the order of half a wavelength at the lowest operating frequency. For some horn designs, this can result in either a very short or a very long horn. For the designs presented in [14], [45] and [87] the axial length is less than the *H*-plane aperture, but more than the *E*-plane aperture, being typically close to the mean of the two values, thus a good starting point would be to use the mean of the *H*- and *E*-plane aperture width.
5. For wideband operation, it is advised to implement the *E*-plane sidewalls with a grid construction. The spacing between the grid elements should be a tenth of a wavelength at the lowest operating frequency to simulate a solid conducting wall at

these frequencies [38]. The grids should be as thin as possible to reduce the chance of performance degradation due to reflection, but strong enough to be self-supporting. As a guideline, grids with strip widths in the order of 3 to 1 mm were found to work well [45], [87].

6. The ridge gap (*D*) and width (*S*) at the launcher interface were already determined in step 2. For the ridge profile, most of the studies and designs in the literature used an exponential profile, refer to Section 2.3.4. The exponential profile can be implemented by for example using (2.1) and (2.2), but as a physical profile, not an impedance profile, similar to (2.5). The ridges should be extended axially straight backwards into the area where the coax-to-waveguide launcher will be added for half a wavelength at the highest frequency to ensure the TE_{20} mode is not excited [38].
7. The coaxial feed inner conductor design will depend on the connector used and other factors, such as the desired power handling. For example, typical precision N-type (for example Southwest Microwave 312-14SF) or SMA (for example Huber & Suhner 23SMA-50-0-165) connectors used up to 18 GHz accept pins with a diameter of 0.036" or 0.914 mm while 50 GHz connectors such as the Southwest Microwave model 1412-04SF 2.4 mm connector can accept a maximum pin diameter of 0.02" or 0.508 mm. The feed pin can have a short thinner section that mates with the connector spring fingers and a thicker section for the rest of the feed pin which can be tapered if the ridge impedance is not 50 Ω. The feed pin should sit in the centre of the ridge to ensure that the TE_{20} mode is not excited [38]. The outer conductor diameter can then be calculated from (3.1).

Using the dimensions determined above an EM model can be created and the electrical performance simulated.

At this stage the only step remaining before the design can be physically realised is to add the coax-to-waveguide launcher. For bandwidths below 36:1, a coax-to-waveguide launcher similar to that proposed in Chapter 3 can be implemented and for bandwidths above 36:1 an absorber-filled cavity as shown in Chapter 4. The optimal dimensions for these launchers can be found using parametric studies in EM simulation and the dimensions as given in

Chapter 3 and Chapter 4 as starting point. As a final step to improve performance if required, the ridge dimensions, for example, the ridge gap, ridge width, ridge profile, etc. can be optimised with parametric studies in simulation using the complete horn model. In the next section, two examples will be shown to illustrate the use of these guidelines.

5.2 EXAMPLES OF WIDEBAND DRGH ANTENNA DESIGNS

In the first example a 2-50 GHz DRGH will be designed, such an antenna would be ideal to measure RESM systems that work over a frequency range of 2-40 GHz. In the second example, a 0.2-18 GHz DRGH will be designed, this antenna would be suited for EMC/I measurements where it can replace the 0.2-1 and 1-18 GHz DRGH antennas with a single antenna, but due to the bandwidth of this design an absorber cavity is necessary and therefore the antenna cannot be used for high power tests.

5.2.1 DRGH Design Example: 2-50 GHz

The dimensions were determined following the guidelines in Section 5.1 as follows:

1. The lowest and highest frequency of operation is f_l = 2 GHz and f_h = 50 GHz. The desired characteristic impedance is Z_0 = 50 Ω and the boresight gain G_l = 7 dB at the lowest frequency.
2. The ridge gap D is chosen as 0.4 mm for operation up to 50 GHz as per the guideline. With the proposed starting values of k_1 = 0.01 and k_2 = 0.1, the dimensions and parameters were calculated as: A = 42 mm, B = 40 mm, S = 2 mm, f_c = 0.84 GHz and Z_0 = 47.2 Ω using the transverse resonance method. Although the impedance is close to desired, the low-frequency cut-off is far below the desired f_l. The values of k_1 and k_2 were then iteratively adjusted until the impedance was closer to 50 Ω and the cut of frequency close to 95% of f_l. This occurred at a choice of k_1 = 0.022 and k_2 = 0.22 with the dimensions and parameters calculated as: A = 20.2 mm, B = 18.2 mm, S = 2 mm, f_c = 1.915 GHz and Z_0 = 50.4 Ω.

3. The effective aperture for G_l = 7 dB at f_l = 2 GHz is calculated from (5.4) as 90 mm^2. Using an aperture efficiency of 0.8 the physical aperture is A_{phys} = 112 mm^2. Then using a ratio of A_{ap}/B_{ap} =1.75 the aperture dimensions are calculated as A_{ap} = 140.1 mm and B_{ap} = 80.1 mm.
4. Using the aperture values in step 3 the axial length is calculated as L = 110.1 mm from the mean of A_{ap} and B_{ap}.
5. The strip gap was calculated as 15 mm (a tenth of a wavelength at 2 GHz). As per the minimum guideline, the strip width was chosen as 1 mm to keep reflections from the strips as small as possible.
6. An exponential ridge profile was used with the physical profile values calculated using (2.1) and (2.2) as shown in (5.5) where x is the distance along the horn axis and y is the perpendicular distance from the horn axis to the ridge profile.

$$y = \frac{D}{2}\, e^{(\frac{1}{L})\ln(\frac{Bap}{D})x} = 0.2\, e^{0.0481341x} \tag{5.5}$$

   The ridges were extended straight back 3 mm (half wavelength at 50 GHz) [38].
7. For this design, a feed pin diameter of 0.5 mm is used. This allows easy integration with a 2.4 mm connector, similar to the design in Chapter 4. The outer conductor diameter was calculated using (3.1) as 1.155 mm for Z_0 = 50.2 Ω.

The basic design was then implemented in FEKO, the model is shown in Figure 5.1(a). The final design shown in Figure 5.1(b) was optimised as follows:

- Addition of a stepped pyramidal cavity as implemented in the 0.5-18 GHz DRGH with dimensions, shown in Figure 5.2, optimised for this design following the same approach as presented in Section 3.4.1.
- Reduction of the ridge width and gap to S = 1.6 mm and D = 0.3 mm respectively.
- An optimised Bezier curve ridge profile with control points as shown in Table 5.1. Note that the curve start point is located at the coax-to-waveguide launcher interface with the flared waveguide.

- Removal of every second grid strip and the grid strip at the coax-to-waveguide launcher interface.

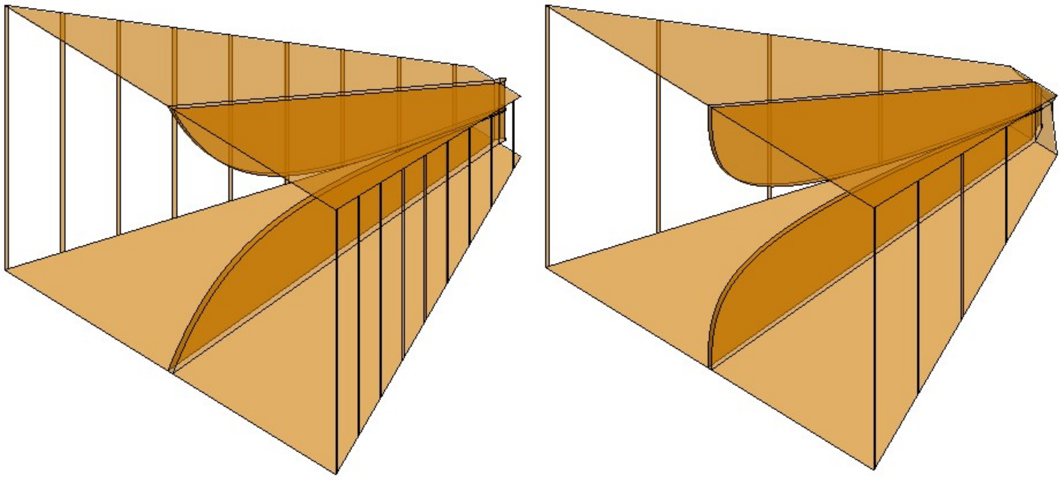

(a) (b)

Figure 5.1. (a) Basic design and (b) final optimised design.

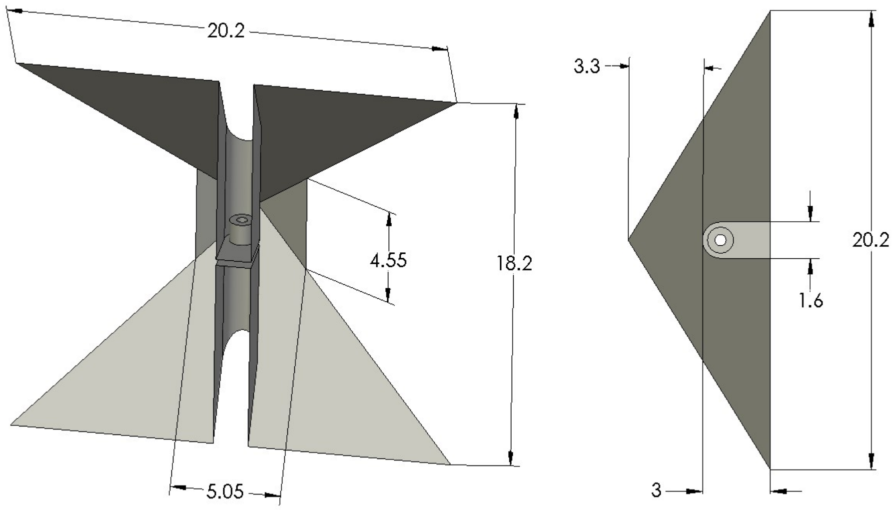

Figure 5.2. Stepped pyramidal cavity dimensions.

Table 5.1. Cubic Bezier control points of the ridge profile (in mm).

Bezier point	**Description**	**Axial distance (x)**	**Perpendicular distance (z)**
P0	Start point	0	0.15
P1	Start tangent point	105.10	0.15
P3	End tangent point	110.1	15
P4	End point	110.1	40.05

The simulated VSWR and boresight realised gain results for the basic and final optimised design are shown in Figure 5.3(a) and Figure 5.3(b), respectively. The VSWR is typically below 2:1 and the boresight gain increases from 7 dBi at 2 GHz to above 14 dBi at 50 GHz. No pattern deterioration was observed when reviewing all the simulated 3D radiation patterns, see for example Figure 5.4.

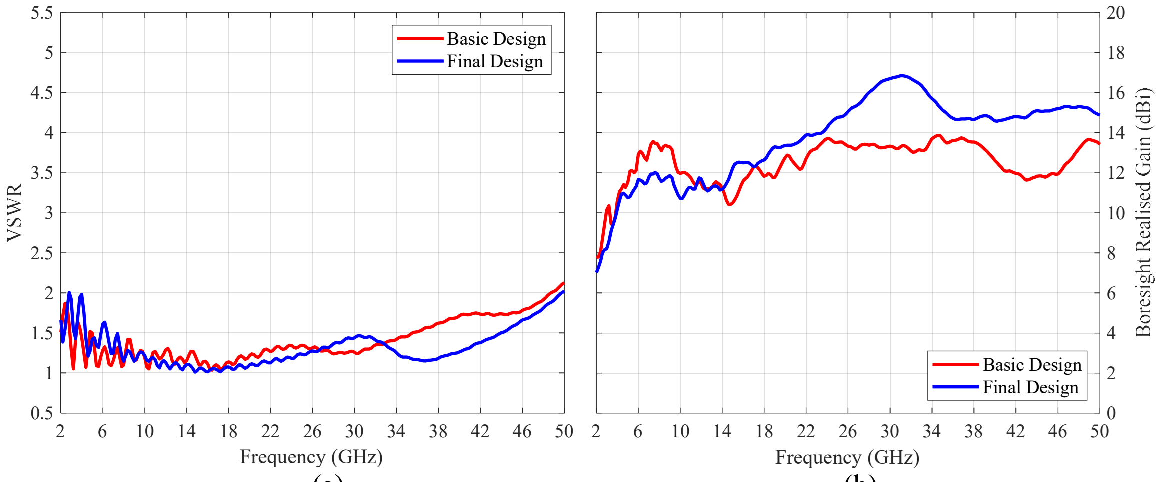

(a) (b)

Figure 5.3. (a) VSWR and (b) boresight gain comparison between the basic and final optimised 2-50 GHz DRGH design.

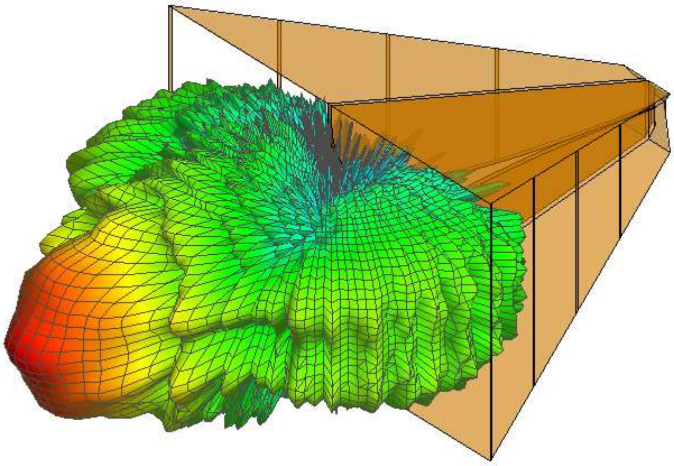

Figure 5.4. 3D radiation pattern at 50 GHz for the final optimised design.

5.2.2 DRGH Design Example: 0.2-18 GHz

The dimensions were determined following the guidelines in Section 5.1 as follows:

1. The lowest and highest frequency of operation is chosen as f_l = 0.2 GHz and f_h = 18 GHz. The desired characteristic impedance is Z_0 = 50 Ω and boresight gain G_l = 3 dBi at the lowest frequency.
2. The ridge gap D is chosen as 1 mm for operation up to 18 GHz as per the guideline. With the proposed starting values of k_1 = 0.01 and k_2 = 0.1, the dimensions and parameters were calculated as: A = 105 mm, B = 100 mm, S = 5 mm, f_c = 0.34 GHz and Z_0 = 47.2 Ω using the transverse resonance method. Although the impedance is close to desired, the low-frequency cut-off is well above the desired f_l. The values of k_1 and k_2 were then iteratively adjusted until the cut-off frequency was as close as possible to 0.2 GHz. This occurred at a choice of k_1 = 0.0065 and k_2 = 0.08, with the dimensions and parameters calculated as A = 160 mm, B = 154 mm, S = 6.2 mm, f_c = 0.202 GHz and Z_0 = 40 Ω. The impedance is not 50 Ω as desired and the cut-off frequency is not below 0.2 GHz, but it was found that if the cut-off frequency is reduced, the impedance decreases further and vice versa. Thus further adjustment of the parameters k_1 and k_2 is not possible.

3. The effective aperture for $G_l = 3$ dB at $f_l = 0.2$ GHz is calculated from (5.4) as 357 mm^2. Using an aperture efficiency of 0.8 the physical aperture is A_{phys} = 446 mm^2. Then using a ratio of A_{ap}/B_{ap} =1.75 the aperture dimensions are calculated as A_{ap} = 884 mm and B_{ap} = 505 mm.
4. Using the aperture values in step 3 the axial length is calculated as L = 694.5 mm from the mean of A_{ap} and B_{ap}.
5. The strip gap was calculated as 150 mm (a tenth of a wavelength at 0.2 GHz). As per the minimum guideline, the strip width was chosen as 1 mm to keep reflections from the strips as small as possible.
6. An exponential ridge profile was used with the physical profile values calculated using (2.1) and (2.2) as shown in (5.6) where x is the distance along the horn axis and y is the perpendicular distance from the horn axis to the ridge profile.

$$y = \frac{D}{2}\, e^{(\frac{1}{L})\ln(\frac{Bap}{D})x} = 0.5\, e^{0.0089626x} \tag{5.6}$$

   The ridges were extended straight back 8.33 mm (half wavelength at 18 GHz) [38].
7. For this design a feed pin diameter of 1.6 mm is used, similar to the design in [14], refer to Section 3.3.1. The outer conductor diameter was calculated using (3.1) as 3.7 mm for Z_0 = 50.3 Ω. There would thus be an impedance mismatch between the ridges and the coax feed, but not between the coaxial feed and 50 Ω connector.

The basic design was then implemented in FEKO, the model is shown in Figure 5.5(a). The flared waveguide assembly of the two optimised designs shown in Figure 5.5(b) and Figure 5.5(c) was optimised as follows:

- Addition of an absorber loaded cavity as implemented in the 0.5-50 GHz DRGH with dimensions optimised for this design following the same approach as presented in Section 4.4.1. Two designs were considered, one using a carbon foam absorber and the other a magnetic absorber in order to illustrate the use of alternative absorbers. The details of these designs will be discussed in more detail below.
- Reduction of the ridge width to 4.7 mm.

- An optimised Bezier curve ridge profile with control points as shown in Table 5.2. Note that the curve start point is located at the coax-to-waveguide launcher interface with the flared waveguide.

Table 5.2. Cubic Bezier control points of the ridge profile (in mm).

Bezier point	Description	Axial distance (x)	Perpendicular distance (z)
P0	Start point	0	0.5
P1	Start tangent point	544.5	0.5
P3	End tangent point	704.5	30
P4	End point	694.5	252.5

For the design of Figure 5.5(b) an absorber-filled cavity similar to the design of Chapter 4 was implemented using a 57 mm thick carbon foam absorber (Eccosorb AN77) modelled as multiple SEP dielectric material layers with different dielectric constant and loss tangents for each layer to account for the gradient loading of the carbon. For the design of Figure 5.5(c), a shallower cavity was added and loaded with a rigid epoxy-based magnetic absorber (Eccosorb MF117). This absorber was modelled as a single SEP volume using the manufacturer-supplied dielectric and magnetic constants and loss tangents. These values vary over frequency and were thus imported as a frequency list. A pyramidal cavity was cut into the absorber at the feed point.

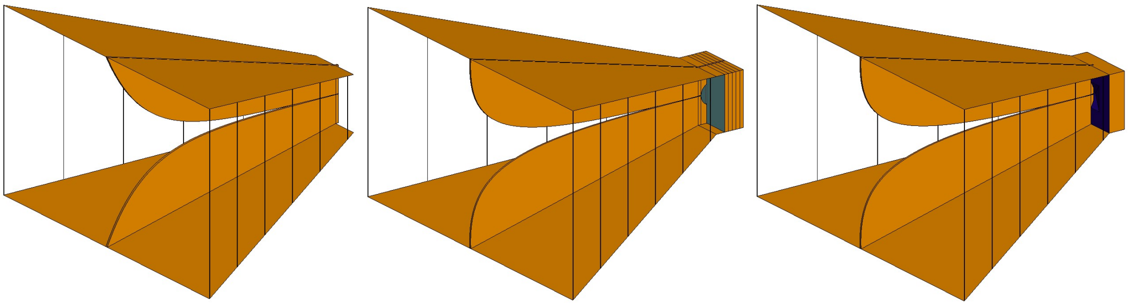
(a) (b) (c)

Figure 5.5. (a) Basic design, (b) final optimised design with foam absorber and (c) magnetic absorber.

A close-up view of the EM simulation model of both cavity designs is shown in Figure 5.6. The dimensions of the carbon foam absorber cavity and magnetic absorber cavity are shown in Figure 5.7 and Figure 5.8, respectively.

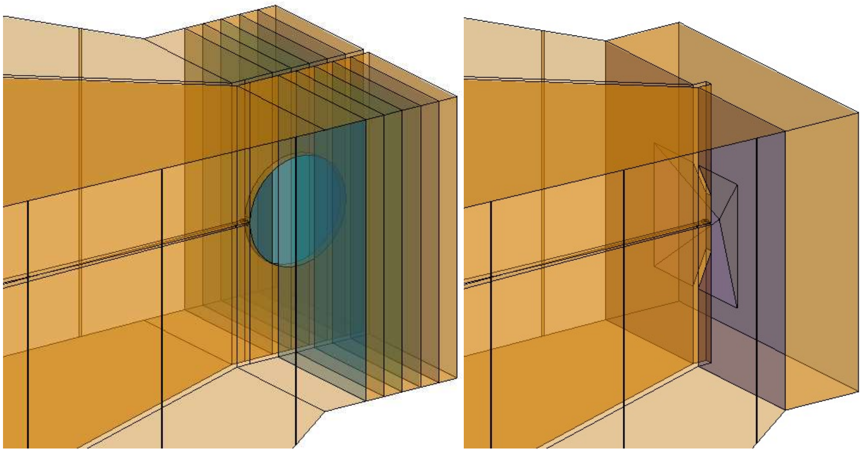

(a) (b)

Figure 5.6. (a) Simulation model of cavity design with foam and (b) magnetic absorber.

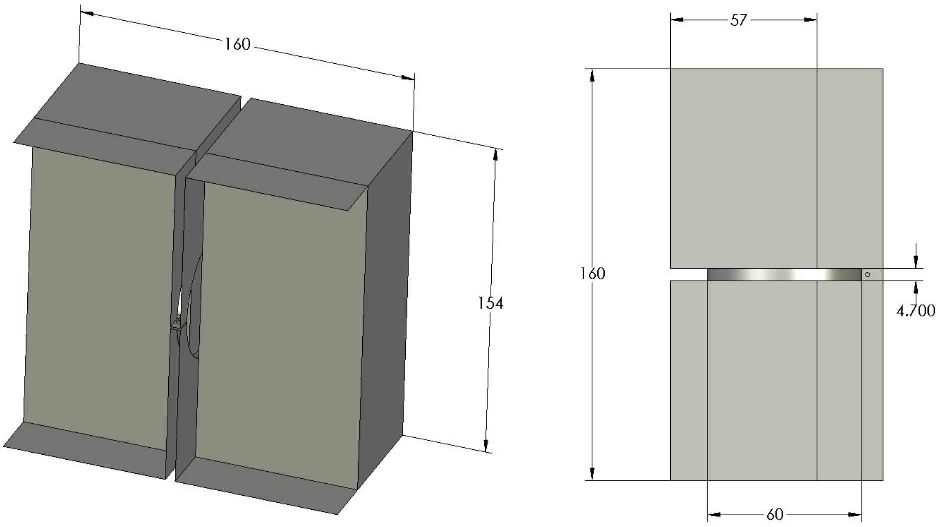

Figure 5.7. Carbon foam absorber cavity dimensions.

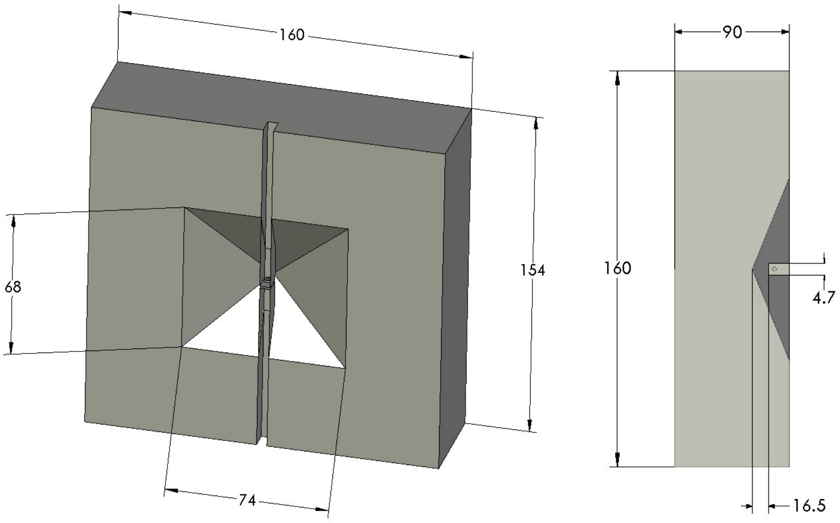

Figure 5.8. Magnetic absorber cavity dimensions.

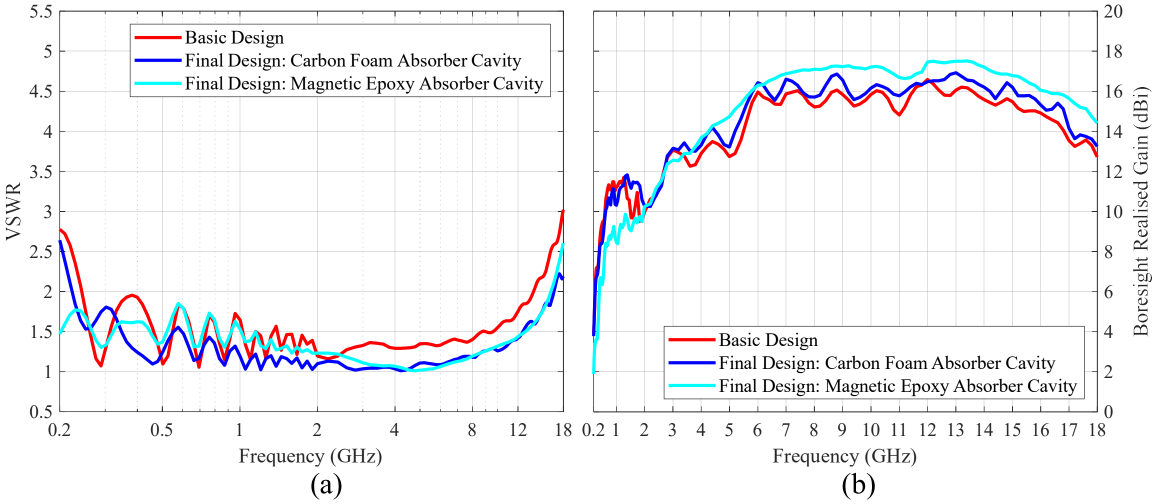

(a) (b)

Figure 5.9. (a) VSWR and (b) boresight gain comparison for the basic and final optimised 0.2-18 GHz DRGH designs.

The simulated VSWR and boresight realised gain results for the basic and final optimised designs are shown in Figure 5.9(a) and Figure 5.9(b) respectively. The VSWR is typically below 2:1 with a maximum of around 2.5:1 at the band edges. The boresight gain increases from 2 dBi at 2 GHz for the magnetically loaded cavity design and 4 dBi for the carbon foam design to 14 dBi and 13 dBi respectively at 18 GHz. No pattern deterioration was observed when reviewing all the simulated 3D radiation patterns, see for example Figure 5.10.

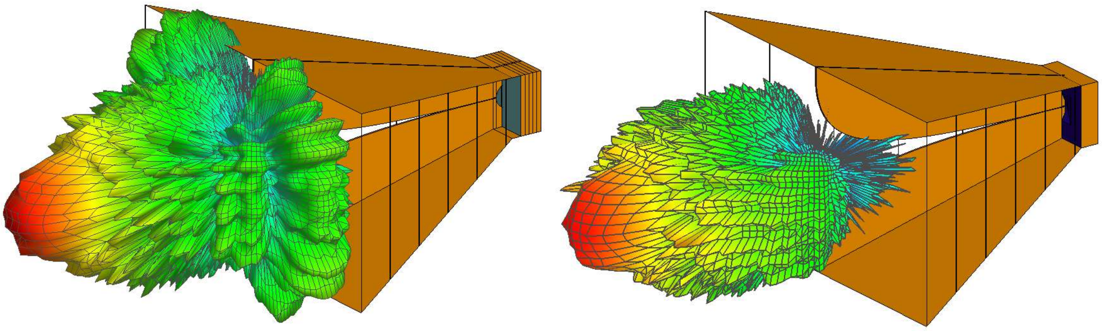

(a) (b)

Figure 5.10. (a) 3D radiation pattern at 18 GHz for the final optimised design with foam and (b) magnetic absorber.

5.3 SUMMARY

A method that could be used to design a basic wideband DRGH, excluding the waveguide launcher, from scratch that can then be used as a starting point for optimisation was proposed in this chapter. Once the basic dimensions are calculated using this method further optimisation can be done using EM simulation as shown in this chapter as well as the previous two chapters. To show how the method can be used two design examples were illustrated, a 2-50 GHz DRGH design and a 0.2-18 GHz DRGH design.

CHAPTER 6 CONCLUSION

6.1 CONCEPTUAL REVIEW OF DRGH OPERATION

During this study, it was observed that the DRGH radiation and VSWR performance above a certain frequency is dictated by the ridge design. It is expected that at higher frequencies, the operational limit will be the manufacturing tolerances and technology used, and at lower frequencies, the maximum permissible size of the antenna. The ridge width, gap, and profile for the desired frequency range and performance could be found using parametric studies on the ridges in isolation. For higher frequency performance the ridge width and gap need to be reduced, for lower frequency performance the ridge aperture and ridge axial length need to be increased. Inherently the ridges in isolation are similar to the radiating portion of TEM and Vivaldi antennas and are nominally frequency independent. The frequency of operation is only limited by practical manufacturing constraints, i.e. the minimum sizes (ridge gap, width, and feed) that can be manufactured (high-frequency operation) and the maximum aperture and axial length of the flared assembly that can be accommodated (low-frequency performance).

The ridges cannot practically be used in isolation and need some connecting structure, typically in the form of a cavity which can take various forms, but introducing these cavities to the ridges disturbs the nominal frequency-independent nature of the ridges. Over many years, changes and improvements in the cavity or coax-to-waveguide launcher design brought about mostly through experimentation using measurement and or simulation, have resulted in increased DRGH bandwidth performance. The problem is that if the coax-to-waveguide launcher structure is too small it will lead to the low-frequency end being below cut-off and on the opposite end, if the coax-to-waveguide launcher is too large it will lead to high-frequency pattern breakup caused either by higher-order modes or reflection from the cavity walls. Not all energy travels down the ridges and this results in backward radiation. At low frequencies the backward radiation will be suppressed by the coax-to-waveguide launcher structure, however, at high frequencies the truncated structure of the ridges will still support backwards radiation. This can be improved somewhat using a circular cavity similar to a Vivaldi antenna right behind the ridges, but then there is still some radiation to the sides. The same problem is solved in cavity-backed spiral antennas using an absorptive cavity. It does come at the loss of some performance but allows significantly wider bandwidths compared to empty cavities.

Adding flares and sidewalls to the DRGH improves low-frequency performance. Some high-frequency degradation is caused due to reflection from sidewalls especially if the sidewalls are implemented as a grid structure on a dielectric substrate.

6.2 SUMMARY

The problem, identified in the introduction, is the requirement from various industries for wider bandwidth electronic systems which leads to a desire for wider bandwidth antennas used for testing these systems, such as DRGH antennas. The research gap was defined as the availability of design procedures or guidelines to design and manufacture DRGH antennas with bandwidths of significantly more than 18:1 with the objective of this study being to address this gap. The research questions postulated in Section 1.3 were answered in Chapters 3 to 5, using the approach as defined in Section 1.4, as follows:

- The most important parts and or sub-assemblies of the DRGH with regards to limiting the bandwidth are the ridges and coax-to-waveguide launcher.
- It is possible to redesign these parts and or sub-assemblies to extend the bandwidth while maintaining acceptable electrical performance.

- It is possible to physically implement these designs and manufacture DRGH antennas with bandwidths of 100:1 and possibly beyond. In addition, it was possible to do this while adhering to the additional requirements on electrical performance and suitability for use in various applications.

In Table 6.1 the DRGH bandwidth-extended designs presented in Chapters 3 to 5 are added to Table 2.1. This table compares the widest bandwidth designs found in the literature with regards to frequency range, bandwidth and whether the designs were verified with measurements on a prototype or not. From this table, it is clear that the designs presented in this study are the widest bandwidth designs available in the literature that have been verified with measurements and that the bandwidth has been significantly extended beyond 18:1.

Table 6.1. DRGH Bandwidth comparison.

Reference	**Frequency Range (GHz)**	**Bandwidth**	**Verified with measurements**
[20]	2-40	20:1	Yes
[10], [11]	0.8-18	22.5:1	Yes
[23]	0.8-20	25:1	Yes
Chapter 5	**2-50**	**25:1**	**No**
[13]	0.7-18	25.7:1	No
[45], **Chapter 3**	**0.5-18**	**36:1**	**Yes**
[26]	0.6-50	83:1	No
Chapter 5	**0.2-18**	**90:1**	**No**
[87], **Chapter 4**	**0.5-50**	**100:1**	**Yes**

6.3 CONTRIBUTION

With reference to Sections 1.5 and 1.6 this study has made the following contributions to the electronic engineering knowledge base and more specifically DRGH antenna design:

- The widest bandwidth, validated, DRGH antenna designs published to date in literature, confirming the feasibility of designing and manufacturing DRGH antennas with bandwidth ratios of 100:1 and potentially even beyond.
- Detailed information on methods that can be used to design and manufacture these antennas.
- Several novel coax-to-waveguide launcher, ridge and coaxial feed designs.
- As research output, most of the results of this study were published in the literature, see [45], [87].

REFERENCES

[1] 3GPP TS 38.101-1, “NR; User Equipment (UE) radio transmission and reception; Part 1: Range 1 Standalone,” no. 18.1.0. Mar. 2023.

[2] J. L. Kerr, “Short axial length broad-band horns,” *IEEE Trans. Antennas Propag.*, vol. 21, no. 5, pp. 710–714, Sep. 1973.

[3] C. Bruns, P. Leuchtmann, and R. Vahldieck, “Full wave analysis and experimental verification of a broadband ridged horn antenna system with parabolic reflector,” in *Proc. IEEE Antennas Propag. Soc. Int. Symp.*, Jul. 8-13, 2001, pp. 230–233.

[4] C. Bruns, P. Leuchtmann, and R. Vahldieck, “Analysis and Simulation of a 1-18-GHz broadband double-ridged horn antenna,” *IEEE Trans. Electromagn. Compat.*, vol. 45, no. 1, pp. 55–60, Feb. 2003.

[5] C. Bruns, P. Leuchtmann, and R. Vahldieck, “Comprehensive analysis and simulation of a 1-18 GHz broadband parabolic reflector horn antenna system,” *IEEE Trans. Antennas Propag.*, vol. 51, no. 6, pp. 1418–1422, Jun. 2003.

[6] V. Rodriguez, “New broadband EMC double-ridged guide horn antenna,” *RF Design*, vol. 27, no. 5, pp. 44–50, May. 2004.

[7] V. Rodriguez, “Dual ridge horn antenna,” U.S. Patent 6 995 728 B2, Feb. 07, 2006.

[8] M. Abbas-Azimi, F. Arazm, J. Rashed-Mohassel, and R. Faraji-Dana, “Design and optimization of a new 1–18 GHz double ridged guide horn antenna,” *J. Electromagn. Waves Appl.*, vol. 21, no. 4, pp. 501–516, Jan. 2007.

[9] H. Xu, Y. Zhou, E. Li, H. Liu, Q. Wang, and Z. Zhong, “Design and simulation of ultra-wideband double-ridged horn antenna,” in *Int. Conf. Microw. Millimeter Wave Technol.,* May 8-11, 2010, pp. 950–952.

[10] H. Steghafner, D. Leugner, and B. Klos, “Horn antenna,” U.S. Patent 7 969 376 B2, Jun. 28, 2011.

[11] Rohde & Schwarz, “R&S HF907 Double-ridged waveguide horn antenna,” HF907 datasheet, HF – VHF/UHF Antennas, Catalog 2017/2018.

[12] M. Ghorbani and A. Khaleghi, “Wideband double ridged horn antenna: pattern analysis and improvement,” in *Proc. 5th Eur. Conf. Antennas Propag. (EUCAP)*, Apr. 11-15, 2011, pp. 865–868.

[13] M. Ghorbani and A. Khaleghi, “Double ridged horn antenna designs for wideband applications,” in *Proc. 19th Iranian Conf. Elect. Eng.*, May 17-19, 2011, pp. 1–4.

[14] B. Jacobs, J. W. Odendaal, and J. Joubert, “An improved design for a 1–18 GHz double-ridged guide horn antenna,” *IEEE Trans. Antennas Propag.*, vol. 60, no. 9, pp. 4110–4118, Sep. 2012.

[15] M. Abbas-Azimi, F. Arazm, and J. Rashed-Mohassel, “Sensitivity analysis of a 1 to 18 GHz broadband DRGH antenna,” in *Proc. IEEE Antennas Propag. Soc. Int. Symp.*, Jul. 9-14, 2006, pp. 3129–3132.

[16] B. Jacobs, J. W. Odendaal, and J. Joubert, “The effect of manufacturing and assembling tolerances on the performance of double-ridged horn antennas,” *J Electromagn. Waves Appl.*, vol. 24, no. 10, pp. 1279–1290, Jul. 2010.

[17] B. Jacobs, “The effect of manufacturing and assembling tolerances on the performance of 1-18 GHz double ridged guide horn antennas,” M. Eng. thesis, University of Pretoria, South-Africa, 2010.

[18] M. Botello-Perez, H. Jardon-Aguilar, and I. G. Ruiz, “Design and simulation of a 1 to 14 GHz broadband electromagnetic compatibility DRGH antenna,” in *Proc. 2nd Int. Conf. Elect. Electron. Eng.*, Sep. 9, 2005, pp. 118–121.

[19] V. Rodriguez, “Recent improvements to dual ridge waveguide horn antennas: The 200MHz to 2000MHz and 18GHz to 40GHz models,” in *Proc. IEEE Int. Symp. Electromagn. Compat.*, Aug. 17-21, 2009, pp. 24–27.

[20] Tenigeer, N. Zhang, J. Qiu, P. Zhang, and Y. Zhang, “Design of a novel broadband EMC double ridged guide horn antenna,” *Prog. Electromagn. Res. C*, vol. 39, pp. 225–236, Jan. 2013.

[21] M. A. Morgan and T. A. Boyd, “A 10–100-GHz double-ridged horn antenna and coax launcher,” *IEEE Trans. Antennas Propag.*, vol. 63, no. 8, pp. 3417–3422, Aug. 2015.

[22] L. Wei and X. XiaoLi, “Design and simulation of TEM double ridge guide horn antenna,” in *Proc. 8th Int. Conf. Electron. Meas. Instruments*, Aug. 16-18, 2007, pp. 1-703-1–706.

[23] C. Wang, E. Li, Y. Zhang, and G. Guo, “Ridged horn antenna with adjustable metallic grid sidewalls and cross-shaped back cavity,” *IEEE Antennas Wireless Propag. Lett.*, vol. 15, pp. 1221–1225, Nov. 2015.

[24] M. Gerber, J. W. Odendaal, and J. Joubert, “Ridge profile optimization of DRGH antenna,” in *Proc. IEEE Radio Antenna Days Indian Ocean*, Oct. 15-18, 2018, pp. 1–3.

[25] M. Gerber, J. W. Odendaal, and J. Joubert, “DRGH antenna with improved gain and beamwidth performance,” *IEEE Trans. Antennas Propag.*, vol. 68, no. 5, pp. 4060–4065, May. 2020.

[26] P. D. Kuroptev, V. V. Levyakov, and A. V. Fateev, “Modified 0.6–50 GHz ultra-wideband double-ridged horn antenna design for parameters improvement,” in *Proc. 47th Eur. Microw. Conf.*, Oct. 10-12, 2017, pp. 1313–1316.

[27] *FEKO.* Altair. Accessed: Dec. 4, 2024. [Online]. Available: https://altair.com/feko.

[28] *CST Studio Suite.* Simulia. Accessed: Dec. 4, 2024. [Online]. Available: https://www.3ds.com/products-services/simulia/products/cst-studio-suite/.

[29] O. J. Lodge, *Signaling Across Space Without Wires.* London, England: “The Electrician” Printing and Publishing Co. Ltd., 1898.

[30] Lord Rayleigh, “On the passage of electric waves through tubes, or the vibrations of dielectric cylinders,” *The London, Edinburgh, and Dublin Philos. Mag. and J. of Sci.*, vol. 43, no. 261, pp. 125–132, 1897.

[31] J. C. Bose, “IX. On a complete apparatus for the study of the properties of electric waves,” *The London, Edinburgh, and Dublin Philos. Mag. and J. of Sci.*, vol. 43, no. 260, pp. 55–68, 1897.

[32] G. C. Southworth and A. P. King, “Metal horns as directive receivers of ultra-short waves,” *Proc. of the IRE*, vol. 27, no. 2, pp. 95–102, Feb. 1939.

[33] W. L. Barrow and L. J. Chu, “Theory of the electromagnetic horn,” *Proc. of the IRE*, vol. 27, no. 1, pp. 51–64, Jan. 1939.

[34] W. L. Barrow, “Electromagnetic horn,” U.S. Patent 2 467 578 A, Jan. 09, 1939.

[35] S. B. Cohn, “Properties of ridge wave guide,” *Proc. of the IRE*, vol. 35, no. 8, pp. 783–788, Aug. 1947.

[36] S. Hopfer, “The design of ridged waveguides,” *IRE Trans. on Microw. Theory and Techn.*, vol. 3, no. 5, pp. 20–29, Oct. 1955.

[37] Radio Research Laboratory Harvard University, *Very High-Frequency Techniques*. Cambridge, MA, USA: McGraw-Hill, 1947.

[38] K. L. Walton and V. C. Sundberg, “Broadband ridged horn design,” *Microw. J*, vol. 4, no. 2, pp. 96–101, Mar. 1964.

[39] J. L. Kerr, “A very broad band low silhouette antenna,” Fort Monmouth, NJ, USA, Tech. Rep. ECOM-3087, Jan. 1967.

[40] J. L. Kerr, “Broadband horns,” USAECOM, Fort Monmouth, NJ, USA, Tech. Rep. ECOM-3319, Aug. 1970.

[41] MIL-STD-461G, “Requirements for the control of electromagnetic interference characteristics of subsystems and equipment.” Dec. 2015.

[42] T. İsenlik, E. Başaran, and B. Türetken, “A novel ultra wideband horn feed for parabolic reflector antennas,” in *Proc. IEEE Int. Conf. Ultra-Wideband*, Sep. 17-20, 2012, pp. 513–517.

[43] T. Isenlik, E. Basaran, and B. Turetken, “A novel 2–18-GHz double-ridged horn antenna with an improved feed section design,” *Electromagnetics*, vol. 35, no. 3, pp. 145–154, Mar. 2015.

[44] T. Isenlik, K. Yegin, and D. E. Barkana, “Near-constant beamwidth quadruple bandwidth double-ridged horn antenna design,” *IET Microw., Antennas Propag.*, vol. 13, no. 12, pp. 2102–2109, Jul. 2019.

[45] B. Jacobs, J. W. Odendaal, and J. Joubert, "Compact 0.5–18 GHz double-ridged guide horn antenna," *IET Microw., Antennas Propag.*, vol. 15, no. 4, pp. 427–440, Mar. 2021.

[46] A. R. Mallahzadeh and A. A. Dastranj, "Double-ridged conical horn antenna for 2-18 GHz," *Electromagnetics*, vol. 28, no. 6, pp. 450–461, Aug. 2008.

[47] N. Lee, C. Im, S. Park, and H. Choo, "Design of a metal 3D printed double-ridged horn antenna with stable gain and symmetric radiation pattern over a wide frequency range," *IEEE Access*, vol. 11, pp. 100565–100572, Sep. 2023.

[48] C. A. Balanis, *Antenna Theory: Analysis and Design,* 3rd edition, Hoboken, NJ, USA: Wiley, 2005.

[49] W. L. Stutzman and G. A. Thiele, *Antenna Theory and Design*, 2nd edition, Hoboken, NJ, USA: Wiley, 1998.

[50] Z. Chen, A. Mehdipour, and L. Matytsine, "Customized compact dielectric lens to improve double-ridge horn antenna performance for automotive immunity EMC test," in *Proc. IEEE Int. Symp. on Electromagn. Compat.*, Jul. 25-29, 2016, pp. 835–840.

[51] D. Baker and C. Van Der Neut, "A compact, broadband, balanced transmission line antenna derived from double-ridged waveguide," in *Proc. Antennas Propag. Soc. Int. Symp.*, May 24-28, 1982, pp. 568–571.

[52] A. Genc, I. Basyigit, T. Göksu, and S. Helhel, "The comparison of the characteristics of the double-ridged horn antennas depending the geometry of ridge profiles for wideband application," in *Proc. Progress Elecromagn. Res. Symp.,* May 22-25, 2017, pp. 1553-1557.

[53] B. M. Notaros, C. D. McCarrick, and D. P. Kasilingam, "Two numerical techniques for analysis of pyramidal horn antennas with continuous metallic ridges," in *Proc. IEEE Antennas Propag. Soc. Int. Symp.,* Jul. 8-13, 2001, pp. 560–563.

[54] J. C. Koech, "Modifed horn-type antennas for SKA RFI monitoring," M. Eng. thesis, Stellenbosch University, South-Africa, 2019.

[55] W. D. Burnside and C. W. Chuang, "An aperture-matched horn design," *IEEE Trans. Antennas Propag.*, vol. 30, no. 4, pp. 790–796, Jul. 1982.

[56] T.-C. Lin, C.-H. Lee, J.-L. Dong, C.-N. Chiu, D.-B. Lin, and H.-P. Lin, "A new uniformity-enhanced double ridged horn antenna for radiated susceptibility test from 1 GHz to 18 GHz," in *Proc. IEEE Int. Symp. Electromagn. Compat. and IEEE Asia-Pacific Symp. Electromagn. Compat.,* May 14-18, 2018, pp. 264–267.

[57] S. Sarjoghian, Y. Alfadhl, X. Chen, and C. G. Parini, "A 3-D-printed high-dielectric materials-filled pyramidal double-ridged horn antenna for abdominal fat measurement system," *IEEE Trans. Antennas Propag.*, vol. 69, no. 1, pp. 64–73, Jul. 2020.

[58] S. Lee, Y. Yang, K.-Y. Lee, K.-Y. Jung, and K. C. Hwang, "Robust design of 3D-printed 6–18 GHz double-ridged TEM horn antenna," *Applied Sciences*, vol. 8, no. 9, Sep. 2018, Art. no. 1582.

[59] B. Majumdar, D. Baer, S. Chakraborty, K. P. Esselle, and M. Heimlich, “A 3D printed dual-ridged horn antenna,” in *Proc. Int. Conf. on Electromagn. Adv. Appl.*, Sep. 19-23, 2016, pp. 836–839.

[60] B. Majumdar, D. Baer, S. Chakraborty, K. P. Esselle, and M. Heimlich, “Advantages and limitations of 3D printing a dual-ridged horn antenna,” *Microw. Opt. Technol. Lett.*, vol. 58, no. 9, pp. 2110–2117, Jun. 2016.

[61] J J. Haumant, G. Cochet, D. Diedhiou, A. Manchec, R. Allanic, C. Quendo, C. Person, and R.-m. Sauvage., *Ultralight wide-band double ridged horn antenna using additive technologies.* Accessed: May 18, 2024. [Online]. Available: https://www.elliptika.com/en/ultralight-wide-band-double-ridged-horn-antenna-using-additive-technologies/.

[62] H. Yao, S. Sharma, R. Henderson, S. Ashrafi, and D. MacFarlane, “Ka band 3D printed horn antennas,” in *Proc. Texas Symp. Wireless Microw. Circuits and Syst.,* Mar. 30-31, 2017, pp. 1–4.

[63] B. Zhang, Y.-X. Guo, H. Sun, and Y. Wu, “Metallic, 3D-printed, K-band-stepped, double-ridged square horn antennas,” *Applied Sciences*, vol. 8, no. 1, Dec. 2018.

[64] K. V. Hoel, M. Ignatenko, S. Kristoffersen, E. Lier, and D. S. Filipovic, “3-D printed monolithic GRIN dielectric-loaded double-ridged horn antennas,” *IEEE Trans. Antennas Propag.*, vol. 68, no. 1, pp. 533–539, Jan. 2020.

[65] J. H. H. Eriksrød, K. G. Kjelgård, and T. S. Lande, “Design of robust and low-loss 3-D printed double-ridged waveguide to microstrip transition,” *IET Microw. Antennas Propag.*, vol. 16, no. 4, pp. 224–232, Feb. 2022.

[66] I. Goode and C. E. Saavedra, “3D printed variable aperture horn with modular ridges,” *J. Phys. Commun.*, vol. 7, no. 5, May 2023, Art. no. 55004.

[67] V. Midtbøen, K. G. Kjelgård, and T. S. Lande, “3D printed horn antenna with PCB microstrip feed for UWB radar applications,” in *Proc. IEEE MTT-S Int. Microw. Workshop Ser. Adv. Materials Processes RF THz Appl.*, Sep. 20-22, 2017, pp. 1–3.

[68] B. Majumdar, D. Baer, S. Chakraborty, K. P. Esselle, and M. Heimlich, “Additive manufacturing of a dual-ridged horn antenna,” *Prog. Electromagn. Res. Lett.*, vol. 59, pp. 109–114, Apr. 2016.

[69] S. Sarjoghian, M. H. Sagor, Y. Alfadhl, and X. Chen, “A 3D-printed high-dielectric filled elliptical double-ridged horn antenna for biomedical monitoring applications,” *IEEE Access*, vol. 7, pp. 94977–94985, Jul. 2019.

[70] K. V. Hoel, S. Kristoffersen, J. Moen, K. G. Kjelgård, and T. S. Lande, “Broadband antenna design using different 3D printing technologies and metallization processes,” in *Proc. 10th Eur. Conf. Antennas Propag.,* Apr. 10-15, 2016, pp. 1–5.

[71] G.-L. Huang, S.-G. Zhou, C.-Y.-D. Sim, T.-H. Chio, and T. Yuan, “Lightweight perforated waveguide structure realized by 3-D printing for RF applications,” *IEEE Trans. Antennas Propag.*, vol. 65, no. 8, pp. 3897–3904, Jun. 2017.

[72] J. Helszajn, *Ridge Waveguides and Passive Microwave Components*, London, UK: IEE, 2000.

[73] R. Bunger, R. Beyer, and F. Arndt, "Rigorous combined mode-matching integral equation analysis of horn antennas with arbitrary cross section," *IEEE Trans. Antennas Propag.*, vol. 47, no. 11, pp. 1641–1648, Nov. 1999.

[74] T. Wriedt, K.-H. Wolff, F. Arndt, and U. Tucholke, "Rigorous hybrid field theoretic design of stepped rectangular waveguide mode converters including the horn transitions into half-space," *IEEE Trans. Antennas Propag.*, vol. 37, no. 6, pp. 780–790, Jun. 1989.

[75] D. M. Pozar, *Microwave Engineering*, 3rd edition, Hoboken, NJ, USA: Wiley, 2005.

[76] F. F. Dubrovka, G. A. Yena, P. Y. Stepanenko, and V. M. Tereschenko, "Ultra wideband double ridged horns with rectangular aperture," in *4th Proc. Int. Conf. Antenna Theory and Techn.*, Sep. 9-12, 2003, pp. 590–593.

[77] L. Botha and D. A. McNamara, "Examination of antenna patterns of profiled horns using the method of moments," in *Proc. Antennas Propag. Soc. Int. Symp.*, Jun. 17-21, 1985, pp. 293–296.

[78] J. R. Whinnery and H. W. Jamieson, "Equivalent circuits for discontinuities in transmission lines," *Proc. of the IRE*, vol. 32, no. 2, pp. 98–114, Feb. 1944.

[79] D. A. Jarvis and T. C. Rao, "Design of double-ridged rectangular waveguide of arbitrary aspect ratio and ridge height," *IEE Proc. Microw. Antennas Propag.*, vol. 147, no. 1, pp. 31–34, Feb. 2000.

[80] Z. Hradecky, M. Mazanek, and T. Korinek, "Double ridged structures mode study for broadband antennas design," in *Proc. First Eur. Conf. Antennas Propag.*, Nov. 6-10, 2006, pp. 1–6.

[81] N. Marcuvitz, *Waveguide Handbook*, New York, NY, USA: Dover, 1951.

[82] W. J. R. Hoefer and M. N. Burton, "Closed-form expressions for the parameters of finned and ridged waveguides," *IEEE Trans. Microw. Theory Tech.*, vol. 30, no. 12, pp. 2190–2194, Dec. 1982.

[83] T.-S. Chen, "Calculation of the parameters of ridge waveguides," *IRE Trans. Microw. Theory Techn.*, vol. 5, no. 1, pp. 12–17, Jan. 1957.

[84] C. A. Balanis, *Advanced Engineering Electromagnetics*, 2nd edition, Hoboken, NJ, USA: Wiley, 2012.

[85] S. Ramo and J. R. Whinnery, *Fields and Waves in Modern Radio*, New York, NY, USA: Wiley, 1949.

[86] D. B. Davidson, *Computational Electromagnetics for RF and Microwave Engineering*, New York, NY, USA: Cambridge University Press, 2005.

[87] B. Jacobs, J. W. Odendaal, and J. Joubert, "Wideband 0.5–50 GHz double-ridged guide horn antenna using coaxial-to-ridge waveguide launcher," *IET Microw. Antennas Propag.*, vol. 18, no. 4, pp 248-265, Dec. 2023.

[88] Southwest Microwave. *Power Rating for Coaxial Connectors.* Accessed: May 18, 2024. [Online]. Available: https://mpd.southwestmicrowave.com/wp-content/uploads/2020/09/Southwest-Microwave-Power-Rating.pdf.

[89] C. Fumeaux, D. Baumann, and R. Vahldieck, "Finite-volume time-domain analysis of a cavity-backed Archimedean spiral antenna," *IEEE Trans. Antennas Propag.*, vol. 54, no. 3, pp. 844–851, Mar. 2006.

[90] ETS-Lindgren. *HP High Power Microwave Absorber.* Accessed: May 18, 2024. [Online]. Available: https://www.ets-lindgren.com/datasheet/absorbers/rf-absorbers/1006/100603.

[91] Cumming Microwave. *C-RAM SFC-HC High Power Broadbanded Pyramidal Honeycomb RF Absorber.* Accessed: May 18, 2024. [Online]. Available: http://www.cumingmicrowave.com/wp-content/uploads/2013/06/390-16-C-RAM-SFC-HC.pdf.

[92] Microwave Vision Group. *HPX Series High Power Absorbers.* Accessed: May 18, 2024. [Online]. Available: https://www.mvg-world.com/media/1063/download/reference.

[93] L. Liu *et al.*, "Gradient honeycomb absorber with high power handling capability," *Appl. Phys. A*, vol. 127, no. 2, Jan. 2021, Art. no. 129.

[94] Y. Zhang, Y. J. Zhu, Y. H. Qi, W. Yu, F. H. Li, and L. Liu, "High-power broadband honeycomb absorber for 5G millimeter wave chambers," in *Proc. IEEE Int. Symp. Electromagn. Compat. and IEEE Asia-Pacific Symp. Electromagn. Compat.,* May 14-18, 2018, pp. 103–105.